UNIVERSITÄT OSNABRÜCK

Exact diagonalization studies of a one-dimensional system at electron density $\rho = 0.4$: effect of the Coulomb repulsions and distant transfer

Dem Fachbereich Physik der Universität Osnabrück
zur Erlangung des Grades eines

Doktors der Naturwissenschaften

vorgelegte Dissertation von

Dipl.–Phys. Fatiha Ouchni

aus Marokko

Osnabrück, August 2006

Betreuer	:	Apl. Prof. Dr. J. Schnack
Zweitgutachter	:	Apl. Prof. Dr. K. Betzler

33 *A Sign for them is the earth that is dead: We do give it life, and produce grain therefrom, of which ye do eat.*
34 *And We produce therein orchard with date-palms and vines, and We cause springs to gush forth therein:* 35 *That they may enjoy the fruits of this (artistry): It was not their hands that made this: will they not then give thanks?*
36 *Glory to Allah, Who created in pairs all things that the earth produces, as well as their own (human) kind and (other) things of which they have no knowledge.*
37 *And a Sign for them is the Night: We withdraw therefrom the Day, and behold they are plunged in darkness;*
38 *And the sun runs his course for a period determined for him: that is the decree of (Him), the Exalted in Might, the All-Knowing.*
39 *And the Moon,- We have measured for her mansions (to traverse) till she returns like the old (and withered) lower part of a date-stalk.*
40 *It is not permitted to the Sun to catch up the Moon, nor can the Night outstrip the Day: Each (just) swims along in (its own) orbit (according to Law).*
41 *And a Sign for them is that We bore their race (through the Flood) in the loaded Ark;*
42 *And We have created for them similar (vessels) on which they ride.*

Ya Seen, sura 36 *The Quran*

33 *And He it is Who has created the night and the day, and the sun and the moon, each in an orbit floating.*

Al-Anbiya, sura 21 *The Quran*

164 *Verily! In the creation of the heavens and the earth, and in the alternation of night and day, and the ships which sail through the sea with that which is of use to mankind, and the water (rain) which Allah sends down from the sky and makes the earth alive therewith after its death, and the moving (living) creatures of all kinds that He has scattered therein, and in the veering of winds and clouds which are held between the sky and the earth, are indeed Ayat (proofs, evidences, signs, etc.) for people of understanding.*

Al-Baqarah, sura 2 *The Quran*

47 *With power did We construct the heaven. Verily, We are Able to extend the vastness of space thereof.*

Adh-Dhariyat, sura 51 *The Quran*

To my parents, my family, my friends,
and to all those who left a trace in my memory.

Contents

1. INTRODUCTION

As the dimensionality of an electronic system decreases, it is expected that charge screening would become less important in effectively reducing the range of the Coulomb repulsions. Thus, in one dimension (1D) the role of a $1/r$ Coulomb repulsion should be important in determining the physical properties of electronic models [1, 2]. Theoretically, the long-range (LR) Coulomb potential should in principle be included when dealing with any interacting insulating phase, due to the ineffectiveness of screening. Insulators often exhibit charge patterns which differ from the uniform charge distribution encountered in ordinary metals, and in several cases the nature of charge ordering (CO) is more likely that of a Wigner lattice (WL) than that of a charge-density wave (CDW). Originally, Wigner [3] predicted that an electron liquid moving on a uniform compensating charge background crystallizes if the electron density is sufficiently small, because the e-e interaction becomes dominant over the kinetic energy of the electrons. Hubbard has pointed out the important effect of the Coulomb repulsion when it is dominating the kinetic energy on the distribution of the electrons [1] in a solid. The interactions cause a tendency for the electrons to arrange themselves in a pattern which is a generalization of the classical WL (GWL). The ordred structure of electrons may be accompanied by a lattice distortion which here is driven by electrons. However, it is sometimes difficult to determine whether the observed charge modulation is induced by LR forces or by an instability of the Fermi surface (IFS), i.e., a CDW of quantum mechanical origin. Our study of $1d$ systems at the low-density limit shows that a WL CO accompaned by a dimerization is a result of a competition between LR Coulomb interaction and an IFS.

Two key physical ingredients, strong correlations and low dimensionality, seem to be crucial for the electronic structure of novel materials, such as the cuprate superconductors. Such strongly anisotropic electronic systems can be modeled in terms of extended Hubbard models (EHM) which start from the tight-binding model with effective electronic repulsion, which can be either short or LR depending on the extent of screening. The prototype of the short-range (SR) models is the 1D Hubbard model [4, 5, 6, 7, 8] which from a mathematical point of view can be regarded as exactly solved for all fillings N/L, where N is the number of electrons and L the number of sites [9]. However, if the screening is not effective in reducing the range of the Coulomb interaction, the true LR or truncated Coulomb potential should be included. The question of importance of intersite interaction within the context of parametrized models such as EHM for low-dimensional systems was addressed by a number of authors [2, 1, 10, 11, 12, 13, 14, 15, 16]. Most of the studies within EHM have been done for half or quarter-fillings but have not been carried out for lower densities, although many issues arise from extensive experiments on low density systems which anticipate future investigations. The cuprate composite material $Sr_{14}Cu_{24}O_{41}$ (SCO), under study in this thesis, belongs to such systems. SCO shows insulating behavior at low temperatures, which may be a signature of LR interaction as already discussed above. Other properties, like the appearence of anti-ferromagnetic (AF) dimers and WL CO in the chain subsystem direct our theoretical investigations towards using strong interactions, better suited for well localized systems. Structural elements, which will be given in detail in Chap. 3, of this material, chains and ladders are very good realizations of different EHM with strong interactions. A comparison of our results,

using a Heisenberg model, with experimental magnetization data for SCO, show indeed the need of strong interactions between different holes on the chains.

The scope of this thesis is the following. In Chap. 2 we learn basic properties of 1d electronic systems from a theoretical point of view. The discussion will be kept to the minimum necessary to understand the succeeding chapters. In Chap. 3, we introduce the exact diagonalization (ED) method and its application to the bare Hubbard model. Chap. 4 provides a description of the properties of SCO from an experimental point of view. We investigate in Chap. 5 an EHM that contains LR interactions and distant transfer t_2. We show the important role of a strong LR interactions and t_2 in stabilizing the WL CO and appearance of AF dimers. The results will be discussed only qualitatively. Using the same method, in Chap. 6, we introduce a Heisenberg model that depends parametrically on hole positions, to obtain the magnetization, using ED method. Then, we compare the results with experiments [17].

A summary and outlook in Chap. 7 close the thesis.

2. 1D SYSTEMS- THEORETICAL OVERVIEW

2.1. Introduction

1d systems have received considerable theoretical attention for several reasons. First, 1d systems are often easier to handle theoretically than two- or three-dimensional systems. Secondly, often problems exactly solvable in 1d may only be approximately treated in higher dimensionalities. And finally, characteristic low dimensional effects can be studied.

2.2. The tight-binding model

2.2.1. Overview

The tight-binding model is usually used when realistic band structures are required or when the mean-free path of the conduction electrons is not long enough compared to the interatomic distance for a free-electron model to be used. In this section we consider the tight-binding model to compare the magnitude of the Coulomb interaction energy with that of the kinetic energy.

Let us first recall the second quantised form of the Hamiltonian governing the motion, and interaction between the particles. The non-interacting one-body Hamiltonian of a one-dimensional (1d) system of electrons subject to a lattice potential V is given by

$$\mathcal{H}^{(0)} = \int dx \sum_{\sigma} c_{\sigma}^{\dagger}(x) \Big[\hat{p}^2/2m + V(\hat{x}) \Big] c_{\sigma}(x) \,, \tag{2.1}$$

where $\hat{p} = -i\hbar\partial_x$. The field operators obey the anticommutation relations appropriate for fermions. The field operators act on the big many-particle Fock space, $\mathcal{F} = \oplus_{N=0}^{\infty} \mathcal{F}_N$. Each $N-$particle space $\mathcal{F}_N$ is spanned by states of the form $\prod_{i=1}^{N} c_{\sigma_i}^{\dagger}(x_i)|\Omega\rangle$ where the no-particle state or vacuum $|\Omega\rangle$ is annihilated by all operators $c_{\sigma}(x)$.

Applying a two-body Coulomb interaction potential,

$$\frac{1}{2} \sum_{i \neq j} \frac{e^2}{|\hat{x}_i - \hat{x}_j|} \,,$$

where $\hat{x}_i$ is the position operator of the i-th electron, the total many-body Hamiltonian takes the second quantised form

$$\mathcal{H} = \mathcal{H}^{(0)} + \frac{1}{2} \int dx \int dx' \sum_{\sigma\sigma'} c_{\sigma}^{\dagger}(x) c_{\sigma'}^{\dagger}(x') \frac{e^2}{|\hat{x}_i - \hat{x}_j|} c_{\sigma'}(x') c_{\sigma}(x) \,. \tag{2.2}$$

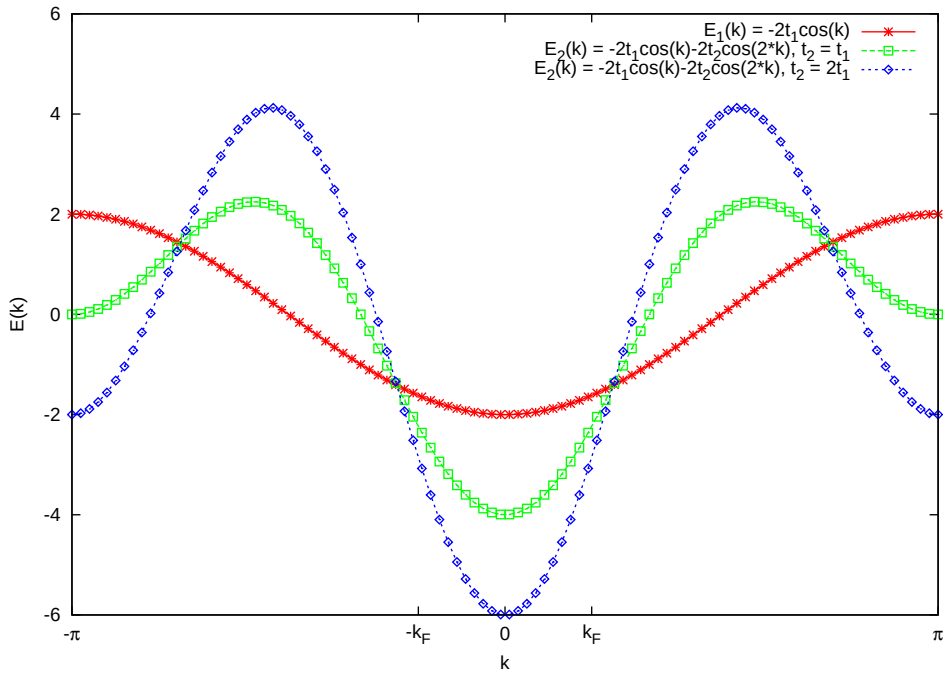

Figure 2.1.: The dispersion relation, $E(k)$, of the non-interacting tight binding chain at filling $N/L = 0.4$. The hopping matrix element t_{lm} are here restricted to only nearest-neighbour and next-nearest hoppings $t_{l,l\pm1} = t_1$ and $t_{l,l\pm2} = t_2$, respectively.

Next, we introduce an interatomic distance, i.e. the lattice parameter a and the wave function $|\psi_l\rangle$ (Wannier function) for an electron on an isolated atom located at la. The wave function of an electron on a $1d$ chain of such atoms is given by

$$\overbrace{|\psi_l\rangle}^{c_l^\dagger|\Omega\rangle} = \frac{1}{\sqrt{L}} \sum_{k\in[-\pi/a,\pi/a]}^{\text{B.Z.}} \exp(-ikla) \overbrace{|\psi_k\rangle}^{c_k^\dagger|\Omega\rangle}, \qquad |\psi_k\rangle = \frac{1}{\sqrt{L}} \sum_{l=1}^{L} \exp(ikla)|\psi_l\rangle \tag{2.3}$$

where L denotes the total number of atoms in the chain. $|\psi_k\rangle$ (Bloch function) carries a quasi-momentum index k and makes it possible to calculate the expectation value of the Hamiltonian in the crystal. Here the sum on k runs over the L $k-$points spanning the Brillouin zone, i.e. $k = 2\pi m/aL$ with integers $-L/2 < m \leq L/2$. The field operators associated with the Wannier functions are defined by

$$\overbrace{|\psi_l\rangle}^{c_{l\sigma}^\dagger|\Omega\rangle} = \int_0^{La} dx \quad \overbrace{|x\rangle}^{c_\sigma^\dagger(x)|\Omega\rangle} \langle x|\psi_l\rangle\,, \tag{2.4}$$

i.e.

$$c_{l\sigma}^{\dagger} = \int_0^{La} dx\, \psi_l(x) c_{\sigma}^{\dagger}(x), \qquad c_{\sigma}^{\dagger}(x) = \sum_{l=1}^{L} \psi_l^{\star}(x) c_{l\sigma}^{\dagger}(x)\,. \tag{2.5}$$

In the above equation, the spin degree of freedom is restored. Physically, $c_{l\sigma}^{\dagger}$ can be interpreted as an operator creating an electron with spin σ at site l. The operators $c_{l\sigma}$, and $c_{l\sigma}^{\dagger}$ obey fermionic anticommutation relations $\left[c_{l\sigma}, c_{m\sigma'}^{\dagger}\right]_+ = \delta_{\sigma\sigma'}\delta_{lm}$.

In the presence of a two-body Coulomb interaction, a substitution of the field operators in Eq. (2.) by Wannier operators generates the generalised tight-binding Hamiltonian

$$\mathcal{H} = -\sum_{lm}\sum_{\sigma} t_{lm} c_{l\sigma}^{\dagger} c_{m\sigma} + \sum_{lmrs}\sum_{\sigma\sigma'} U_{lmrs} c_{l\sigma}^{\dagger} c_{m\sigma}^{\dagger} c_{r\sigma'} c_{s\sigma}\,, \tag{2.6}$$

where the hopping matrix elements are given by

$$t_{lm} = -\langle \psi_l | \mathcal{H}^0 | \psi_m \rangle = \frac{1}{L}\sum_{k} e^{-i(l-m)ka} \epsilon_k = t_{lm}^{\star}\,, \tag{2.7}$$

and the interaction parameters are set by

$$U_{lmrs} = \frac{1}{2}\int_0^{La} dx \int_0^{La} dx' \psi_l^{\star}(x)\psi_m^{\star}(x') \frac{e^2}{|\hat{x}_i - \hat{x}_j|} \psi_r(x')\psi_s(x)\,. \tag{2.8}$$

Physically t_{lm} represents the probability for an electron to hop from a site l to a site m.

In the momentum basis, $c_{l\sigma} = L^{-1/2}\sum_k^{\text{B.Z.}} e^{-ilka} c_{k\sigma}$, the non-interacting Hamiltonian is diagonalised as $\mathcal{H}^0 = \sum_k^{\text{B.Z.}} c_{k\sigma}^{\dagger} c_{k\sigma}$. Fig 2.1 depicts the cosine band thus obtained.

Let us suppose that the energy of an electron in the state $|\psi_l\rangle$ is ϵ. If this orbital is highly localized, then the amplitude for it to tunnel or hop between sites will decay exponentially with distance between sites, and to a good approximation, most of the matrix elements of the general tight-binding model are small and can be neglected.
Focusing on the most relevant:

2.2.2. Hubbard model

- Short-Range Coulomb Interactions

How are electronic states in the conduction band modified by the Coulomb interaction (Eq. 2.8) between electrons?

In the atomic limit where the atoms are well-separated and the overlap between neighbouring orbitals is weak, the matrix elements t_{lm} and U_{lmlm} are exponentially small in the interatomic separation. By contrast the on-site Coulomb or Hubbard interaction

$$\sum_l \sum_\sigma U_{llll} c^\dagger_{l\sigma} c^\dagger_{l\sigma'} c_{l\sigma'} c_{l\sigma} = U \sum_l \hat{n}_{l\uparrow} \hat{n}_{l\downarrow} \,, \tag{2.9}$$

where $U = 2U_{llll}$, increases as the atomic wavefunctions become more localised.

Therefore, in the atomic limit, a strongly interacting many-body system of electrons can be described to a good approximation by

$$\mathcal{H} = -t \sum_{\langle lm \rangle} \sum_\sigma c^\dagger_{l\sigma} c_{m\sigma} + U \hat{n}_{l\uparrow} \hat{n}_{l\downarrow} \,, \tag{2.10}$$

where we have introduced the notation $\langle lm \rangle$ to indicate a sum over neighbouring lattice sites, and $t = t_{lm}$ (assumed real and usually positive). We set the constant energy $\epsilon_0 = t_{ll} = 0$. The above Hamiltonian has just two parameters: the matrix element t of an electron jump from one site to an adjacent site in the lattice and the parameter U is the local Coulomb repulsion which operates when two electrons occupy the same orbital. These two forces compete to determine whether a material is conducting or insulating. U must be taken into account when it is not negligible compared to the kinetic energy of the electrons. The kinetic energy to be compared with U is represented by the band width $W = 4t$. This is due to the fact that the wave function of the localized electron is composed of a linear combination of the $\psi_{k\sigma}(x)$ of (2.3). Therefore the energy of the localized electron is represented approximately by the maximum energy, W, available in the tight-binding model.

The model (2.10), proposed in Refs [6, 7, 8], has become known as the Hubbard model. This is one of the simplest interacting fermionic models one can write and has been extensively studied to describe the theory of strongly correlated electron systems (SCES), for which U is greater than or of the order of W. In particular, the Hubbard model can explain certain materials known as Mott insulators that are predicted to be conductors in standard band theory models.

The Hubbard model is the prototype of the short-range models and from a mathematical point of view can be regarded as exactly solved for all fillings $\rho = N/L$. Lieb and Wu were able, using the Bethe-ansatz technique, to give the exact ground-state wavefunction and a scheme for calculating energy and related static quantities [9]. In the Hubbard model, written in the site representation, the Coulomb term is diagonal, whereas in the Fourier representation the kinetic term is diagonal and it corresponds to the band spectrum

$$\varepsilon_k = 2t \sum_{\alpha=1}^{d} \cos k_\alpha \,, \tag{2.11}$$

where d is the dimension of space.

The diagonality of one or another term in the Hamiltonian provides an opportunity of developing perturbation theory for two limiting cases: $U \ll W$ and $U \gg W$. They are sometimes called the limits of weak and strong coupling, respectively. For weak coupling $U \ll W$, the

Hubbard interaction can be treated perturbatively within the framework of the **Fermi-liquid theory**. In the half-filled case ($\rho = 1$) the density of states is that of a metal. The opposite limiting case when $U \gg W$ corresponds to a strongly correlated system. When a small parameter W/U is used, it is possible to go over from the Hubbard Hamiltonian to the effective Hamiltonian that is known as the $t - J$ model [18], which describes the motion of electrons on a lattice when there is no more than one electron at any one site and the effective exchange interaction between the nearest neighbours is described by

$$J = 2\frac{t^2}{U}\,. \tag{2.12}$$

Perturbation theory treatment in terms of the parameter W/U can be developed for the $t-J$ model. In this case the zeroth approximation deals with single-site atomic states, whereas the kinetic term and the effective exchange are regarded formally as perturbations [19]. In the case $\rho = 1$ the Hamiltonian of the $t-J$ model reduces to the exchange Hamiltonian in the Heisenberg model. In this case charges are frozen and the low energy configurations just correspond to different spin orientations: in a bipartite lattice, the ground state is always a nondegenerate spin singlet and it is expected to show correlations typical of 1d antiferromagnets: $\langle S_l S_0\rangle \sim (-1)^l/l$. Spin excitations are gapless with linear dispersion relation. See Appendix C for more details on the strong coupling limit.

It follows that the Hubbard model describes itinerant magnetism in the weak coupling limit, and localized magnetism in the tight coupling limit when $\rho = 1$. The intermediate case when $U \sim W$, is naturally most difficult to deal with, although physically it is the most interesting because it is in this case that the correlation effects leading to a metal-insulator phase transition are manifested most strongly, localised moments appear, and a strong coupling forms between the behaviour of charge carries and magnetic order [6, 20].

- LR Coulomb Interactions

What is expected to occur when the range of the Coulomb repulsion between conduction electrons is not restricted to within each atom but reaches far beyond next neighbours?

In the tight-binding model, the direct terms $U_{lmml} = V_{lm}$ involve integrals over square moduli of Wannier functions and couple density fluctuations at different sites,

$$\sum_{l\neq m} V_{lm}\hat{n}_l\hat{n}_m\,, \tag{2.13}$$

where $\hat{n}_l = \sum_\sigma c^\dagger_{l\sigma}c_{l\sigma}$. Such terms have the capacity to induce charge density instabilities.

For $V_{lm}/W \gg 1$ ($\mid l-m \mid < \infty$), all electrons repel each other. In the case of the short-range repulsion, U, it was meaninful to use the band model because in this case electrons can move freely unless two of them come onto the same atom. In the present case, however, V_{lm} is larger for two electrons distant from each other than the energy W gainded by a free motion. All electrons will become localized in such a way as to minimize the total Coulomb energy. The

resultant ordered structure of electrons is called a WL of electrons as was mentioned early in the introduction. The lattice distortion here (due to the charge structure) is driven by electrons which tend to distribute themselves equidistantly.

If $W = 0$, the system is of an insulating character. When $W \neq 0$, however small it is compared to V_{lm}, electrons will more or less be able to move. This is particularly so when the electron density is low and hence the mean distance between neighbouring electrons is long, in which case the movement of an electron to its neighbouring electrons will cause only a small increment in the Coulomb energy.

The open questions regard the effects of doping in the presence of LR repulsive interactions. In the bare Hubbard model (short-range interaction), as soon as we insert holes into the lattice, the charge gap closes and both the charge and the spin branch of the excitation spectrum acquire linear dispersion relation, characterized by finite charge and spin velocity, as was shown in [21] and references therein. In this class of spin isotropic Luttinger liquids, the long wavelength properties of the system are determined by a single dimensionless parameter K_ρ governing the power-law decay of all correlation functions. The antiferromagnetic correlations in the ground state are characterized by the wave vector $q = 2k_F$ and decay as $x^{(1+K_\rho)}$ while the density correlations are dominated by oscillations at $q = 4k_F$ and behave as x^{-4k_F}. The analysis based on bosonization technique [22] showed that the LR nature of the Coulomb interaction is expected to change this picture: while the spin sector is unaffected by interactions, the charge spectrum now becomes non analytic: $\omega_q \sim q\sqrt{|\ln q|}$. Formally this corresponds to the $K_\rho \to 0$ limiting case. In fact, the leading power law behavior of spin correlations is just $\cos(2k_F x)/x$ while charge correlations decay more slowly than any power law and the momentum distribution is continuous with all its derivatives at the Fermi momentum. Actually, the bosonization study allowed to determine the precise form of the asymptotic behavior, which turns out to be:

$$\begin{aligned} < \mathbf{S}(x) \cdot \mathbf{S}(0) > &\sim \exp\left[-c(\ln x)^{1/2}\right] \frac{\cos(2k_F x)}{x}\,, \\ < n(x)n(0) > &\sim \exp\left[-4c(\ln x)^{1/2}\right] \cos(4k_F x)\,, \\ < c^\dagger_{x,\sigma} c_{0,\sigma} > &\sim \exp\left[-c'(\ln x)^{3/2}\right] \cos(k_F x)\,, \end{aligned} \tag{2.14}$$

with c and c' non universal positive constants, and k_F is the Fermi wave vector and is equal to $k_F = \rho\pi/2$.

- Coulomb Interactions and CDW

The investigation of CDW and its influence on the properties of materials has been the subject of intense research for many decades now. Such a phenomenon is often observed in low-dimensional metallic systems, where the spatial modulation of the conduction electron density has a periodicity different from that of the undistorted lattice. As a consequence, a gap opens up in the single-particle excitation spectrum of such materials. Interestingly would be the occurence of CDW in insulators. The conclusion we have reached from the role of Coulomb interactions in the limit where the Coulomb energy is much larger than the band energy is that this can produce a CDW. Thus, a possible origine of CDW in insulators is a large Coulomb

interaction. For instance, as we will show in Chap. 5, at $\rho = 0.4$, the apparent structure is specified by the wave numbers $2k_F$ and $4k_F$. The apparent $4k_F$ CDW is the dominating one. The formation of $2k_F$ CDW appears only for very large LR Coulomb repulsion. Any material in which both the $2k_F$ and the $4k_F$ CDW appear, has two kinds of 1d chain. Therefore a possibility is that one of the two types of chains has a weak interaction among electrons giving rise to the $2k_F$ CDW while the other, having a strong Coulomb repulsion, brings about a $4k_F$ CDW.

Another possibility, however, must also be remembered, i.e. that the $2k_F$ and the $4k_F$ CDW may coexist on a single kind of 1d chain [23, 24, 25] which corresponds to our results shown in Chap. 5. In such a case, one of four waves, a $4k_F$ CDW, and a $2k_F$ spin-density wave (SDW) will be dominant depending on the relative magnitudes of the hole-hole repulsion and the NNN hopping. The interchain interaction will be not considered in our study.

However, waves other than the dominant type can coexist. Theories have shown that a $2k_F$ CDW, and a $4k_F$ SDW can grow in spite of a presence of electron-electron (hole-hole) Coulomb repulsion [23, 24, 25], and that its growth is assisted by the interchain repulsion [23, 24].

2.2.3. Exchange interaction

A second important contribution from (2.8) for intersite interactions derives from the exchange coupling which induces magnetic correlations among the electronic spins. Setting $J_{ij}^F = U_{ijij}$, we obtain

$$\sum_{l\neq m}\sum_{\sigma} U_{lmlm} c_{l\sigma}^{\dagger} c_{m\sigma'}^{\dagger} c_{l\sigma'} c_{m\sigma} = -2\sum_{l\neq m} J_{lm}^F \big(\hat{S}_l \hat{S}_m + \frac{1}{4}\hat{n}_l \hat{n}_m\big)\,. \tag{2.15}$$

Such contributions tend to induce weak ferromagnetic coupling of neighbouring spins (i.e. $J_F > 0$). Physically, the origin of the coupling is easily understood as deriving from a competition between kinetic and potential energies. By aligning with each other and forming a symmetric spin state, two electrons can reduce their potential energy arising from their mutual Coulomb repulsion. To enforce the antisymmetry of the two-electron state, the orbital wave function would have to vanish at $x = x'$ where the Coulomb potential is largest. This mechanism is familiar from atomic physics where it is manifest as Hund's rule.

3. QUASI-1D (q1d) $Sr_{14-x}Ca_xCu_{24}O_{41}$

3.1. (q1d) $Sr_{14-x}Ca_xCu_{24}O_{41}$- a complex system

Although new composite materials $M_{14}Cu_{24}O_{41}$ (M=La, Sr, Ca, Ba, Y) have been identified [26, 27], their physical properties have drawn much attention of many experimentalists only with the recent discovery of superconductivity in $Sr_{0.4}Ca_{13.6}Cu_{24}O_{41}$, a material heavily doped by Ca, under high pressure [28]. The superconductivity is expected to be driven by the spin-liquid ground state with an energy gap, as theoretically predicted by Dagotto, Riera, and Scalapino [29, 30, 31], in the hole doped even-leg ladder structural elements. According to an optical study [32], the role of Ca substitution, which does not change the formal valence of Cu, was thought to transfer holes from the chain to the ladder. Thus, the superconductivity in this system is considered to be realized when the quasi-one dimensionality of holes on the ladder becomes sufficiently weakened. Most experiments have been made on $Sr_{14}Cu_{24}O_{41}$ (SCO) that has proved more easy to dope than $SrCu_2O_3$. $M_{14}Cu_{24}O_{41}$ can undergo a CDW transition.

3.1.1. Crystallographic structure of q1d $Sr_{14-x}Ca_xCu_{24}O_{41}$

$Sr_{14-x}Ca_xCu_{24}O_{41}$ (SCCO) is built up by alternating layers, edge-sharing CuO_2 weakly coupled chains of copper ions which are coupled by the nearly 90° Cu-O-Cu bonds, and two-leg Cu_2O_3 ladders of copper ions, which are coupled by the nearly 180° Cu-O-Cu bonds in the ac plane [26, 27]. Each ladder is coupled by nearly 90° Cu-O-Cu bonds. These two sublayers are separated by (Sr,Ca) atoms and stacked along the b axis. This structure is denoted in Fig. 3.1. The chains and ladders run along the c axis and their unit cell parameters roughly differ by a factor of $\sqrt{2}$ along this direction, the Cu-Cu distance in the unit cell in the chains $c_C \approx 2.75\,\mathrm{\AA}$, and in the ladders $c_L \approx 3.9\,\mathrm{\AA}$. Such a misfit is shown in Fig. 3.2. This misfit leads to an incommensurate modulation of the two sublattices. The lattice constants a and b, which corresponds to the stacking, are the same for both elements.

3.1.2. Electronic structure of q1d $Sr_{14-x}Ca_xCu_{24}O_{41}$

It was shown in [33] and references therein that a superexchange interaction J in insulating cuprates (IC) contains information on the electronic state of these materials and a dependence on the dimensionality of Cu-O network. The compound SCO contains CuO_4 units that are linked to form a variety of Cu-O networks. There are two types of linkage, i.e., the corner-sharing and edge-sharing types, as shown in Fig. 3.3. The former involves the corner sharing of two CuO_4 units forming a straight Cu-O-Cu bond, while the latter type is formed by sharing of the edges of CuO_4 units with an almost 90° Cu-O-Cu bond angle. The chains are composed of edge-sharing corners with a very weak ferromagnetic 90° Cu-O-Cu bond whereas the ladders contain both types of linkage. The copper moments are coupled by an almost 180° Cu-O-Cu bond angle. The neighboring ladders are coupled by almost 90° Cu-O-Cu bonds which give a ferromagnetic interaction. Because this ferromagnetic interaction is much weaker than the dominant antiferromagnetic interaction, these ladders are almost decoupled.

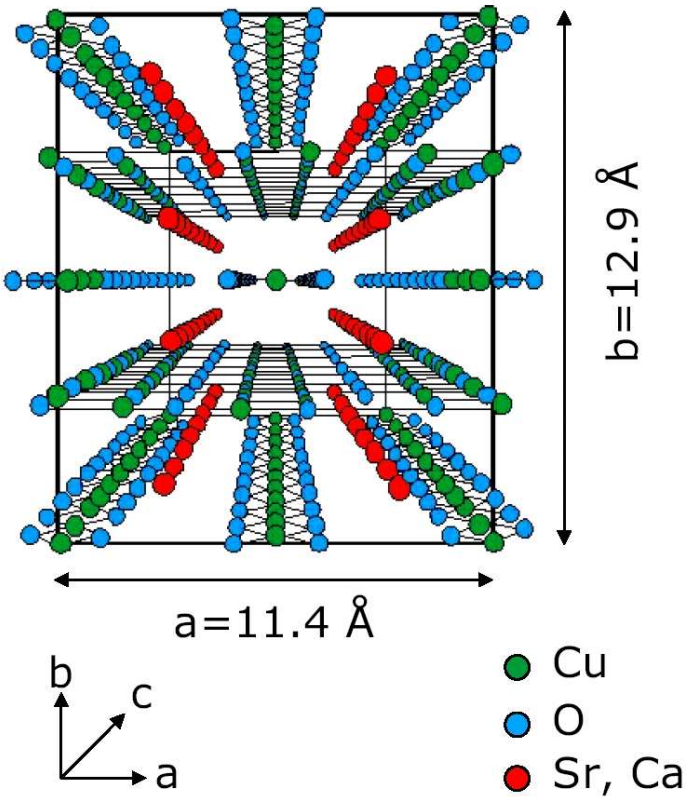

Figure 3.1.: The crystal structure of SCO viewed along the c axis.

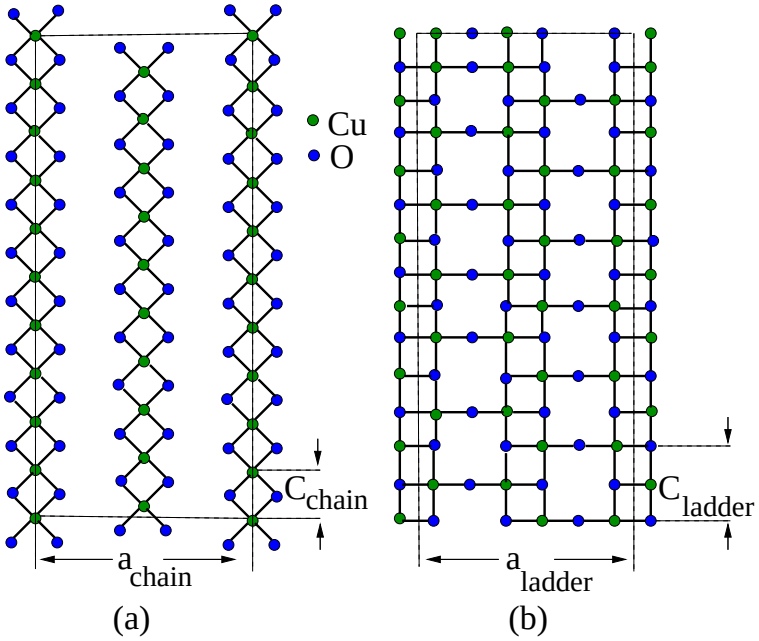

Figure 3.2.: (a) and (b) show the chain and the ladder of copper ions in SCO, respectively. The dashed rectangles represent the universal unit cell in the (010) crystallographic plane. Here, c_{chain} and c_{ladder} represent the CuO_2 chain and Cu_2O_3 ladder subunits, respectively.

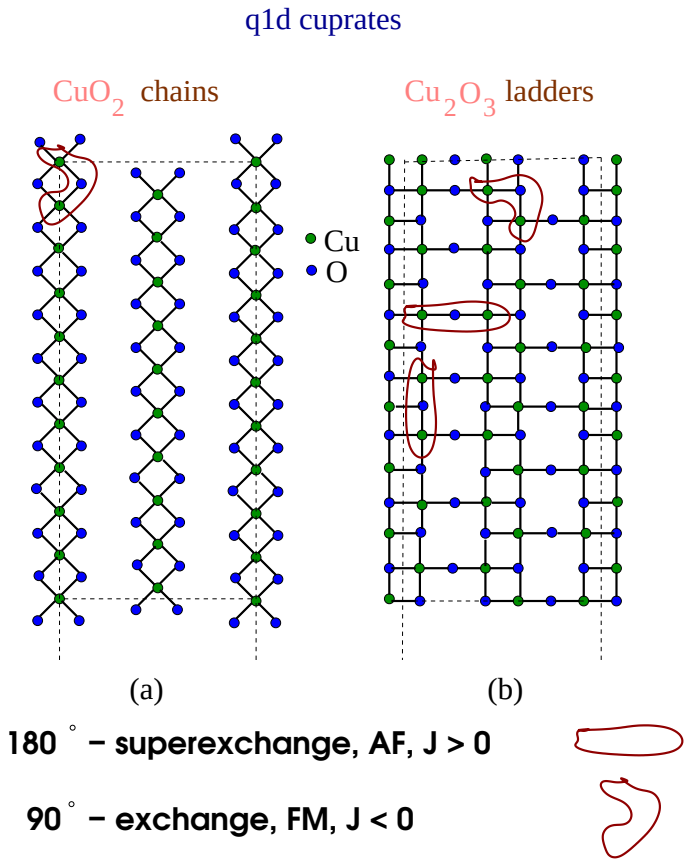

Figure 3.3.: Linkage of two CuO_4 units. (a) Corner-sharing and (b) edge-sharing structures.

The electronic structure of the parent compound SCO was calculated *ab initio* within the local-density approximation [34]. The calculations were performed on a small unit cell containing one formula unit of SCO and neglecting the structural modulation. The compound was calculated as a metal, leading to a finite density of states (DOS) at the Fermi energy E_F. However, an insulating behavior was observed for SCO by angle-resolved photoemission spectroscopy (ARPES) experiments. The total DOS is compared with ARPES with fairly good agreement [35]. It was found that the chain bands near E_F are mainly composed of the antibonding combination of Cu d_{xz} orbitals and O p_x and p_z orbitals, while the ladder bands are composed of Cu $d_{x^2-z^2}$ orbitals and O p_x and p_z orbitals. These bands of both subsystems have

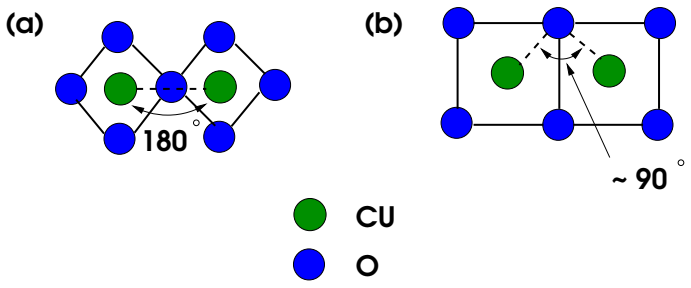

Figure 3.4.: Linkage of two CuO_4 units. (a) Corner-sharing and (b) edge-sharing structures.

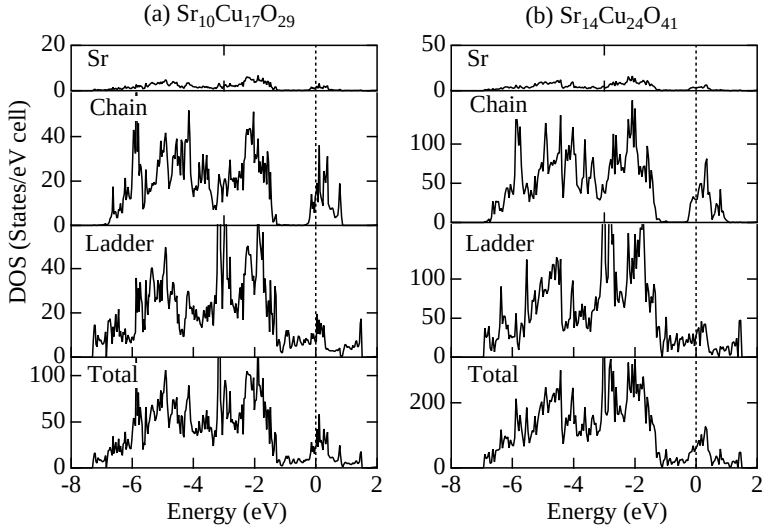

Figure 3.5.: The total and partial density of states of (a) $Sr_{10}Cu_{17}O_{29}$ and (b) $Sr_{14}Cu_{24}O_{41}$.

a pseudo-one-dimensional character and the interladder hoppings are $5-20\,\%$ of the intraladder ones. In both subsystems, the bands were fitted by simple q1d tight-binding dispersions with NN and NNN hoppings between rungs and adjacent ladders and along and between the chains. For chains the NNN hoppings, t_2, are largest and twice the nearest-neighbour ones. The total and partial DOS is shown in Fig. 3.5.

3.1.3. Hole distribution

A significant feature of the composite (Sr, Ca, La)$_{14}Cu_{24}O_{41}$ materials is that they are self-doped. In $Sr_{14}Cu_{24}O_{41}$ the Cu average valence is +2.25, i.e., six holes per formula unit (f.u.) are already doped without any substitution. These holes are generally believed to reside essentially in the chain. Bond-valence-sum (BVS) calculations [36, 37] confirm the concept of self-doping holes and give higher BVS values for holes in the chains. Madelug energy calculations [33] lead to the same conclusion for $x = 0$ that all holes are in the chains due to their larger electronegativity, resulting in a hole concentration of about 6/10 per Cu site in the chain. On the experimental side, the resistivity and magnetic measurements on $La_6Ca_8Cu_{24}O_{41}$, with a pure Cu^{2+} valence and thus no holes, as well as on compounds with increasing Sr content for La and a corresponding number of doped holes lead to the conclusion that all doped holes reside on the chains of $Sr_{14}Cu_{24}O_{41}$ giving a $Cu^{2.6+}$ valence. Holes enter the structural units with larger O/Cu ratios which are the CuO_2 chains. The ladders remain undoped and magnetically inert due to a large spin gap. The moments in the undoped chains interact weakly, and every hole added creates a nonmagnetic CuO_2 unit and decreases the resistivity [38]. However, neutron scattering experiments [39, 40, 41, 42, 43] and optical investigations [32, 44, 45] point to an arrangement of one hole for every other Cu site of the chain. That means that only 5 out of the 6 doped holes reside in the $(CuO_2)_{10}$ chain subunit of $Sr_{14}Cu_{24}O_{41}$, and one hole is left for the $(Cu_2O_3)_7$ ladder unit. Polarisation-dependent near-edge x-ray absorption spectroscopy fine structure (NEXAFS) [46] studied hole states on both the chain and ladder sites. The finding is that nonisovalent substitution of Sr^{2+} with La^{3+} (or Y^{3+}) reduces the nominal hole count from its full value of six holes per f.u. and that the substitutions of Ca^{2+} for Sr^{2+} leave the nominal

hole nominal constant. NEXAFS confirms the assumption of [32, 44, 45] that one hole per f.u. resides in the ladders of $x = 0$. However, it supports the evidence for weaker redistribution of holes from chains to ladders while stronger redistribution was observed by Osafune *et al.* [32]. NEXAFS provides the absolute hole counts in the chains and ladders, while Osafune *et al.* provide only relative numbers. Studies of the hole/spin patterns within the subsystems provide an additional information on the hole distribution at room temperature, as well as at low temperatures.

3.1.4. Chains subsystem

Magnetic susceptibility

The magnetic susceptibility is a bulk observable which should not be able to distinguish between the subsystems. Even though the magnetic properties of (Sr, Ca, La)$_{14}$Cu$_{24}$O$_{41}$ have been studied by susceptibility [39, 38, 47], Carter *et al.* [38] found that the parent compound $La_6Ca_8Cu_{24}O_{41}$ showed a temperature dependence of the susceptibility consistent with weakly interacting 10($\pm$0.5) Cu^{2+} spins per f.u., all contributed from the chain site. The Cu^{2+} spins in the ladder were virtually inert below 300 **K** due to the large spin gap. The spin gap on the ladder for $Sr_{14}Cu_{24}O_{41}$ is much larger; $\Delta_{ladder} = 510 \pm 20$ **K** (from the nuclear magnetic resonance (NMR) shift; Magishi *et al.*, [48]). A large spin gap in the ladder of the order of 400 **K** is also observed by Neutron Inelastic Scattering [41, 40] and thermal conductivity measurements [49]. This leads to the conclusion that only spins in chains contribute to the susceptibility of q1d cuprates. The spin ladders have a singlet ground state. And surprisingly the spin chains also exhibit a singlet ground state with a spin gap of $11 - 12\,meV$ [38, 50, 40, 51], while homogeneous spin chains are known to be gap-less in the spin-channel. The question of the nature of ordering which leads to the spin-gaped state in the chains is still open.

Susceptibility measurements [39, 38] suggested that the spin gap in the chains is due to the formation of weakly interacting spin dimers. They found that a simple AF dimer model gives a good fit to the low temperature part of χ. The AF dimer model is based on organising spins along the chain into isolated antiferromagnetically coupled pairs. The solid line in Fig. 3.6 shows the result of the AF dimer model $\chi = 2N_D(g\mu_B)^2/kBT[3 + e^{(J/k_BT)}]$ with the number of dimers $N_D = 2.0$ per formula unit ($g = 2.05$ along the a direction) and the interdimer exchange $J = 130$ **K** . The deviation of χ from the dimer model at high temperatures can be attributed to the contribution from the ladders.

Inelastic neutron scattering (INS) and X-ray diffraction (XRD)

Neutron scattering [53, 54, 40, 43] and X-ray diffraction [52] experiments have revealed a periodic spacing of spin dimers and that the chain dimeric units are formed by NNN spins separated by a hole. Matsuda *et al.* [54] interpreted the observed spin excitations at low temperatures ($T = 8$ **K**) with a model where two different types of antiferromagnetically coupled dimers exist, characterised by intradimer spin separation of two chain parameters and four chain parameters, $2c$ and $4c$, respectively. Two independent INS groups [40] and [43] have confirmed from their measurements at low temperatures ($T = 5 - 10$ **K**) the assumption proposed by the authors of Cu NMR [50] that dimers are separated by two holes. Such a picture leads to a chain filling of 6 holes per f.u., that is all the holes located on the chains. Their interpretation was based on a model with only AF dimers. Interdimer distance was found to be three

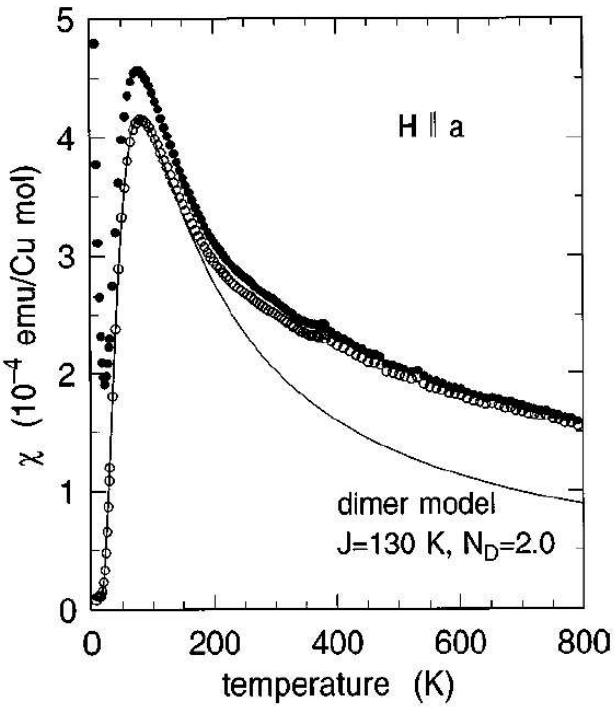

Figure 3.6.: Comparison for $x = 0$, of the experimentally measured temperature dependence of the magnetic susceptibility, χ, represented by solid dots, Motoyama *et al* [47], and the dimer model, $N_D = 2.0$ per formula unit, indicated by a line.

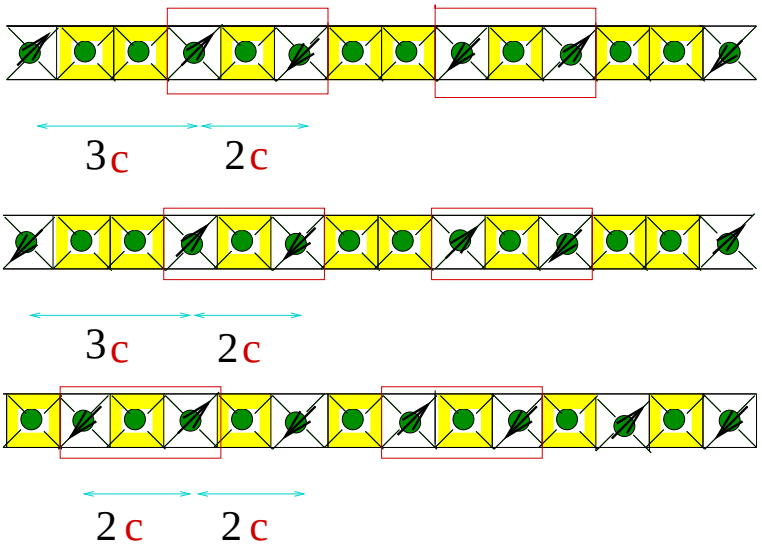

Figure 3.7.: Structure and periodicity of the spin dimers (framed) with the complementary charge-order of the holes (Zhang-Rice singlet sites denoted by yellow squares) for $x = 0$ chains in the alternation models. The upper and intermediate models, periodicity $5c$, chains hole count 6, are proposed by INS measurements [40], [43], and [42] at $5 - 20$ **K**. The lower model, periodicity $4c$, chains hole count 5, is resulting from XRD measurements [52] at 50 **K**, and INS measurements [42].

chain parameters, 3c, Fig. 3.7. The chain superstructure periodicity in this model is 5c. XRD results for $Sr_{14}Cu_{24}O_{41}$ directly point to structural change related to charge-order [52]. These measurements were performed at ($T = 50$ **K**). The observed periodicity was equal to 4 chain parameters. This result leads to the choice of the model with the chain hole count 5, Fig. 3.7. In this model 2.5 AF dimers would appear per 10 Cu sites. We note again the contradiction between the observed charge-order (by XRD) and spin order (by INS) due to different hole counts. However the INS experiments were performed at lower temperatures than XRD.

NMR

NMR offers the possibility of a direct determination of the spin gap. ^{63}Cu NMR signals for the ladder site can be separated from those for the chain site, since nuclei of these sites possess different quadrupole coupling. Kumagai *et al.* [55] investigated $Sr_{14-x}Ca_xCu_{24}O_{41}$ by Cu NMR and nuclear quadrupole resonance (NQR). The energy gaps in the spin excitation spectra (spin gap) were confirmed to be $\Delta = 140$ **K** for the CuO_2 chain and $\Delta = 470$ **K** for the Cu_2O_3 ladder in $Sr_{14}Cu_{24}O_{41}$. Also they found that the spin gap for the chain is nearly independent of the substitution of Ca up to ($x = 9$), Y up to ($x = 2$), and La up to ($x = 1$). Detailed NMR and NQR studies reveal static distribution of holes below 200 **K** for $x = 0$ [50]. Two distinct resonance spectra are obtained for the chain sites. They are assigned to the magnetic Cu sites with spin-1/2 and the nonmagnetic Cu sites. The suggested model to explain these results is that the dimers are separated by at least two nonmagnetic sites, which is in accordance and reproduces the same spin-pattern as deduced from INS.

ESR

Electron spin resonance (ESR) has been studied as a function of temperature and Ca concentration ($x = 0-12$) [56]. Since the spin ladders show a large spin gap of about $400-500$ **K**, the dominant contribution to the ESR signal below 300 **K** is attributed to the CuO_2 spin-1/2 chains. For all values of x the data reveal a remarkable influence of the hole dynamics on the Cu-spin relaxation. This enables to identify the onset of charge order in the chains for $x = 0$ and 2 at 200 and 170 **K**, respectively. A further increase of x rapidly destroys the charge ordered state. A transition to an antiferromagnetically ordered state is observed at 2.5 **K** for $x = 12$. The whole set of ESR data can be understood in terms of a transfer of only a small amount of holes from the chains to the ladders with increasing x in $Sr_{14-x}Ca_xCu_{24}O_{41}$ and a simultaneous crossover from independent dimers to antiferromagnetically coupled chains, which order at low temperatures due to weak interchain interactions.

4. LANCZOS ALGORITHM

4.1. Introduction

Numerical methods are essential in the investigation of strongly correlated fermion systems, because in such a sysems the perturbation theory to treat the electronic correlations often breaks down. These methods are playing an important role in understanding of how correlation effects determine the properties of strongly interacting electrons. The dimensions of the matrices involved are usually very large and a large number of eigenvalues and their corresponding eigenvectors are needed to compute the desired physical quantities. This presents a problem in numerical treatments and makes it one of the grand challenges in the field of supercomputing. The following chapter will be devoted to the numerical technique based on the Lanczos algorithm. However, the focus will be on the specific area of strongly correlated models, namely 1d fermionic systems, to illustrate various technical aspects of the method and to discuss the physics of these systems.

4.2. Basic idea

ED has played a very important role in understanding the ground state properties of quantum systems. The idea is to set up the Hamiltonian $N_{\mathcal{H}} \times N_{\mathcal{H}}$ matrix for the model in a finite Hilbert space of dimension $N_{\mathcal{H}}$ and calculate the eigenpairs (eigenvalues and eigenvectors) by diagonalizing the matrix. Since the Hilbert space of quantum system grows exponentially with system size, a direct numerical attack is impractical for large $N_{\mathcal{H}}$ as the matrix increases like $N_{\mathcal{H}}^2$ and the CPU-time like $N_{\mathcal{H}}^3$. Instead, an iterative scheme known as the Lanczos algorithm [57, 58] is often used to construct iteratively a sequence of orthonormal vectors that form a basis under which the Hamiltonian is real and tri-diagonal [58, 59]. Once in this form the ground state and the low-lying excitation spectrum for small systems (of up to about 10^8 states) can be found with high accuracy using standard library subroutines [60]. This is especially important for fermion systems where quantum Monte carlo methods suffer from the well known "negative sign problem" [61]. The Lanczos algorithm is a recursive algorithm. The success of this method is due to the rapidly growing power of supercomputers. The disavantage of ED is that it inevitably suffers from finite size effects. Because of the restrictions on the cluster size, there are limitations for a complete finite-size scaling analysis with this technique (Hilbert space can be dramatically reduced once the symmetry properties are used). Nevertheless, ED is very valuable in supplementing analytical and other numerical results. The Hamiltonian matrices for most quantum spin models are sparse (which is the case of an overdoped system). Although the matrix can be stored in sparse matrix form in the Lanczos iteration, the size of the matrix grows so rapidly with the system size that one may not have enough memory or disk space to store it even as a sparse matrix. The algorithm presented here will be illustrated by considering the example of a Hubbard chain, but it can be applied to any quantum Hamiltonian.

4.3. The Lanczos method

4.3.1. Invariant subspace

The concept of an invariant subspace is an important point for understanding the Lanczos method. Linear algebra tells us that a subspace that is spanned by m linear independent vectors $|\phi_1\rangle, \ldots, |\phi_m\rangle$ is invariant under a hermitian matrix $\mathcal{H}$, if for any vector $|\phi\rangle$ in the subspace the vector $\mathcal{H}|\phi\rangle$ is also in the subspace. In the following we will denote the $\mathcal{H}$-invariant subspace by $\mathfrak{H}$. What does this invariance mean? If Q_m is a $n \times m$ matrix whose columns are the orthonormal vectors $|\phi_l\rangle$, then the matrix product $\mathcal{H}Q_m$ is a $n \times m$ matrix too and the columns are linear combinations of the columns of Q_m. Assuming that the $|\phi_l\rangle$ form an orthonormal basis in the invariant subspace, i.e. $Q_m^t Q_m = \mathrm{id}_m$, one can find a $m \times m$ matrix T_m which satisfies the relation

$$\mathcal{H}Q_m = Q_m T_m \Leftrightarrow Q_m^t \mathcal{H} Q_m = T_m \,. \tag{4.1}$$

This means that the eigenpairs of a large matrix $\mathcal{H}$ can be found from those of a smaller matrix T_m. For instance, let λ and $|v\rangle$ be an eigenpair of T_m. Multiplication of $T_m|v\rangle = \lambda|v\rangle$ by Q_m and the use of relation (4.1) leads to the equivalence

$$Q_m T_m |v\rangle = \lambda Q_m |v\rangle \Leftrightarrow \mathcal{H} Q_m |v\rangle = \lambda Q_m |v\rangle \,, \tag{4.2}$$

where λ and $Q_m|v\rangle$ describe an eigenpair of $\mathcal{H}$. The Lanczos algorithm approximately generates such an invariant subspace $\mathfrak{H}$.

4.3.2. The algorithm

Following is a brief idea about the steps involved during the construction of the $\mathcal{H}$-invariant subspace $\mathfrak{H}$.

First step: the initial state

In this procedure it is necessary to select an arbitrary but nonzero normalized vector $|\phi_0\rangle$ ($\langle\phi_0|\phi_0\rangle = 1$) which belongs to the Hilbert space $\mathfrak{H}$ of the model being studied. If some information about the ground state is known, like total momentum or spin, then it is convenient to start the iteration with a vector already belonging to the subspace having those quantum numbers. Otherwise, it is convenient to select an initial vector with randomly chosen coefficients.

Second step: orthogonality

After $|\phi_0\rangle$ is selected, a second normalized vector $|\phi_1\rangle$ can be constructed by multiplying the hermitian matrix $\mathcal{H}$ with the initial vector

$$b_1|\phi_1\rangle = \mathcal{H}|\phi_0\rangle - a_0|\phi_0\rangle \,. \tag{4.3}$$

To ensure the orthogonality $\langle\phi_0|\phi_1\rangle = 0$ one has to subtract the projection onto $|\phi_0\rangle$. One imposes

$$\langle\phi_0|\phi_1\rangle = \langle\phi_0|\mathcal{H}|\phi_0\rangle - a_0\langle\phi_0|\phi_0\rangle = 0\,, \tag{4.4}$$

and because $|\phi_0\rangle$ is normalized, one obtains

$$a_0 = \langle\phi_0|\mathcal{H}|\phi_0\rangle\,, \tag{4.5}$$

that is a_0 is the average energy of $|\phi_0\rangle$. In addition, b_1 can be found by taking the scalar product of Eq. (4.3) with $\langle\phi_1|$

$$b_1 = \langle\phi_1|\mathcal{H}|\phi_0\rangle\,. \tag{4.6}$$

Notice that, by using Eq. (4.3), one also has that

$$b_1^2 = \langle\phi_0|(\mathcal{H}-a_0)(\mathcal{H}-a_0)|\phi_0\rangle = \langle\phi_0|\mathcal{H}^2|\phi_0\rangle - a_0^2\,, \tag{4.7}$$

that is b_1 is the mean square energy deviation of $|\phi_0\rangle$.

By repeating the above procedure, we define the third normalized vector, in such a way that it is orthogonal both to $|\phi_0\rangle$ and $|\phi_1\rangle$

$$b_2|\phi_2\rangle = \mathcal{H}|\phi_1\rangle - a_1|\phi_1\rangle - b|\phi_0\rangle\,. \tag{4.8}$$

The conditions of orthogonality are

$$\langle\phi_1|\phi_2\rangle = 0 \Leftrightarrow a_1 = \langle\phi_1|\mathcal{H}|\phi_1\rangle\,, \tag{4.9}$$

$$\langle\phi_0|\phi_2\rangle = 0 \Leftrightarrow \langle\phi_0|\mathcal{H}|\phi_1\rangle - b = 0 \Leftrightarrow b = b_1\,, \tag{4.10}$$

and finally, the fact that $|\phi_2\rangle$ is normalized leads to

$$b_2 = \langle\phi_2|\mathcal{H}|\phi_2\rangle\,. \tag{4.11}$$

This procedure can be generalized by defining an orthogonal basis recursively. Suppose one has constructed the Lanczos vector up to $|\phi_{m-1}\rangle$

$$b_{m-1}|\phi_{m-1}\rangle = \mathcal{H}|\phi_{m-2}\rangle - a_{m-2}|\phi_{m-2}\rangle - b_{m-2}|\phi_{m-3}\rangle\,, \tag{4.12}$$

with

$$\begin{aligned} a_{m-2} =& \langle \phi_{m-2}|\mathcal{H}|\phi_{m-2}\rangle \,, \\ b_{m-2} =& \langle \phi_{m-2}|\mathcal{H}|\phi_{m-3}\rangle \,, \\ b_{m-1} =& \langle \phi_{m-1}|\mathcal{H}|\phi_{m-2}\rangle \,. \end{aligned} \tag{4.13}$$

orthogonal to all $|\phi_j\rangle$ with $j \leq m-2$. Then one defines

$$b_m|\phi_m\rangle = \mathcal{H}|\phi_{m-1}\rangle - a_{m-1}|\phi_{m-1}\rangle - b'|\phi_{m-2}\rangle - \sum_{j=1}^{m-3} A_j|\phi_j\rangle \,. \tag{4.14}$$

The conditions of orthogonality reads as

$$\begin{aligned} \langle \phi_{m-1}|\phi_{m-1}\rangle \Leftrightarrow \rangle a_{m-1} =& \langle \phi_{m-1}|\mathcal{H}|\phi_{m-1}\rangle \,, \\ \langle \phi_{m-2}|\phi_{m-1}\rangle \Leftrightarrow b' =& \langle \phi_{m-2}|\mathcal{H}|\phi_{m-1}\rangle = b_{m-1} \,, \\ A_j =& \langle \phi_j|\mathcal{H}|\phi_{m-1}\rangle \,, \end{aligned} \tag{4.15}$$

but, because one has

$$b_{j+1}|\phi_{j+1}\rangle = \mathcal{H}|\phi_j\rangle - a_j|\phi_j\rangle - b_j|\phi_{j-1}\rangle \,, \tag{4.16}$$

and $j+1 \leq m-2$, one obtains that

$$A_j = 0 \,. \tag{4.17}$$

Then, $|\phi_m\rangle$, once orthogonalized to $|\phi_{m-1}\rangle$ and $|\phi_{m-2}\rangle$, it is automatically orthogonal to all the previous vectors.

Thus, at each Lanczos step, it is sufficient to orthogonalize only to the previous two vectors, and the orthogonality with the previous ones is automatic. That makes the Lanczos algorithm very efficient.

After $j = m$ steps a set of orthonormal vectors $|\phi_m\rangle$ has been generated. These vectors are the columns of an orthonormal matrix Q_m. By applying formula (4.1) the Hamiltonian matrix $\mathcal{H}$ will be transformed into a tridiagonal symmetric matrix, whith a_j on the diagonal and b_j below and above the diagonal

$$Q_m^t \mathcal{H} Q_m = T_m = \begin{pmatrix} a_0 & b_1 & 0 & 0 & . & . \\ b_1 & a_1 & b_2 & 0 & . & . \\ 0 & b_2 & a_2 & b_3 & . & . \\ 0 & 0 & b_3 & a_3 & . & . \\ . & . & . & . & & \\ . & . & . & . & & \end{pmatrix} \tag{4.18}$$

If m is sufficiently large, the eigenvalues λ of the Lanczos matrix T_m should be good approximations of the eigenvalues of $\mathcal{H}$ which are restricted to the invariant subspace

$$\mathfrak{H} = \mathrm{Span}\Big\{|\phi_0\rangle, \mathcal{H}|\phi_0\rangle, \mathcal{H}^2|\phi_0\rangle, \ldots, \mathcal{H}^{m-1}|\phi_0\rangle\Big\}\,, \tag{4.19}$$

known as Krylov subspace generated by application of $\mathcal{H}$ to $|\phi_0\rangle$. In practice for large systems, the iterations will stop at a much earlier stage. Either after some Lanczos iteration steps n_L (typically of the order of $\sim$ 100 steps), or when b_j^2 is smaller than a chosen precision value. For instance for Hubbard model with 10 sites and periodic boundary conditions at a density $\rho = 0.4$ and zero magnetization, the termination is signaled if b_j^2 is smaller than 10^{-13}.

The main aim in the numerical realization of the Lanczos algorithm is to keep computational effort low. The most expensive operation is the matrix-vector multiplication $\mathcal{H}|\phi_0\rangle$. In addition, the Hamiltonian matrix cannot be stored in the computer memory. The storage of matrix elements would require too much memory. With the Lanczos algorithm, one needs only two or three vectors of dimension $N_{\mathcal{H}}$ (two vectors are enough for making the Lanczos procedure). When we are interested in having the ground-state vector, and not only the eigenvalues, three vectors are useful to avoid a lot of writing and reading from the hard disk.

4.4. Application of the method: Hamiltonian of the model

As an example we will sketch how to implement the Lanczos method for the 1d one-band Hubbard model with nearest neighbor hopping t and local Coulomb repulsion U

$$\mathcal{H} = -t \sum_{<ij>,\sigma} \Big(c_{i\sigma}^\dagger c_{j\sigma} + H.c.\Big) + U \sum_i n_{i\uparrow} n_{i\downarrow}\,. \tag{4.20}$$

The Hamiltonian is applied to a chain with 20 sites and periodic boundary conditions.

The possible configurations of up-spins are independent of the configurations of the down spins and the Hilbert space $\mathcal{H}_{\mathrm{Hubbard}}$ of all possible configurations is just the direct product of the Hilbert space of down spins $\mathcal{H}_\downarrow$ and of up-spins $\mathcal{H}_\uparrow$

$$\mathcal{H}_{\mathrm{Hubbard}} = \mathcal{H}_\downarrow \otimes \mathcal{H}_\uparrow\,. \tag{4.21}$$

In order to actually be able to express the Hamiltonian as a matrix, we need a basis of the Hilbert space. Since the model's Hamiltonian conserves the total electron number and the electrons' z-component S_z of the total magnetization, we can restrict ourself to the subspace whose basis states have a certain number of up and down spins. We thus want to construct a basis of all states with N particles on L sites and a given S_z. Each basis state of this subspace is identified by an index α between 1 and the subspace dimension

$$dim = \left(\frac{L!}{N_\uparrow!\,(L-N_\uparrow)!}\right)\left(\frac{L!}{N_\downarrow!\,(L-N_\downarrow)!}\right)\,. \tag{4.22}$$

By doing so, we generate two lists, the "small" list called 'basis' gives the occupation index α for each basis state index. The "big" list called 'Hspace' (total Hilbert space) gives the basis state index for a given occupation index α (or -1 if α corresponds to a state with wrong quantum numbers). The advantage of this representationis, that, except for the special case of a system with only up spins or only down spins, these two spaces are much smaller that the total Hilbert space. Therefore it is possible to keep an inverse list of all bit patterns for the up and down spins in memory. And the search for the index of a new configuration reduces to two lookups in these tables to find the up-index and the down-index. An implementation for the two-dimensional Hubbard model, using this representation, is described in detail in Ref. [62]. For instance, if we restrict ourself to the subspace with zero magnetization and a density $n = 0.4$, the Hibert space thus has dimension $\left(\begin{array}{c} 20 \\ 4 \end{array} \right)^2 \simeq 23$ million, whereis the dimension of the total Hilbert space is 4^{20}.

The occupation number basis for a system of L sites is defined as

$$|n\rangle = |n_{1\uparrow} n_{1\downarrow} n_{2\uparrow} .... n_{L-1\downarrow} n_{L\uparrow} n_{L\downarrow}\rangle = \prod_{i\sigma, n_{i\sigma}=1} C^{\dagger}_{i\sigma} |0\rangle \,, \tag{4.23}$$

where $|0\rangle$ is the vacuum state. The occupation index α is defined as

$$\alpha = \sum_{i=1}^{L} \Big(n_{i\uparrow} 2^{2i-2} + n_{i\downarrow} 2^{2i-1} \Big) \,. \tag{4.24}$$

The many-body Hamilton-matrices are sparse. Only a small fraction of all matrix elements is not zero. And since we are interested in low density $n = 0.4$, the matrix is very sparse, it is then practical to store only the nonzero matrix elements not only to save memory but also to speed up operations of the form $\mathcal{H}|v\rangle$ which form the heart of the ED procedure.

See Appendix A for more details about coding the basis states.

4.5. Symmetry operations: reducing Hilbert space dimension

The Lanczos method gives essentially exact results for ground-state and low lying eigenvectors. In spite of these advantages, memory limitations impose severe restrictions on the size of the clusters that can be studied within this method. This problem can be considerably alleviated using the symmetries of the Hamiltonian that reduce the matrix Hamiltonian to a block form. We have already used two symmetries, the conservation of particle number and the conservation of the $z-$component of the total magnetisation. To reduce further the sise of the matrix, we considere as well the momentum conservation due to translational invariant in systems with periodic boundary conditions. The total number of basis states is greatly reduced by L lattice translations with lattice displacements $R_l, l = 0, 1, 2, \ldots, L-1,$. The average reduction is $\sim 1/L$. The total number of basis states is now about 1 million for $\rho = 0.4$, and $L = 20$. Let us define the lattice translation operator $T_l, l = 0, \ldots, L-1$, which bring site i to site $T_l(i)$ through the relation

$$T_1\Big[|.\rangle_1|.\rangle_2\ldots|.\rangle_L\Big] = |.\rangle_2|.\rangle_3\ldots|.\rangle_1\,. \tag{4.25}$$

This operator does not change the type of configuration in the sense that it does not affect the number of doubly-occupied, singly-occupied, and empty sites. We can then construct Block states of the form:

$$|n,k\rangle = \frac{1}{\mathcal{N}_{n,k}}\sum_{l=0}^{L-1} e^{-ikl}T_l|n\rangle\,, \tag{4.26}$$

where $\mathcal{N}_{n,k}$ is a normalisation constant. As already said, in a subspace of fixed k there is only a fraction of about $1/L$ of the states of the full space. The exact number depends on the value of k. However, we have to pay a price. For momentum $k \neq 0$ or π the Hamiltonian matrix is no longer real, but complex and we need twice as much memory to store the vectors. In addition the calculation of the matrix elements is more dofficult due to the normalisation constants $\mathcal{N}_{n,k}$ and prefactors e^{-ikl} arising from the translational symmetry.

Spin space reflection also commutes with $\mathcal{H}$, but does not preserve the total numbers of up and down spins when they are different. Using the set of basis state described above, we can construct the Hamiltonian matrix $\mathcal{H}$ for the Hubbard model. The problem of finding the ground state of the 20 sites reduces to that of finding the eigenvector of $\mathcal{H}$ with smallest eigenvalue using the Lanczos algorithm.

More details about the implementation of the Lanczos method is given in the Appendix A.

4.6. Measurements

Almost any equal time expectation value can be evaluated within the exact diagonalization approach. Following are some important expectation values for our study:

- spin spin correlations: $\langle S(i)\cdot S(j)\rangle\,.$
- charge charge correlations: $\langle n(i)\cdot n(j)\rangle\,.$
- hole hole correlations: $\langle\big(n_{hi}\cdot n_{hj}\big)\rangle\,.$

These real space correlations are easily implemented. From these correlations, one can compute static structure factors by means of Fourier transforms. For the conduction band we have for the charge and spin structure factors:

- $C(q) = \frac{1}{L}\sum_{j,k}^{L} e^{iq(j-k)}\langle\left(n_{j\sigma}+n_{j\bar{\sigma}}\right)\left(n_{k\sigma}+n_{k\bar{\sigma}}\right)\rangle\,.$
- $S(q) = \frac{1}{4L}\sum_{j,k}^{L} e^{iq(j-k)}\langle\left(n_{j\sigma}+n_{j\bar{\sigma}}\right)\left(n_{k\sigma}+n_{k\bar{\sigma}}\right)\rangle, = \frac{1}{L}\sum_{j,k}^{L} e^{iq(k-k)}\langle S^z_j S^z_k\rangle\,.$

5. Wigner crystallization and dimerization for 1d system at low-density limit

5.1. Introduction

The question of the importance of intersite interaction within the context of parametrized models such as EHM for low-dimensional systems was addressed by a number of authors [2, 1, 10, 11, 12, 13, 14, 15, 16]. Most of the studies within EHM have been done for half or quarter-fillings but have not been carried out for lower densities, although many issues arise from extensive experiments on low density systems which anticipate future investigations. The composite material SCO which was introduced in Chap. (3), belongs to such systems.

Experiments by several groups have reported the coexistence of low-temperature superstructure and dimerized state of the CuO_2 chains in the parent compound SCO as it was mentioned in detail in Chap. (3). It was shown that dimers are formed between Cu^{+2} ions that are separated by twice the distance between NN Cu ions along the chain (c direction) at low temperature.

The arrangement of the dimers in the chain was discussed mainly with two possible models provided by **NMR** studies [50], which revealed that both Cu^{+2} and Cu^{+3} exist in the chain. The first model is that each dimer is separated by one ZR singlet (model I), in which a lattice distortion with 4 times the periodicity of the chain structure is required, and this was supported by lattice distortion measurments [52]. The second is that the dimers are separated by two ZR singlets (model II), in which a lattice distortion with 5 times the periodicity of the chain structure is required, and this is consistent with studies of magnetic excitations by using INS [51, 43, 40]. This situation is shown in Fig. 5.1 where the CO is of a GWL form [1].
The opportunity of dimerization may be a result of competing distant transfer t_2 for NNN and

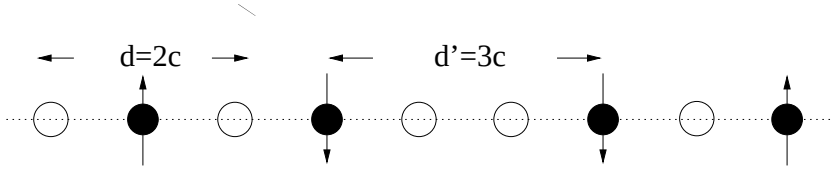

Figure 5.1.: Schematic representation of a model of interacting antiferromagnetic dimers along the chains of $Sr_{14}Cu_{24}O_{41}$, with lattice paremeter c, suggested by INS. [51, 43, 40]

Coulomb repulsion. A model with t_1 (nearest neighbour (NN) hopping) and t_2 may have some relevance to real materials such as SCO. For edge-sharing chains, the largest hopping is t_2 due to the superexchange path Cu-O-O-Cu whereis NN (Cu-Cu) hopping t_1 should be reduced due to the 90° Cu-O-Cu bond angle. In fact band calculation for SCO shows that $t_1 = -0.09$ eV and $t_2 = -0.17$ eV [34].

Here, in order to work out this discrepancy, we investigate an overdoped 1d system ($\rho = 0.4$) by using extended Hubbard models. Because of complex superstructure of SCO, our aim is not

to reproduce the experimental results but rather to check whether such system, for some range of the model parameters, shows the same superstructure accompagned by a dimerization which was observed in SCO. The computed model allows us to understand the origin of the CDW and chain dimerization.

5.2. The formulation of the model

We have used an EHM with NN and NNN hoppings to consider the geometry of the edge-sharing CuO_2 chains. We have also considered the fact that the holes in these chains are localized, so a bare and a truncated hole-hole repulsion are introduced. The WL CO suggested by Hubbard for the density $\rho = 0.4$ forbids two charges to be a NN as it is shown in Fig. 5.1. Therefore, we have introduced a short e-e repulsion V_{ee} in our Hamiltonian to consider such order but also we have found that this term stabilizes the formation of the dimer singlet and enhances further the intradimer correlation function.

The model we consider is thus described by the Hamiltonian

$$\begin{aligned} H = & - \sum_{i\neq j,\sigma} t_{ij} c^{\dagger}_{i\sigma} c_{j\sigma} + U \sum_{i} n_{i\uparrow} n_{i\downarrow} + \frac{1}{2} \sum_{i\neq j} Vh_{ij} n_{hi} n_{hj} \\ & + V_{ee} \sum_{i} n_i n_{i+1}, \end{aligned} \tag{5.1}$$

where $c^{\dagger}_{i\sigma}$ ($c_{i\sigma}$) is the creation (annihilation) operator of an electron with spin σ ($=\uparrow,\downarrow$) at site i and $n_{hi} = 2 - c^{\dagger}_i c_i$ ($n_i = c^{\dagger}_i c_i$) is the hole (electron) number operator, respectively. t_{ij} is the transfer integral; U, V_{ij} are the matrix elements of Coulomb interaction on-site and inter-sites, respectively (here and further we put $t_{i,i\pm1} = t_1$, $t_{i,i\pm2} = t_2$, $Vh_{i,i+l} = V_h/|l| = Vh_l$, l being the distance between holes. To distinguish between the bare and truncated Coulomb repulsion amplitudes, we put Vh_t for the bare repulsion and Vh_r for the truncated repulsion. We set $t_1 = 1$ and assume $U \gg t_1$ as it is the case for cuprate materials. Let us first investigate the effect of Vh_l at $t_2 = 0$ (model I). The effect of V_{ee} will be discussed later in this paper.
For all calculations we set $U = 10t_1$. Nevertheless, we will investigate, for the truncated repulsion case, the behavior of the CO and spin correlations upon varing the parameter U/t_1. Fig. 5.2 shows a schematic representation of the model Hamiltonian.

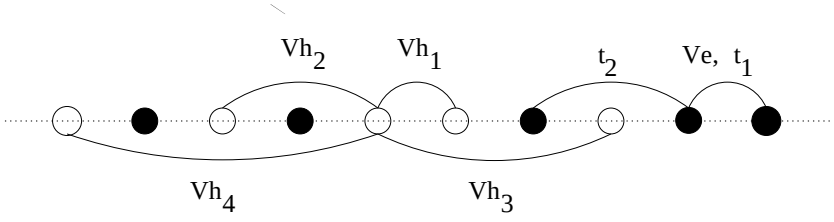

Figure 5.2.: Schematic representation of the single-chain EHM.

5.3. RESULTS OF CALCULATION

5.3.1. Charge ordering

5.3.1.1. Model I

- Effect of Vh_t/t_1

When the bare hole-hole Coulomb repulsion with magnitude Vh_t/t_1 is turned off, configurations with more than two holes sitting close to each other have a large weight in the ground-state. Therefore, the WL CO is absent. As a consequence of $Vh_t/t_1 \neq 0$, an apparent $4k_F$ peak appears in the behavior of the charge structure factor, shown in Fig. 5.3 (a), which reflects the presence and nature of long-range charge correlations, and defined as

$$C(q) = \frac{1}{L}\sum_{jl} \exp(iq(j-l))(\langle n_j n_l\rangle - < nj >< n_l >), \tag{5.2}$$

with $n_j = n_{j\uparrow} + n_{j\downarrow}$ and $\langle n_j n_l\rangle$ is the density-density correlation function. $C(4k_F)$ are enhanced by increasing the magnitude Vh_t/t_1. A small $2k_F$ peak develops at large magnitude ($Vh_t/t_1[\gtrsim 40]$). The size dependence of $C(q)$ shown in the inset of Fig. 5.3 (a) suggests the $2k_F$ singularity at $Vh_t/t_1 = 40$. So, we need a large bare repulsion between holes to create an oscillation at $2k_F$. Thus, large Vh_t/t_1 values enhance the probability to have charges separated by ($d = 5c, c = 1$) intersite distance as seen in Fig. 5.3 (b). This distance represents the WL CO periodicity (see Fig. 5.1).

We have used the Hamiltonian with a localized holes instead of the Hamiltonian with electron-electron repulsion, which is well documented in the literature, due to the fact that at large magnitudes the charge pattern obtained for the bare hole-hole Coulomb repulsion is different from that obtained using long-ranged electron-electron repulsion. For the same magnitude, the two repulsions lead to different CO. The main CO observed for the e-e repulsion is of type

0000110000110000,

where 0 represents a hole and 1 a charge. Here, the two charges 11 are on the same site and having different spins. Upon increasing Vh_t/t_1 and Ve_t/t_1, where Ve_t/t_1 is the magnitude of LR e-e repulsion, $C(2k_F)_{Ve_t} \gg C(2k_F)_{Vh_t}$. However at small magnitudes, the CO is almost the same for both repulsions, as seen in Fig. 5.4.

Upon increasing Vh_t/t_1, $C(2k_F)$ is enhanced. At filling $\rho = 0.4$, any configuration with two NN charges has more than two holes sitting close to each other. Such situation costs an amount of repulsion energy of order of Vh_t/t_1. Therefore, large magnitudes Vh_t/t_1 decrease the probability to have charges on adjacent sites as seen in Fig. 5.3 (b).

- Effect of Vh_r/t_1

The same qualitative behavior of $\langle n_0 n_l\rangle$ and $C(q)$ holds when the range of the Coulomb interaction is limited to some r. For $r = 4$ we find that the ground-state of the system is dominated by configurations of the WL CO type

...001010010100...,

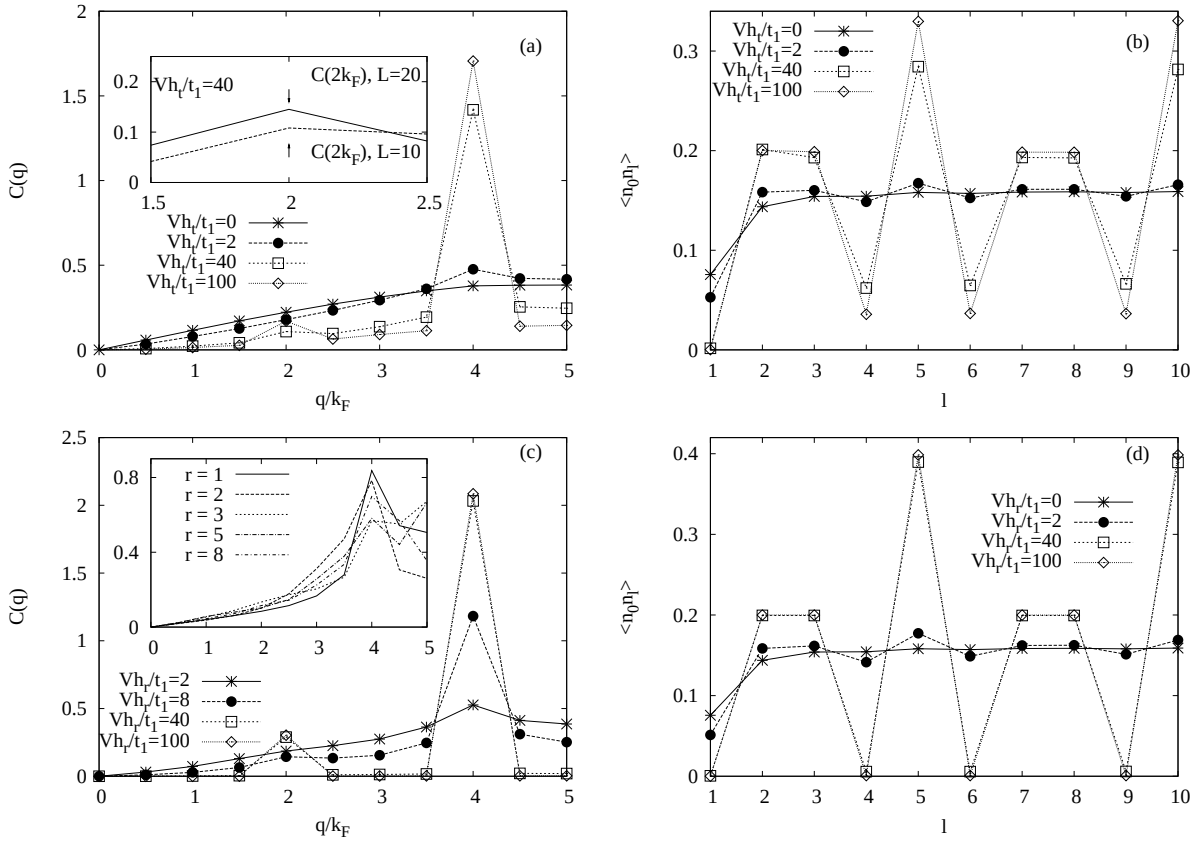

Figure 5.3.: Plots for $U/t_1 = 10, t_2/t_1 = 0$. (a) and (c) Charge structure factor $C(q)$ for various Vh_t/t_1 (Vh_r/t_1) values, respectively. The $Vh_t/t_1 = 40$ inset in Fig. 5.3 (a) shows the dependence of $C(2k_F)$ of the system size L. The inset of Fig. 5.3 (c) shows the behavior of $C(q)$ for $r \neq 4$. (b) and (d) Real-space density-density correlation functions $\langle n_0 n_l \rangle$ for various Vh_t/t_1 (Vh_r/t_1) values, respectively.

where 1 represents a charge. However, the $4k_F$ and $2k_F$ peaks stabilize at smaller magnitude ($Vh_r/t_1 = 40$) of the truncated repulsion, while $C(4k_F)$ and $C(2k_F)$ keep increasing for the bare repulsion. Fig. 5.3 (c) and Fig. 5.3(d) show the behavior of $C(q)$ and $C(l) = \langle n_0 n_l \rangle$ versus different magnitudes Vh_r/t_1. Quantitatively, the magnitude of $C(4k_F)$ and $C(2k_F)$ is larger than that for Vh_t/t_1. The $2k_F$ peak shows up clearly at smaller magnitude Vh_r/t_1 ($Vh_r/t_1 = 8$). This is due to the fact that the truncated Coulomb repulsion increases $C(l = d)$, the density-density correlation function at WL distance d, as seen in Fig. 5.3 (d), whereas the NN $C(1)$ is zero. Thus WL CO is stabilized under Vh_r/t_1.

For any $r \neq 4$ or $r \neq d_{\max}$, where $d_{\max}$ is the maximum distance between two charges, WL CO configurations are absent; the $2k_F$ singularities do not show up, as seen in the inset of Fig. 5.3 (c) which shows the behavior of $C(q)$ at different $r \neq 4$ for $Vh_r/t_1 = 10$. Upon increasing r, the LR nature of the Coulomb repulsions reduce the amplitude of CO. This is in agreement with Refs.[11, 13].

Next we will introduce a distant hopping t_2 to investigate its effect on WL CO. We will consider mainly two cases $t_2/t_1 = 1$ and $t_2/t_1 = 2$ to be consistent with band calculations for

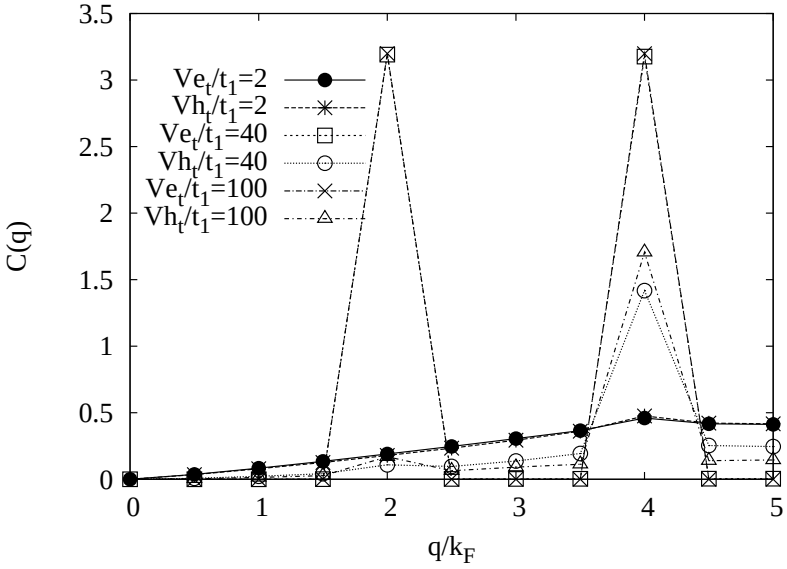

Figure 5.4.: $C(q)$ for both repulsions, the bare hole-hole repulsion and e-e repulsion for various Vh_t/t_1 and Vh_e/t_1 values, respectively, at $U/t_1 = 10, t_2/t_1 = 0$.

SCO as was already mentioned above.

5.3.1.2. Model II

- Effect of $t_2/t_1 \neq 0$ for Vh_t/t_1

The NNN hopping t_2 reduces the magnitude of $C(4k_F)$ for $Vh_t/t_1 < 100$. In the parameter range $40 < Vh_t/t_1 < 100$ the $2k_F$ peaks disappear (see Fig. 5.5 (a)). This is due to the fact that t_2 redistributes the charges. Upon increasing t_2/t_1 from 1 to 2, one can observe a tendency to create an homogeneous distribution of the charges [see Fig. 5.5 (b)]. The NN charge correlation $C(1)$ increases, while $C(2)$ and $C(5)$ decrease. The increase of the magnitude Vh_t/t_1 compensates the effect of t_2. The $2k_F$ peaks reappear (see Fig. 5.5 (c)) due to the increase of $C(5)$. And the magnitude of $4k_F$ peaks increases. Thus, larger values for Vh_t/t_1 ($Vh_t/t_1 > 40$) are needed to cancel fully the effect of t_2 (see Fig. 5.5 (d)).

- Effect of $t_2/t_1 \neq 0$ for Vh_r/t_1

The same effect of $t_2/t_1 \neq 0$ on $C(q)$ and $C(l)$ holds for the truncated repulsion. The magnitude of $C(4k_F)$ is reduced for $Vh_r/t_1 < 40$. The $2k_F$ peaks disappear for $Vh_r/t_1 < 20$ (see Fig. 5.5 (e)). However, the effect of $t_2/t_1 \neq 0$ is cancelled at smaller magnitude of the repulsion ($Vh_r/t_1 = 40$), as seen in the inset of Fig. 5.5(f).

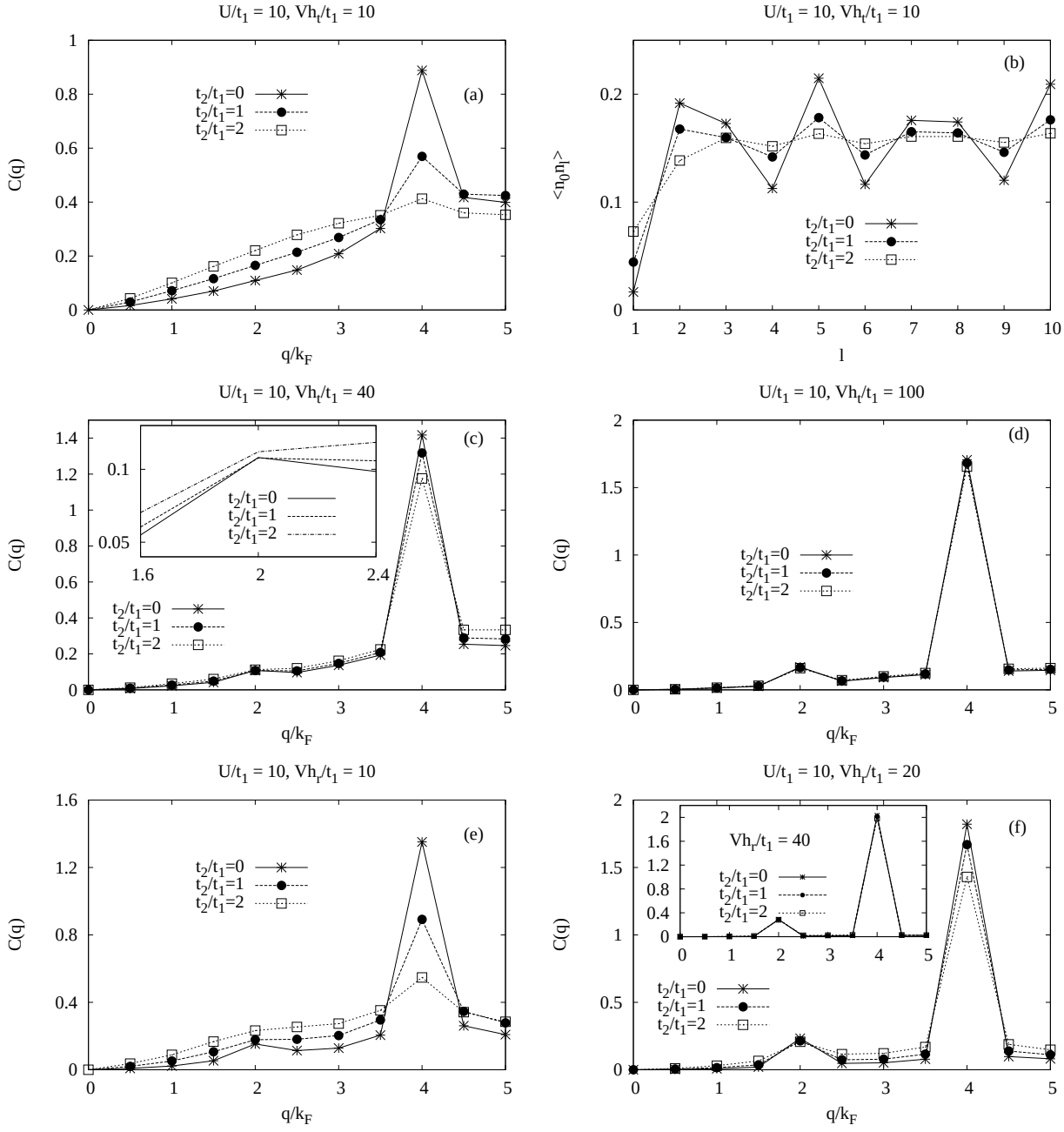

Figure 5.5.: (a) Static charge structure factor $C(q)$ for $Vh_t/t_1 = 10$ at different NNN hopping t_2. (b) Density-density correlation functions $C(l)$ for $Vh_t/t_1 = 10$ at various t_2 values. (c) and (d) $C(q)$ for $Vh_t/t_1 = 40$ and $Vh_t/t_1 = 100$, respectively for different t_2. At large magnitude, $Vh_t/t_1 = 100$, $C(q)$ is t_2/t_1 independant. The inset in Fig. 5.5 (c) shows the behavior of $C(2k_F)$, for $Vh_t/t_1 = 40$ at different t_2, in more detail. (e) and (f) show $C(q)$ at different t_2, for $Vh_r/t_1 = 10$ and $Vh_r/t_1 = 20$, respectively. The inset in Fig. 5.5 (f) shows the behavior of $C(q)$ for $Vh_r/t_1 = 40$ at different t_2. $C(q)$ is t_2/t_1 independant at $Vh_r/t_1 = 40$.

5.3.2. Spin correlations

5.3.2.1. Model I

- Effect of Vh_t/t_1

In order to study the spin degrees of freedom of the system, we now calculate the spin-spin correlation function defined by

$$S(l) = \langle S_i S_{i+l} \rangle \,. \tag{5.3}$$

The bare hole-hole Coulomb repulsion weakens the NN spin-spin correlation function $S(1)$ and at large magnitudes, the probability of having two NN spins is zero, $S(1) \sim 0$, as seen in Fig. 5.6 (a). This is consistent with the results for charge correlation functions of having no NN charges at larger magnitudes, whereas NNN spin-spin correlation function $S(2)$ is enhanced for $Vh_t/t_1 \leq 40$. At $Vh_t/t_1 = 100$, $S(2)$ becomes 0. $S(5)$, which now has an opposite sign regarding the case when repulsion is switch off, is enhanced. The decrease of $S(2)$ and $S(5)$ at large magnitudes is due to the fact that configurations, with different spin structures for NNN charges and for charges separated by the distance d, have a large weight in the ground-state. For instance $\downarrow$ 0 $\uparrow$, $\downarrow$ 0 $\downarrow$, and $\uparrow$ 0 $\uparrow$ as spin structures for NNN charges, and $\uparrow$ 0 $\uparrow$ 00 $\downarrow$, $\uparrow$ 0 $\downarrow$ 00 $\uparrow$, ... as spin structures for charges separated by d. $S(l)$, for large distance l, decreases upon increasing both repulsions.

The above results will have an effect on the static spin structure factor $S(q)$, the Fourier transform of the spin-spin correlation function $\langle S_i^z S_{i+l}^z \rangle$ with $S_i^z = (n_{i\uparrow} - n_{i\downarrow})/2$, and defined as

$$S(q) = \frac{1}{L} \sum_{il} \langle S_i^Z S_{i+l}^Z \rangle e^{iql} \tag{5.4}$$

$S(q)$ displays two peaks. A large and dominate peak at $2k_F$ and a small peak at $4k_F$. Upon increasing Vh_t/t_1, $S(2k_F)$ and $S(4k_F)$ increase for $Vh_t/t_1 < 100$. This behavior is different of that observed in Ref [13], where the magnitude of the singularity corresponding to the periodic ordering of the charges is progressively reduced, for different rational fillings, upon increasing the magnitude of the repulsion. But the LR Coulomb repulsion used there is e-e repulsion. Therefore, the two types of repulsion lead again to a different results. Indeed, Fig. 5.8 shows our calculation of $S(q)$, which now has a different singularity ($q = \pi$) as those observed for LR hole-hole interaction ($q = 2k_F, 4k_F$). Upon increasing Ve_t/t_1, the magnitude of $S(q)$ at the singulatity $q = \pi$ is reduced, which is consistent with Ref [13].

$2k_F$ which is 0.2 in units of the reciprocal lattice (u.r.l) vector $2\pi/c$ was also observed by INS [43, 40]. The $2k_F$ peaks saturate at $40 < Vh_t/t_1 < 100$) and are suppressed at $Vh_t/t_1 = 100$. The $4k_F$ peak is absent when the interaction is turned off and suppressed at $Vh_t/t_1 = 100$.

- Effect of Vh_r/t_1

The effect of the truncated repulsion is distinguishable from that of the bare repulsion in the fact that at very large Vh_r/t_1 ($40 \leq Vh_r/t_1 < 100$) values, $S(2)$ decreases while it remains almost the same for $Vh_t/t_1 < 100$. The $2k_F$ peaks saturate at $Vh_r/t_1 = 40$.

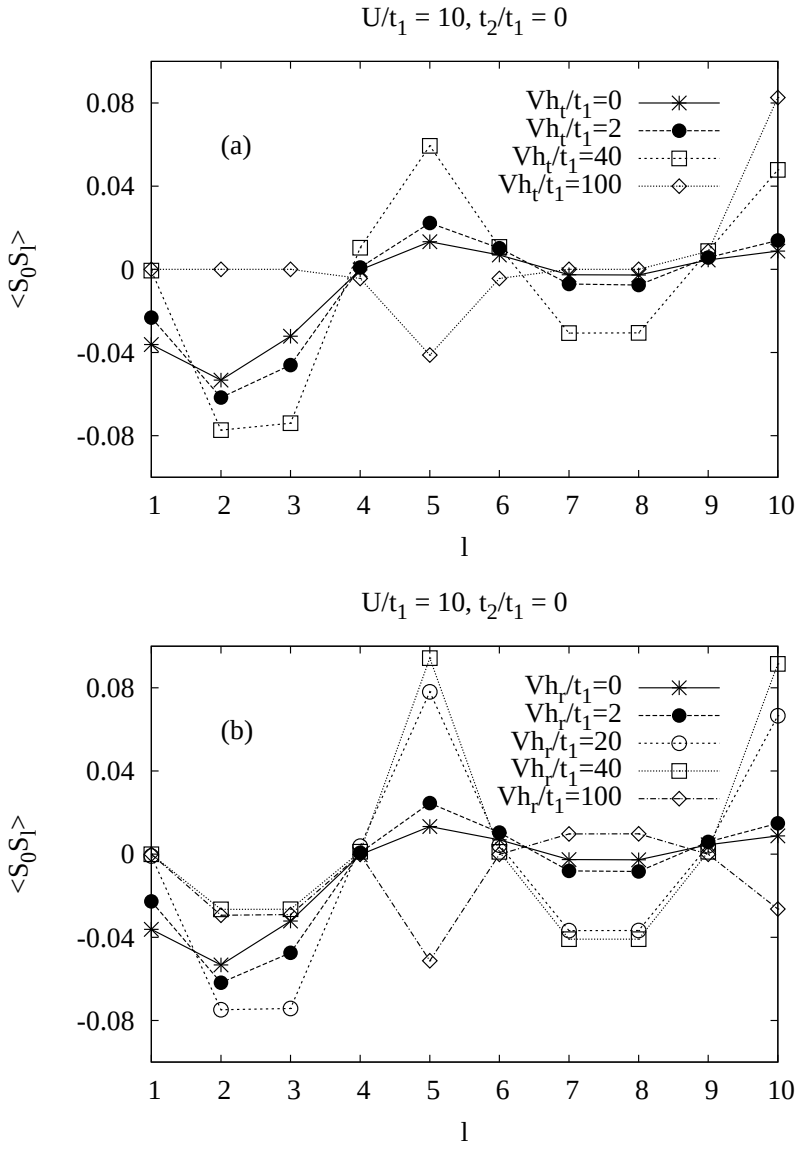

Figure 5.6.: Spin-spin correlation function $\langle S_0 S_l \rangle$. (a) at various Vh_t/t_1, and (b) at various Vh_r/t_1.

Hence, the WL CO is enhanced by large magnitudes. But on the other hand, the ground-state has no dimer structure. In what follows we will show the important influence of a NNN hopping t_2 on spin configurations.

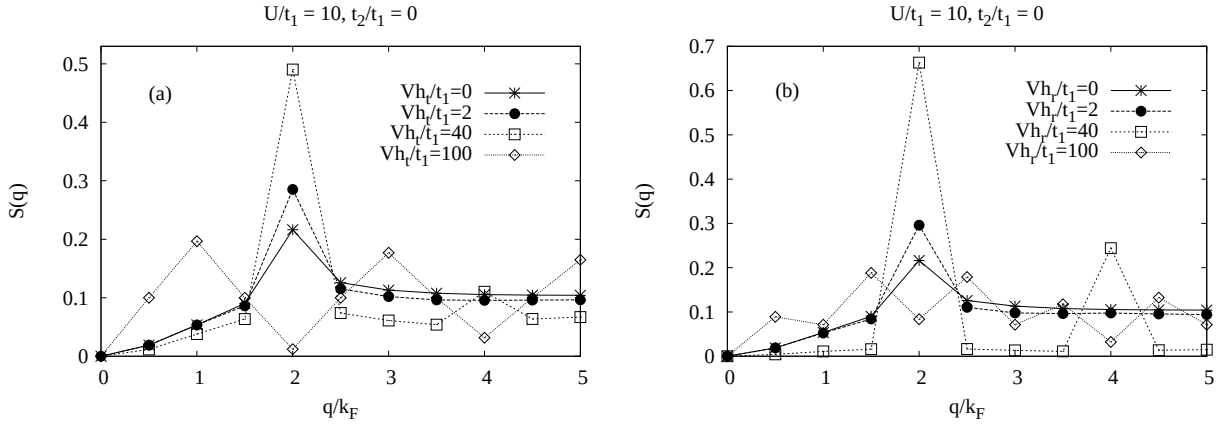

Figure 5.7.: Spin structure factor $S(q)$ at $t_2/t_1 = 0$. (a) for various Vh_t/t_1, and (b) for various Vh_r/t_1.

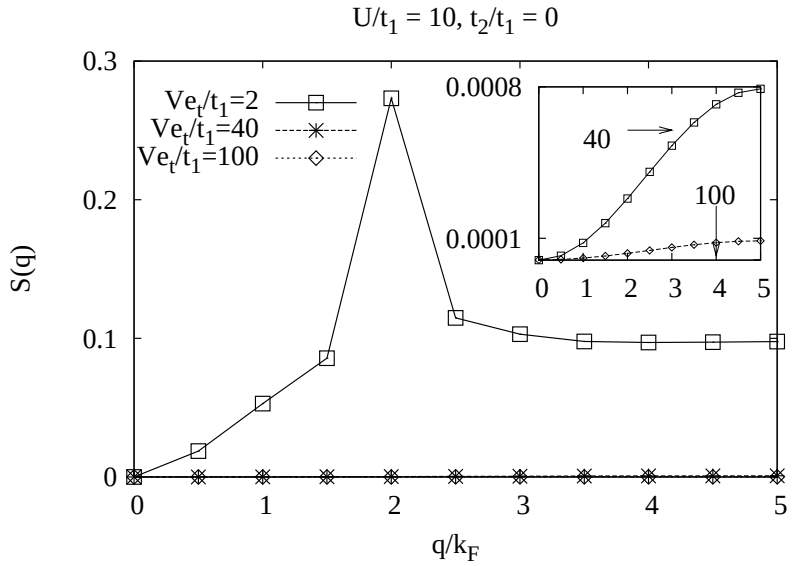

Figure 5.8.: Spin structure factor $S(q)$ for the LR e-e repulsion Ve_t/t_1 at $t_2/t_1 = 0$. The inset shows in more detail the behavior of $S(q)$ at $Ve_t/t_1 = 40$ and $Ve_t/t_1 = 100$, respectively.

5.3.2.2. Model II

The NNN hopping t_2 generates configurations where two charges may be a NN. Therefore $S(1)$ is increased for both interactions, the LR and truncated repulsions, respectively. For fixed $t_2/t_1 \neq 0$, both repulsions decrease distant correlations $S(l)$ as is shown in Figs. 5.9, 5.10, and Figs. 5.11. Upon increasing t_2/t_1, $S(l)$ decreases further. An apparent increase of $S(2)$ is seen at $Vh_t/t_1[Vh_r/t_1] = 40$.

For $S(q)$, the $2k_F$ and $4k_F$ peaks are both t_2/t_1 dependent.

- Effect of $t_2/t_1 \neq 0$ for Vh_t/t_1

Table 5.1.: The parameters A and B obtained from the fit for $Vh_r/t_1 = 100$ and different t_2/t_1 ratios. For each t_2/t_1 one can observe that $A \sim \langle S_i^z S_i^z \rangle$ and $B \sim \langle S_i^z S_{i+2}^z \rangle$

	A	B	$\langle S_i^z S_i^z \rangle$	$\langle S_i^z S_{i+2}^z \rangle$
$t_2/t_1 = 1$	0.0999745	-0.049699	0.099997	-0.049586
$t_2/t_1 = 2$	0.1000709	-0.0495118	0.099986	-0.049688

$S(2k_F)$ decreases under the effect of t_2, whereas $S(4k_F)$ stays unchanged for $Vh_t/t_1 \leq 40$. A noticeable effect of t_2 is observed for $Vh_t/t_1 = 100$, as shown in Fig. 5.12 (a), where t_2 restores a spin pattern as that obtained for intermediate magnitudes.

- Effect of $t_2/t_1 \neq 0$ for Vh_r/t_1

An interesting result is obtained at $Vh_r/t_1 = 100$, where distant correlations become negligible and the dominated correlation is $S(2)$, whereas for the same value for Vh_t/t_1, $S(3)$ and $S(5)$ are still of almost the same magnitude as $S(2)$.

For $Vh_r/t_1 = 100$, $S(q)$ becomes smooth and the singularity assigned at $2k_F$ has shifted to $2.5k_F$ and the $4k_F$ peaks are suppressed. This is in accord with Matsuda [39], who observed, in INS measurements, a maximum of the intensity around 0.25 in unit of reciprocal lattice (u.r.l) $2\pi/c$.

If the main contribution to $S(q)$ comes from $\langle S_i^z S_{i+2}^z \rangle$ then, from Eq. 5.4, $S(q)$ can be approximated by $S(q) \sim \langle S_i^z S_i^z \rangle + 2\langle S_i^z S_{i+2}^z \rangle \cos(2q)$. Therefore, we have fitted $S(q)$ by a function $F(q) = A + B\cos(2q)$ shown in Fig. 5.15. The table above shows the parameters A, B, $\langle S_i^z S_i^z \rangle$ and $\langle S_i^z S_{i+2}^z \rangle$.

Thus, the effect of t_2 on spin configurations for the bare Coulomb repulsion is less relevant to obtain a dimerized ground-state than for the truncated repulsion. We have obtained the WL CO state with dominated intradimer and week interdimer correlations ($S(2)/ \mid S(5) \mid = 27.92$) for very large Vh_r/t_1 and NNN hopping t_2. However, in our model, the WL CO configuration with the spin structure (shown in Fig. 5.1) suggested by INS, through the fit with a free dimer model, competes with configurations having other spin structures as it is shown below

$$
\begin{gathered}
00 \uparrow 0 \downarrow 00 \uparrow 0 \downarrow 00 \uparrow 0 \downarrow 00 \downarrow 0 \uparrow, \\
00 \uparrow 0 \downarrow 00 \uparrow 0 \downarrow 00 \downarrow 0 \uparrow 00 \downarrow 0 \uparrow; \\
00 \uparrow 0 \downarrow 00 \uparrow 0 \downarrow 00 \uparrow 0 \downarrow 00 \uparrow 0 \downarrow, \\
00 \uparrow 0 \downarrow 00 \downarrow 0 \uparrow 00 \uparrow 0 \downarrow 00 \downarrow 0 \uparrow
\end{gathered}
$$

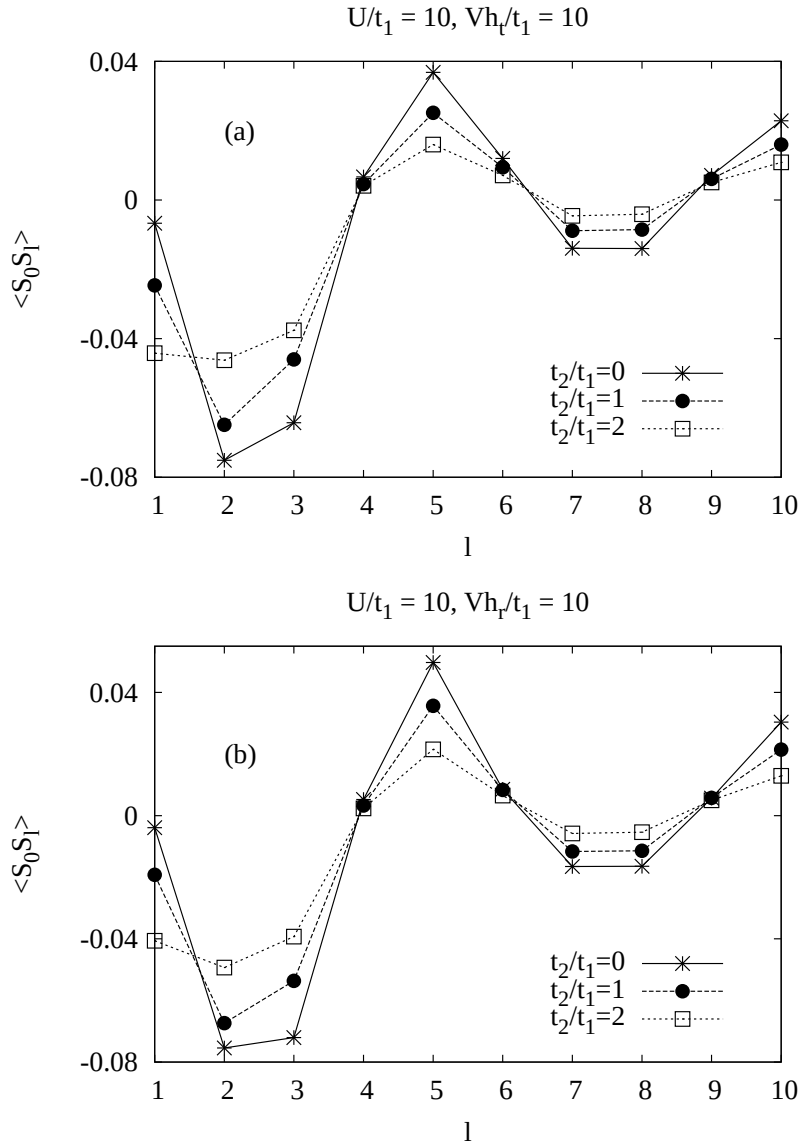

Figure 5.9.: Spin-spin correlation function $\langle S_0 S_l \rangle$. (a) for $Vh_t/t_1 = 10$ at various $t_2/t_1 \neq 0$, and (b) for $Vh_r/t_1 = 10$ at various $t_2/t_1 \neq 0$.

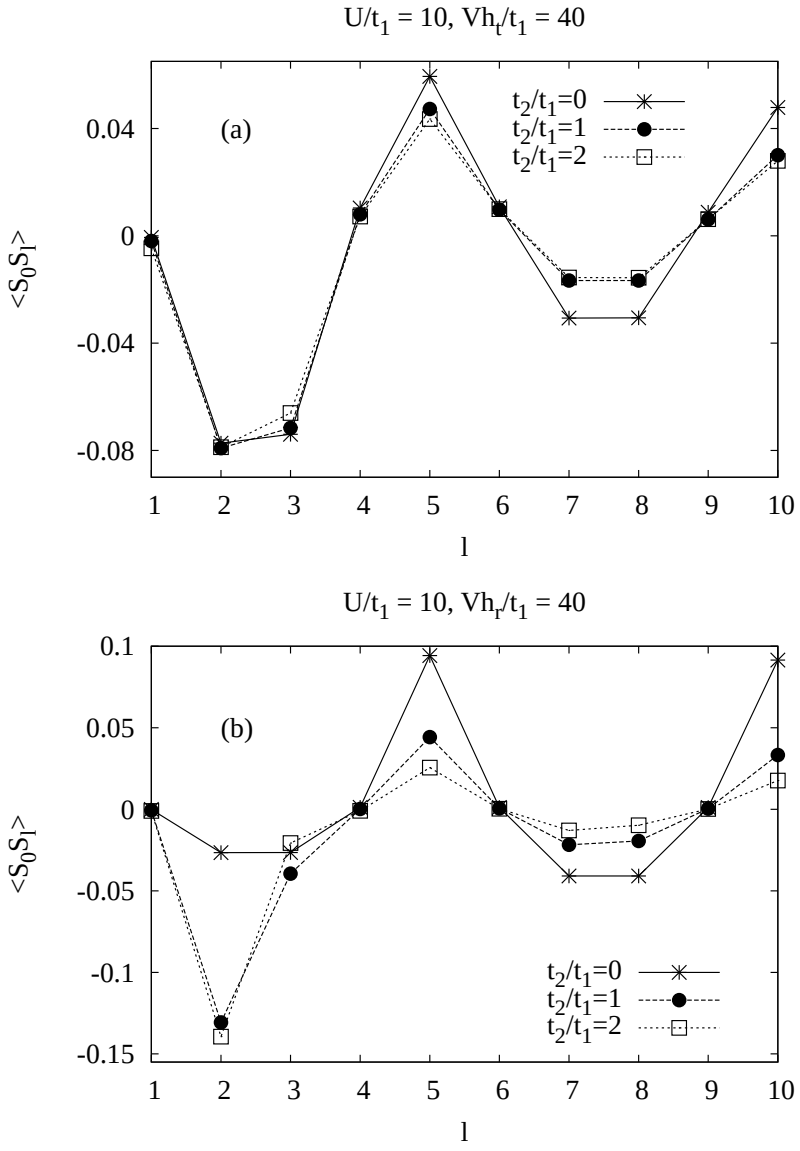

Figure 5.10.: Spin-spin correlation function $\langle S_0 S_l \rangle$. (a) for $Vh_t/t_1 = 40$ at various $t_2/t_1 \neq 0$, and (b) for $Vh_r/t_1 = 40$ at various $t_2/t_1 \neq 0$.

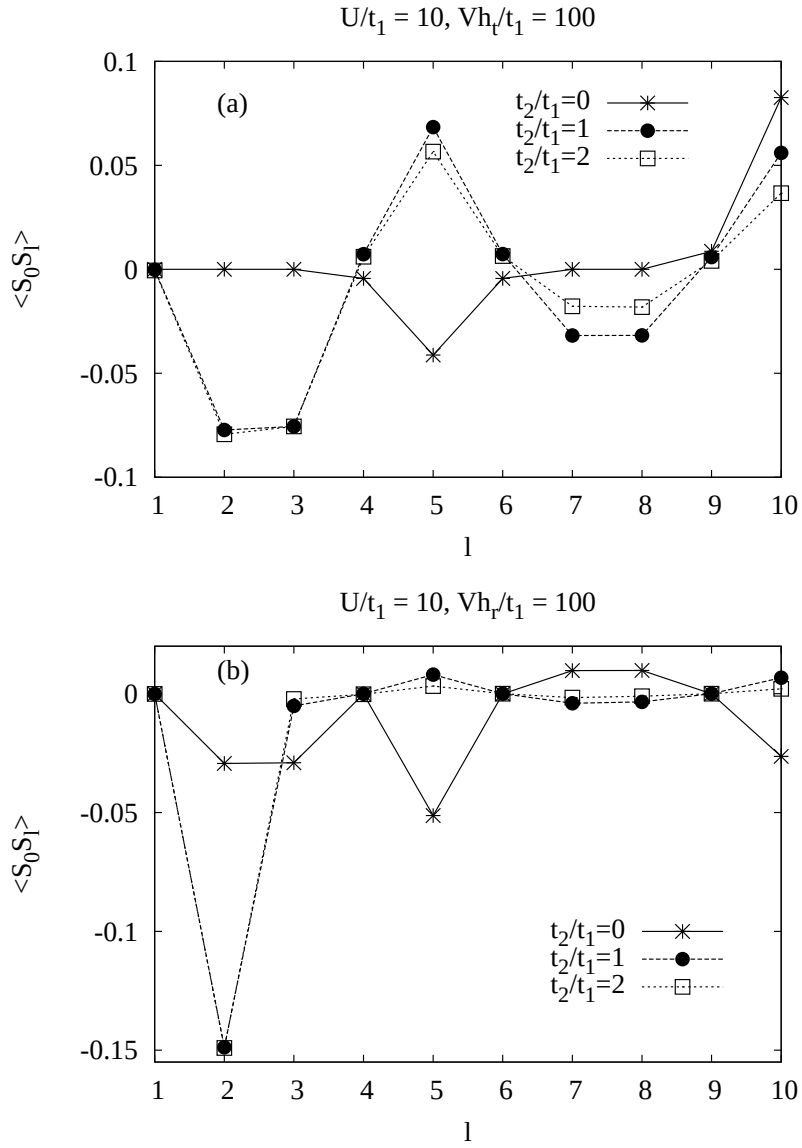

Figure 5.11.: Spin-spin correlation function $\langle S_0 S_l \rangle$. (a) for $Vh_t/t_1 = 100$ at various $t_2/t_1 \neq 0$, and (b) for $Vh_r/t_1 = 100$ at various $t_2/t_1 \neq 0$.

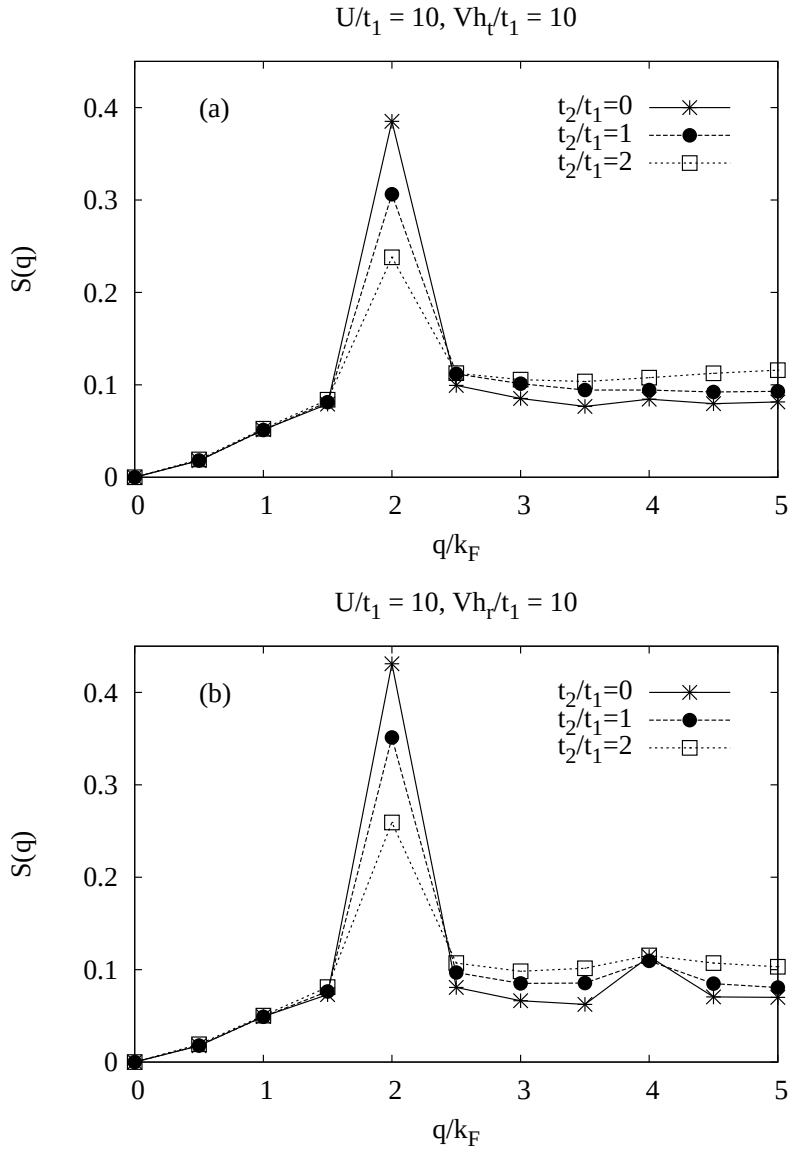

Figure 5.12.: Spin structure factor $S(q)$ at various t_2/t_1. (a) for $Vh_t/t_1 = 10$, and (b) for $Vh_r/t_1 = 10$.

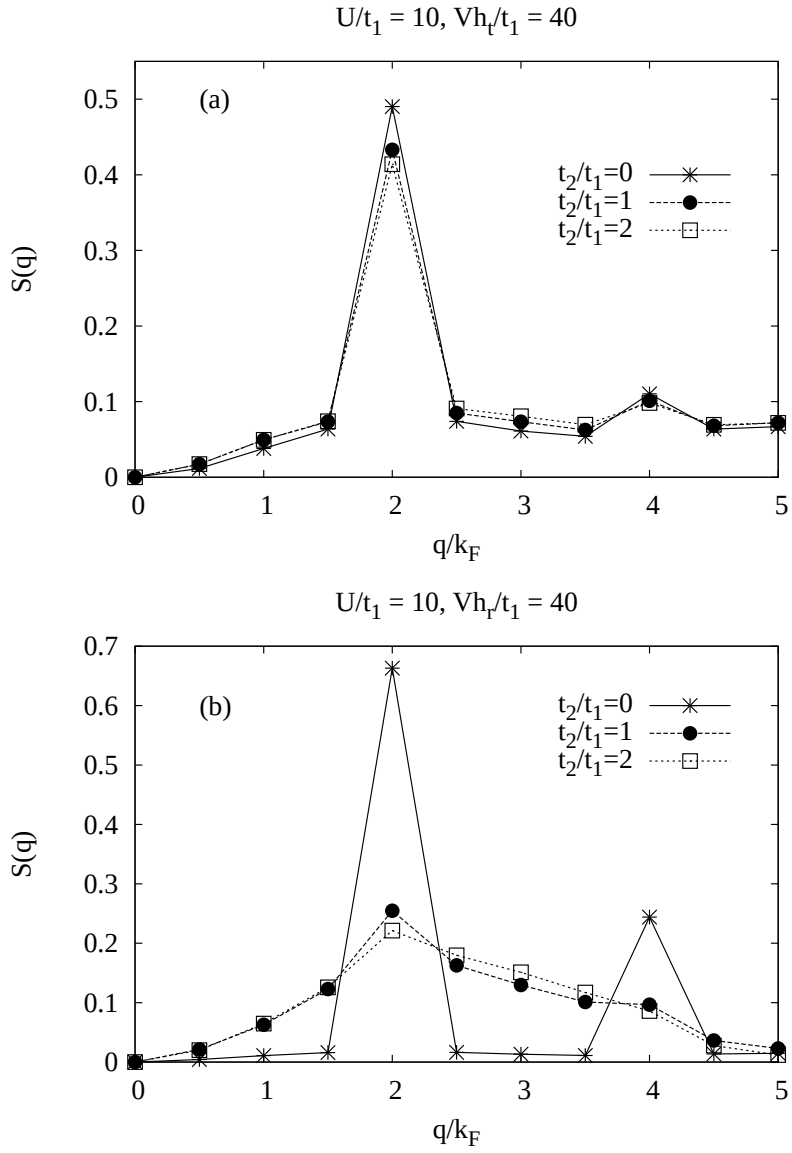

Figure 5.13.: Spin structure factor $S(q)$ at various t_2/t_1. (a) for $Vh_t/t_1 = 40$, and (b) for $Vh_r/t_1 = 40$.

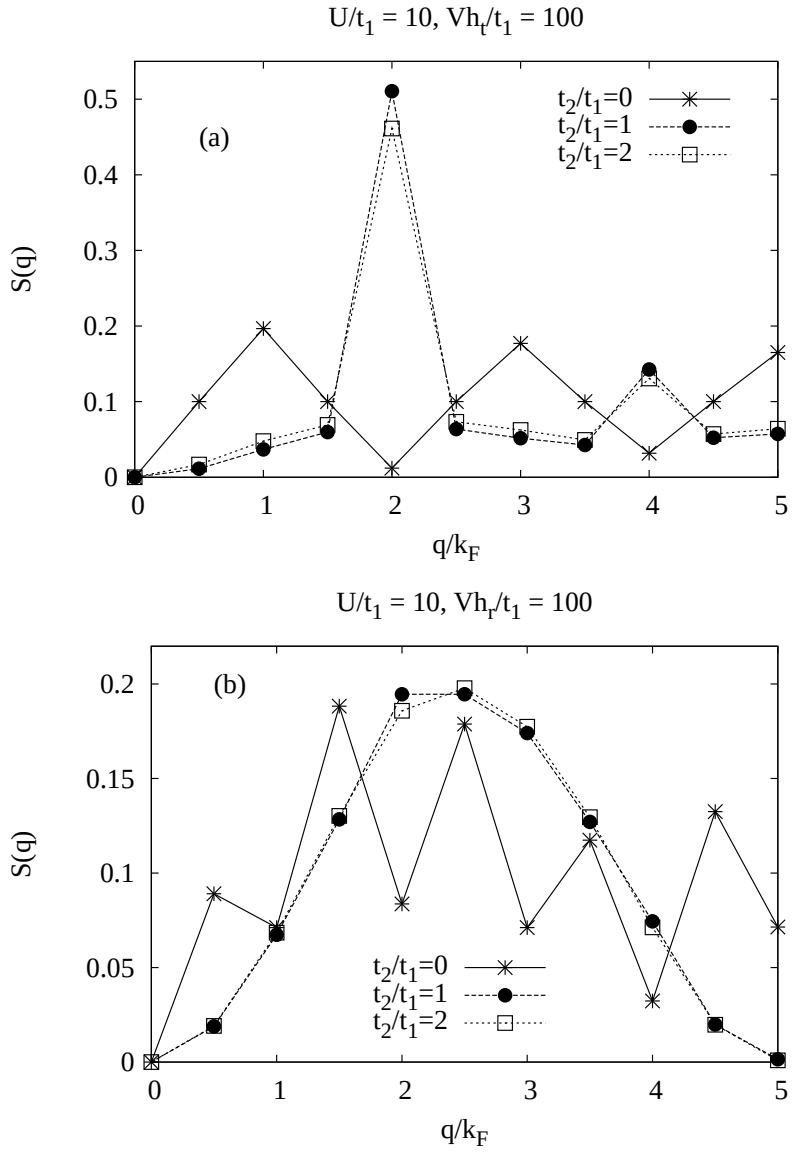

Figure 5.14.: Spin structure factor $S(q)$ at various t_2/t_1. (a) for $Vh_t/t_1 = 100$, and (b) for $Vh_r/t_1 = 100$.

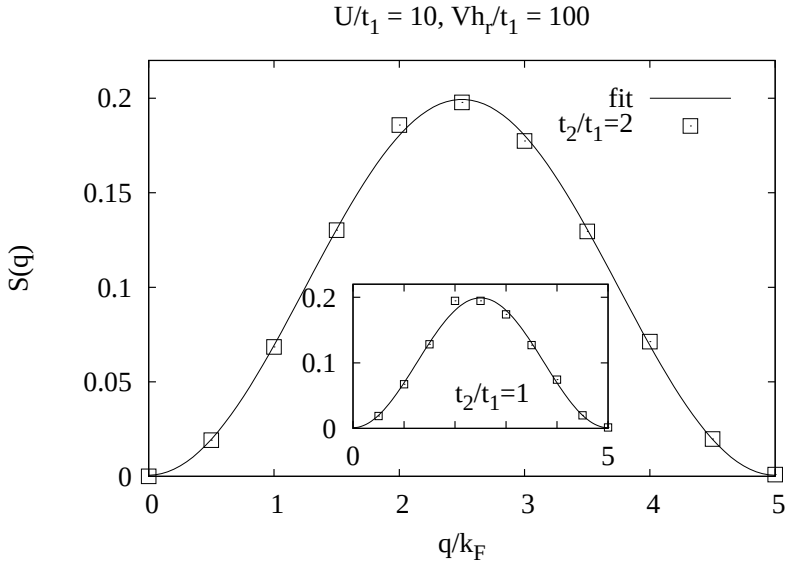

Figure 5.15.: Spin structure factor $S(q)$ for $Vh_r/t_1 = 100$ for $t_2/t_1 = 2$. The inset represents $S(q)$ for $t_2/t_1 = 1$. The full line in both plots represents a fit to an isolated dimers made up by two NNN spins.

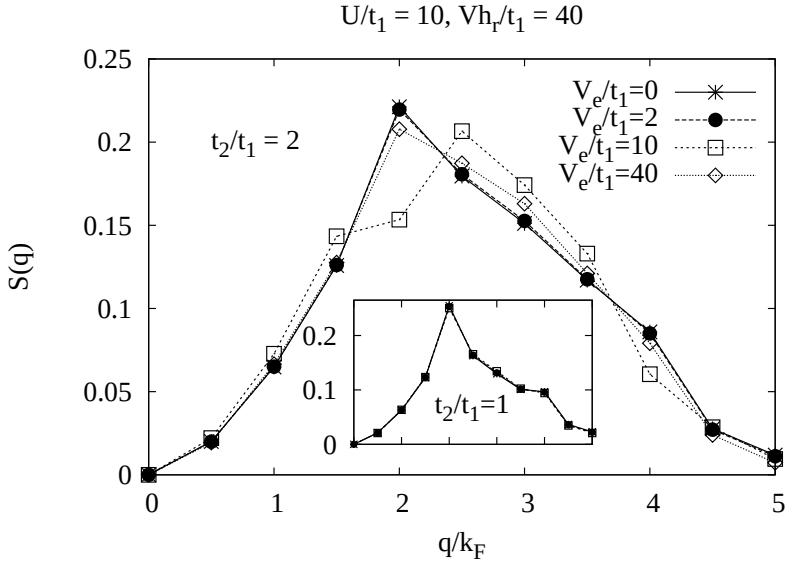

Figure 5.16.: Static spin structure factor $S(q)$ for $Vh_r/t_1 = 40, t_2/t_1 = 2$ and various V_{ee}/t_1. The inset shows the behavior od $S(q)$ for $t_2/t_1 = 1$ and various V_{ee}/t_1. Clearly V_{ee} has no effect on $S(q)$ for $t_2/t_1 = 1$.

5.3.2.3. Effect of V_{ee}

The short e-e repulsion $V_{ee} \neq 10$ has an effect for not too large Vh_r/t_1 values ($Vh_r/t_1 \leq 40$). It stabilizes the dimer formation as is shown in Fig. 5.16. It enhances $S(2k_F)$ but does not change its position. The behavior at small momenta remains the same and for $q > 2k_F$ the decrease becomes a bit slower for large V_{ee}/t_1 values. For $V_{ee}/t_1 = 10\,(V_{ee} = U)$ there is a shift of the maximum to $2.5k_F$. Thus, models with large values of Vh_r/t_1, together with NNN hopping t_2, and models with intermediate values of Vh_r/t_1 and NN e-e repulsion V_{ee} lead to a shift of the $2k_F$ peaks to $2.5k_F$.

To end this part, we study the effect of U on the CO and spin correlations for model I and II with the truncated repulsion, as this later is more relevant for the occurrence of WL CO accompanied with dimerization. The results show that for model I, the parameter U is irrelevant on charge and spin correlations. However, for small Vh_r/t_1, upon increasing U/t_1, the magnitude of $C(2k_F)$ and $S(2k_F)$ increases but with very tiny amount. An interesting result is observed for $Vh_r/t_1 = 40$ at $U/t_1 = 4$. In this case, the behavior of $S(q)$ is similar to that observed for $Vh_r/t_1 = 100$ at $U/t_1 = 10$.
$C(q)$ (not shown) stays unchanged upon varing U/t_1 as seen in Fig. 5.17.

The results are diffrent for model II. For small $Vh_r/t_1 < 8$, $C(2k_F)$ and $S(2k_F)$ are U/t_1 dependant. Not only the magnitude of $C(2k_F)$ and $S(2k_F)$ changes, but also the entire behavior depends on U/t_1 as seen in Figs. 5.18 and 5.19. However, for $Vh_r/t_1 > 4$, $C(q)$ and $S(q)$ stay unchanged upon varing U/t_1.

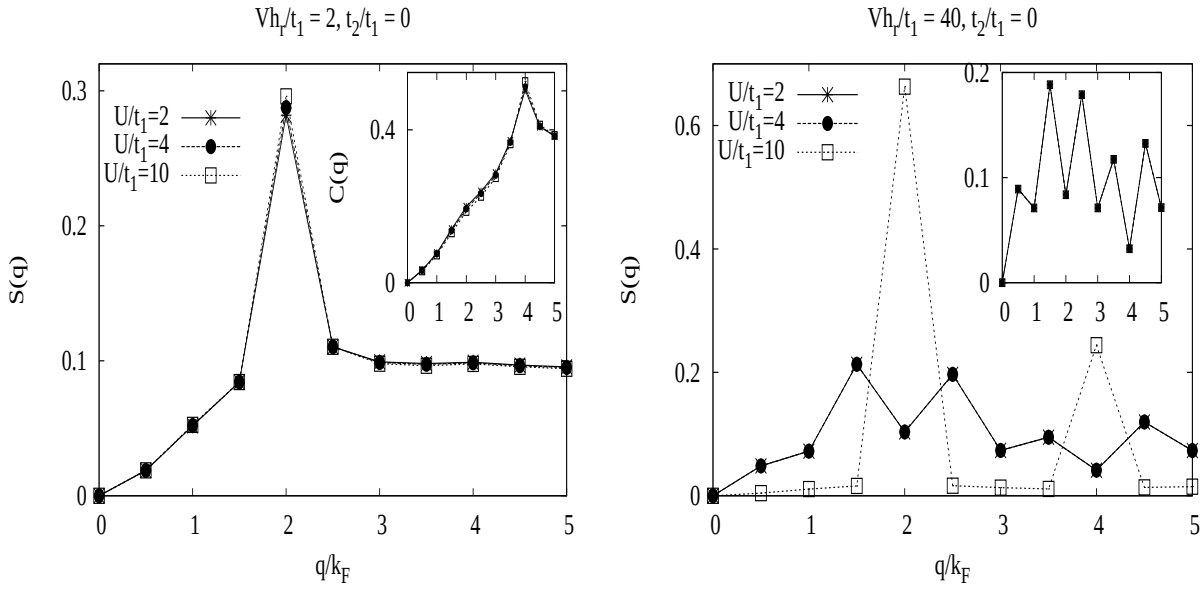

Figure 5.17.: Spin and charge structure factors $S(q)$ and $C(q)$ (shown in the inset), respectively, at $t_2/t_1 = 0$. (a) for $Vh_r/t_1 = 2$ at diffrent U/t_1. $S(2k_F)$ and $C(2k_F)$ are U/t_1 dependant. (b) for $Vh_r/t_1 = 40$ and $Vh_r/t_1 = 100$ (shown in the inset) at diffrent U/t_1. $C(q)$ (not shown) stays unchanged. The labels in the insets are the same as for the main figures.

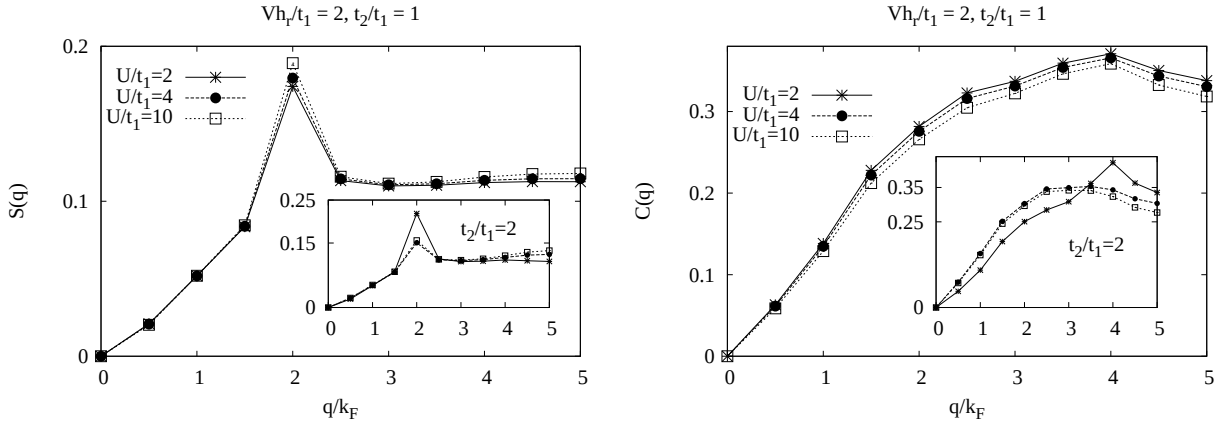

Figure 5.18.: Spin structure factor $S(q)$ and $C(q)$ for $Vh_r/t_1 = 2$ at $t_2/t_1 = 1$ and $t_2/t_1 = 2$ (shown in the inset), respectively, at different U/t_1. The labels in the insets are the same as for $t_2/t_1 = 1$.

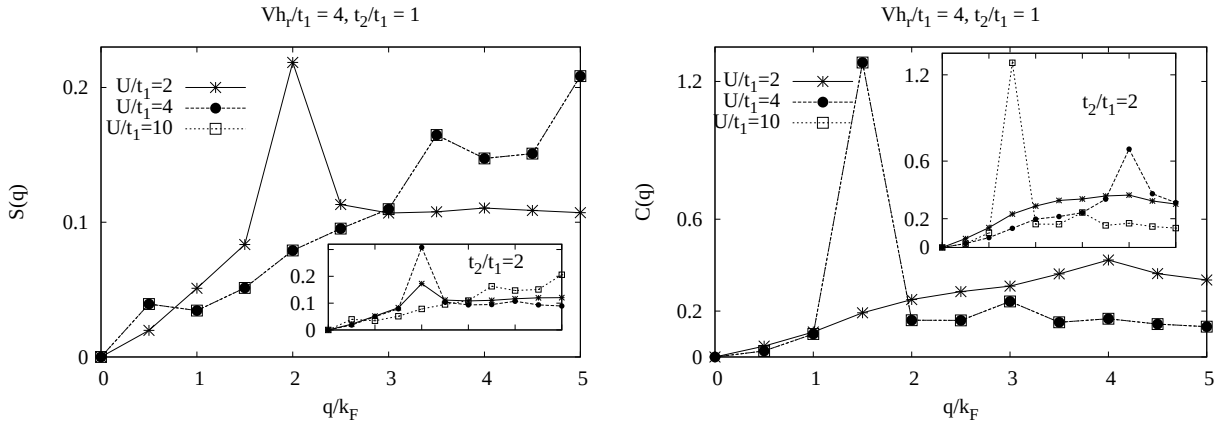

Figure 5.19.: Spin structure factor $S(q)$ and $C(q)$ for $Vh_r/t_1 = 4$ at $t_2/t_1 = 1$ and $t_2/t_1 = 2$ (shown in the inset), respectively, at different U/t_1. The labels in the insets are the same as for $t_2/t_1 = 1$.

To summarize this part conserning the charge and spin correlation functions, we have obtained results which are consistent with [23, 24], where Lee *et al* showed that in the case where the $2k_F$ and the $4k_F$ CDW may coexist on a single kind of 1d chain, one of four waves, a $4k_F$ CDW, and a $2k_F$ spin-density wave (SDW) will be dominant depending on the relative magnitudes of the repulsion. And waves other than the dominant type can coexist. Theories have shown that a $2k_F$ CDW, and a $4k_F$ SDW can grow in spite of a presence of e-e Coulomb repulsion [23, 24], and that its growth is assisted by the interchain repulsion [23, 24], which is not considered in our study.

The next step is to check the behavior of the charge and spin gaps, and critical exponent. We will consider only the truncated repulsion, as it is more relevant for the coexistence of WL CO and dimerization. Thus, we will restrict the calculation using model II for intermediate and large Vh_r/t_1 magnitudes. Due to the restriction to the density $\rho = 0.4$, we have data for 3 sizes only ($L = 10, 15, 20$). In addition, due to even-odd variations, we will consider, unfortunately,

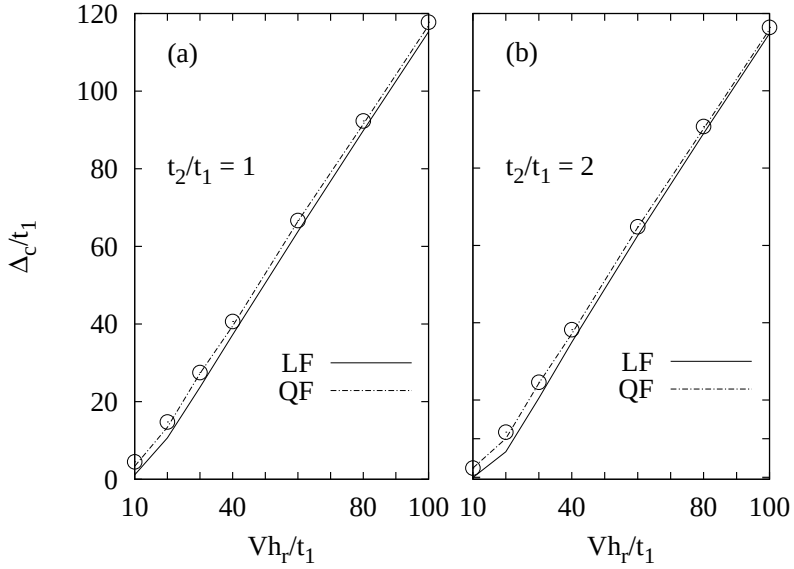

Figure 5.20.: Charge gap $\Delta_c(L)$ as defined in Eq. (5.5) for large Vh_r/t_1 values: (a) for $t_2/t_1 = 1$, (b) for $t_2/t_1 = 2$. The open circles correspond to finite size behavior, and the full and dashed lines represent LF and QF, respectively, to large limit.

only two sizes ($L = 10, 20$). So we cannot consider in a reliable way the limit of the infinite chain. Using data for larger sizes system, will be required to obtain more convincing results; however, this will be left for DMRG.

5.3.3. Charg gap

The charge gap is given by

$$\begin{aligned} \Delta_c(N;L) &= E_0(N+1;L) \\ &+ E_0(N-1;L) - 2E_0(N;L), \end{aligned} \tag{5.5}$$

where $E_0(M;L)$ denotes the ground-state energy of M particles on L sites. Our results for $\Delta_c(L)$ are shown in Fig. 5.20 for $10 \leq Vh_r/t_1 \leq 100$, together with the extrapolation to large L. A linear fit (LF) $A + B/L$ leads to unphysical negative value, which is due to the errors of the finite-size scaling, in case of $Vh_r/t_1 = 10$ and $t_2/t_1 = 2$, while such effect is absent with a quadratic fit (QF) $A + B/L^2$. $\Delta_c(L)$ increases with increasing Vh_r/t_1 in the considered parameter range. It is small at $Vh_r/t_1 = 10$ but stays finite for large system denoted by lines which represent the extrapolation to the thermodynamic limit. The full line corresponds to a linear fit and the dashed line to a quadratic fit. At large Coulomb repulsion, a charge gap clearly opens. Thus the insulating region is confined to large values Vh_r/t_1. The NNN hopping t_2 decreases Δ_c by a small amount.

5.3.4. Spin gap

The spin gap may be defined by

$$\Delta_s(N;L) = E_0(N_\uparrow + 1; N_\downarrow - 1; L) - E_0(N_\uparrow; N_\downarrow; L). \tag{5.6}$$

It corresponds to the energy needed to make a triplet excitation from the singlet ground-state. Generally, the spin gap is much smaller than the charge gap which is also the case here. So an accurate calculation is required. However, with the sizes that are available, it is not possible to distinguish any spin structure that will remain in the thermodynamic limit with a good accuracy. Other numerical techniques like DMRG are required. The calculated results for $\Delta_s(L)$ as a function of Vh_r/t_1 and t_2/t_1 are shown in Fig. 5.21. Δ_s fluctuates strongly with the number of sites. $\Delta_s(L=10)=0$ for any Vh_r/t_1. The ground-state is degenerate. While $\Delta_s(L=20)$ changes by varying Vh_r/t_1 in the parameter range shown in Fig. 5.21. One may observe the same qualitative behavior of $\Delta_s(L)$ for $t_2/t_1=1$ and $t_2/t_1=2$, whereas $\Delta_s^c(L)$ for $t_2/t_1=2$ is much larger than that for $t_2/t_1=1$ by an amount of 5.875 ($\Delta_s(L)$ for $t_2/t_1=2\sim 0.094, \Delta_s(L)$ for $t_2/t_1=1)\sim 0.016$. For fixed t_2/t_1, $\Delta_s(L=20)$ is almost zero at $Vh_r/t_1=10$ and increases to reach a maximum for a given magnitude Vh_r^c/t_1. The position and the magnitude of the maximum $\Delta_s(L)$ depend on the ratio t_2/t_1. For $t_2/t_1=1$, $Vh_r^c/t_1=50$. While for $t_2/t_1=2$, $Vh_r^c/t_1=40$. On the other hand, the spin gap observed for the 1D chain in SCO is about $\Delta_s^{exp}\sim 140$K, which corresponds to $0.12\mathrm{t}_1$ (assuming $\mathrm{t}_1\sim 0.1$ eV, to be consistent with band calculation in [34]). Our numerical results show that the finite-size spin gap for $Vh_r/t_1=40$, $V_{ee}/t_1=10$, and $t_2/t_1=1$ is about $\Delta_s\sim 0.124\mathrm{t}_1$. Also for larger magnitudes, when V_{ee} is not considered, $\Delta_s^c(L)\sim 0.127t_1$ for $Vh_r/t_1=90$ at $t_2/t_1=1$. While the result for the large L limit obtained for $Vh_r/t_1=100$ by the quadratic fit gives a value about $\sim 0.124t_1$. The linear fit gives larger values than Δ_s^{exp}. So, from these finite-size results and their quadratic extrapolation to large L limit, a gaped spectrum may be obtained at larger magnitudes ($Vh_r/t_1>10$) where the system contains singlet pairs as seen from the behavior of the spin-spin correlation functions. A close finite-size results to Δ_s^{exp} can be obtained within our model II for $t_2/t_1=1$ at $Vh_r/t_1=40$ and $Ve=10t_1$, or for $80<Vh_r/t_1<90$. If the QF reflects the true large L limit then a close value to Δ_s^{exp} can ne obtained for $90<Vh_r/t_1<100$. Thus, more calculations should be performed to get more accurate results for Δ_s.

5.3.5. Critical exponent

In order to examine further the ground-state properties, we present in this subsection calculations of the parameter K_ρ which, within the Tomonaga-Luttinger liquid (TLL) theory [63], is related to the compressibility κ through

$$K_\rho=\frac{\pi}{2}v_c\kappa, \tag{5.7}$$

where v_c is the charge velocity. The charge compressibility κ is defined as the second derivative of the ground-state energy E_0 with respect to the density of particles

$$\frac{1}{\kappa}=\frac{1}{L}\frac{\partial^2 E_0}{\partial n^2}. \tag{5.8}$$

A convenient finite-size approximation of the compressibility κ is

$$\kappa=\frac{L}{N^2}\left(\frac{E_0(N+2;L)+E_0(N-2;L)-2E_0(N;L)}{4}\right)^{-1}. \tag{5.9}$$

The charge velocity is obtained from

$$v_c=(E_{1,S=0,Q+2\pi/L}-E_{0,S=0,Q})/2\pi/L, \tag{5.10}$$

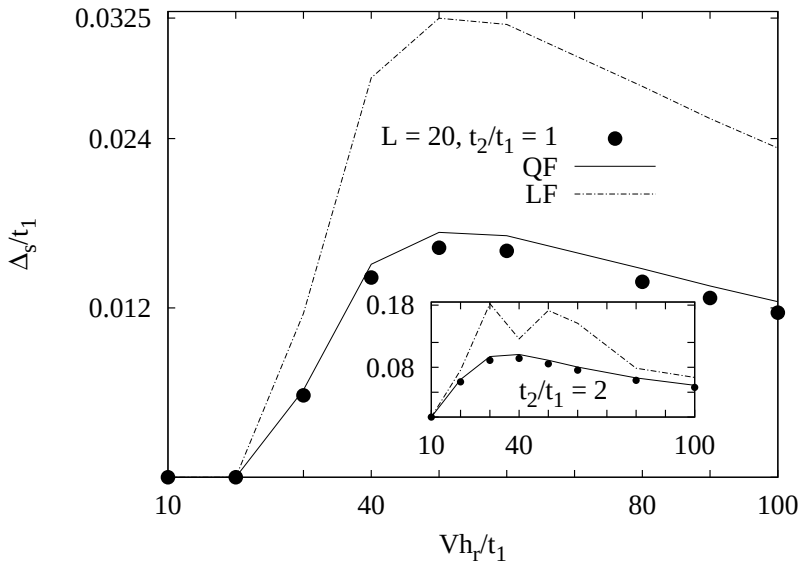

Figure 5.21.: (a) spin gap $\Delta_s(L)$ as defined in Eq. (5.6) for large Vh_r/t_1 values and $t_2/t_1 = 1$, the inset corresponds to $\Delta_s(L)$ for $t_2/t_1 = 2$. The full and open circles correspond to finite size behavior, while the full line reprents the fit to large limit. The dotted line in the inset is guide to the eye.

where $E_{1,S=0}$ is the energy of the first singlet excited state with momentum $2\pi/L$ measured from the ground-state with momentum Q.
We can treat only at most 20 sites using Lanczos ED technique. Therefore, it is difficult to determine K_ρ accurately. The calculated results for the TL parameter as a function of Vh_r/t_1 are shown in Fig. 5.22. We have plotted only QF due to the fact that LF leads to many negative unphysical values of K_ρ at $t_2/t_1 = 2$. K_ρ decreases by increasing the magnitude of the repulsion. Thus, large hole-hole Coulomb repulsions suppress the value of K_ρ. The decrease is large and faster for $10 < Vh_r/t_1 \leq 40$ at $t_2/t_1 = 1$, and for $10 < Vh_r/t_1 \leq 20$ at $t_2/t_1 = 2$. The enhancement of the NNN hopping leads to a larger decrease of K_ρ. For all parameter range, $K_\rho \ll 1$ which is consistent with the insulating behavior and the dominant fluctuations which are $2k_F$- and $4k_F$-CDW.

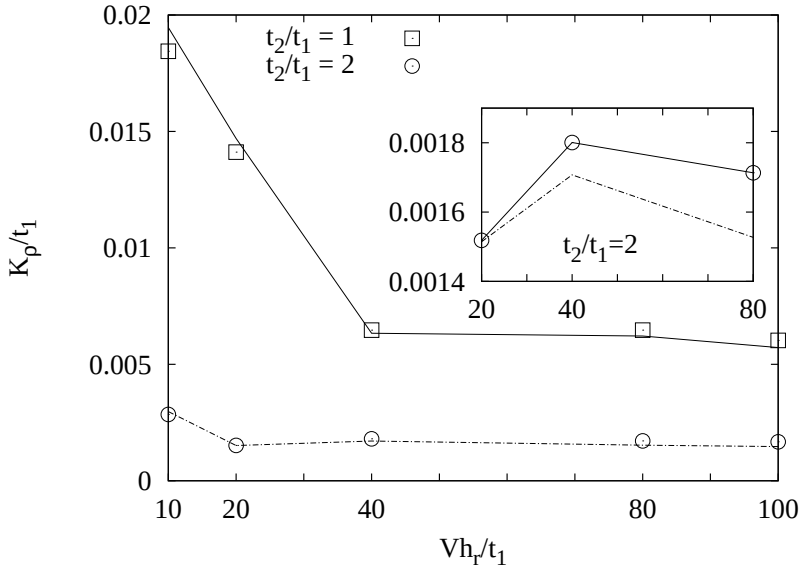

Figure 5.22.: Critical exponent $K_\rho(L)$ as defined in Eq. (5.7) together with its extrapolation for large Vh_r/t_1 values. The open circles and squares correspond to finite size behavior for $t_2/t_1 = 1$ and $t_2/t_1 = 2$, respectively, while the dotted and full lines reprent their extrapolation, respectively. The inset shows in more detail the behavior of $K_\rho(L)$ and its extrapolation in parameter range $40 \leq Vh_r/t_1 \leq 80$.

6. ED studies of doped Heisenberg spin rings

6.1. Introduction

In this chapter, we want to introduce a Heisenberg model which parametrically depends on hole positions. If the electrostatic hole-hole repulsion is included such a model allows to evaluate all energy eigenvalues and eigenstates (for small system size) and thus enables us to evaluate thermodynamic properties as function of temperature, magnetic field, and doping. Assuming certain exchange constants we can investigate the influence of the electrostatic hole-hole repulsion on ground state properties as well as on thermal averages like the magnetization which include contributions of low-lying spin-hole configurations.

6.2. Model system

There are various ways to model a system of holes and spins, among them are the (multiband) Hubbard model and classical spin dynamics models. In this chapter the chain of holes and spins is modeled in the following way. Each configuration $\vec{c}$ of holes and spins defines a Hilbert space which is orthogonal to all Hilbert spaces arising from different configurations. The Hamilton operator of a certain configuration is of Heisenberg type and depends parametrically on the actual configuration $\vec{c}$, i. e.

$$\underset{\sim}{H}(\vec{c}) \;=\; -\sum_{u,v} J_{uv}(\vec{c})\; \underset{\sim}{\vec{s}}(u) \cdot \underset{\sim}{\vec{s}}(v)\;. \tag{6.1}$$

This ansatz is similar to a simple Born-Oppenheimer description where the electronic Hamiltonian (here spin Hamiltonian) depends parametrically on the positions of the classical nuclei (here hole positions). In (6.1) $J_{uv}(\vec{c})$ are the respective exchange parameters. In this chapter three exchange parameters are considered: $J = -67$ K is the antiferromagnetic coupling across a hole ($J = -64$ K and $J = -70$ K have been also considered), $J_{\|} = 5.8$ K is the ferromagnetic coupling across two holes. The values of these exchange parameters are in accord with other theoretical and experimental investigations of this compound [64]. For the ferromagnetic coupling between spins not separated by a hole we are using $J_{NN} = 8.7$ K, which is similar to the coupling used in Ref. [38]. A recent mean field analysis suggests that this exchange constant may be stronger [65].

The electrostatic interaction between holes is modeled by a potential energy

$$V(\vec{c}) \;=\; \frac{e^2}{4\pi\epsilon_0\,\epsilon_r\,r_0}\frac{1}{2}\sum_{u\neq v}\frac{1}{|u-v|}\;, \tag{6.2}$$

where $r_0 = 2.75$ Å is the distance between NN sites on the ring and ϵ_r is the dielectric constant. Several attempts have been undertaken to estimate the dielectric constant which yielded values for ϵ_r up to 30 [66, 67, 68]. In related projects where the exchange interaction of chain systems in cuprates is derived from hopping matrix elements between different orbitals using a Madelung potential the dielectric constant is found to be 3.3 [69, 33].

For small systems all hole configurations can be considered and the related spin Hamiltonians (6.1) can be diagonalized completely. For 8 spins and 12 holes this amounts to 6310 distinct hole configurations and tiny Hilbert spaces of dimension 256. For 12 spins and 18 holes the total number of hole configurations is already too big to be considered completely. Therefore, only the dimer configuration and low-lying excitations with their respective degeneracies are taken into account. It will turn out that the high degeneracy of excited hole configurations plays an important role, since they substantially contribute to observables at low temperature although lying rather high in energy.

6.3. Numerical simulation and results

As an application we investigate spin rings where 60 % of the chain sites are occupied by holes. The ground state hole configuration for this compound is the so-called dimer configuration. In order to obtain this result it is necessary to consider the full Coulomb interaction. If one for instance tries to model the Coulomb interaction by a NN repulsion, then the ground state is given by an antiferromagnetic chain and a cluster of the remaining holes, irrespective how big the NN interaction is. Even the inclusion of NNN does not improve the situation, the Coulomb interaction is still proportional to the number of sites and may be overcome by the antiferromagnetic binding. We also find that the Coulomb interaction has to be sufficintly strong in order to yield the dimer configuration as the ground state. These results are consistent with those obtained by using EHM (see Chap. 5). The following examples shows that this is indeed the case, the Coulomb interaction is only weakly screened.

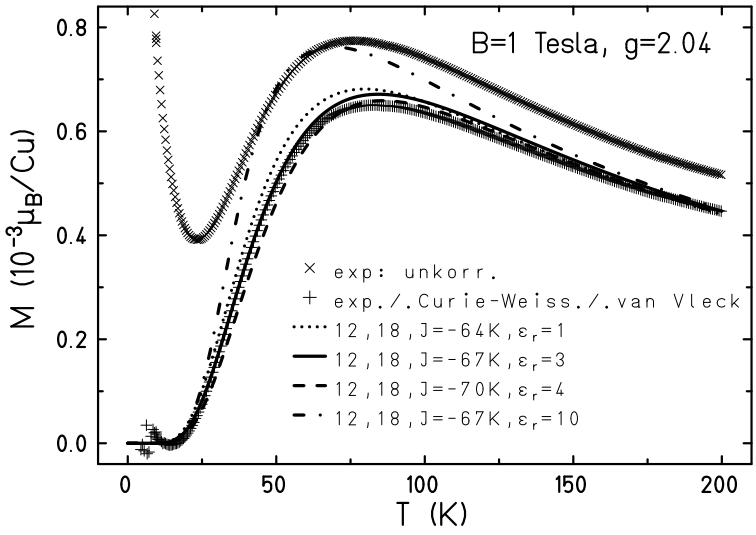

Figure 6.1.: Magnetization versus temperature for $B = 1$ Tesla: Experimental data ($\vec{B} \parallel$ c-axis) are given by x-symbols and crosses (corrected for Curie-Weiss and van-Vleck magnetism) [64]. For $N_\mathrm{s} = 12$ and $N_\mathrm{h} = 18$ magnetization curves are displayed for a range of exchange parameters $J = -64, -67, -70$ K and several dielectric constants ϵ_r.

Figure 6.1 shows the temperature dependence of the magnetization at $B = 1$ Tesla for a system of 30 sites with $N_\mathrm{s} = 12$ spins and $N_\mathrm{h} = 18$ holes. The experimental data points for

the infinite system ($\vec{B} \parallel$ c-axis) are given by x-symbols and crosses (corrected for Curie-Weiss and van-Vleck magnetism) [64]. The latter can be very accurately approximated by an ansatz which describes the magnetic part as noninteracting antiferromagnetically coupled dimers [64]. Nevertheless, the additional ferromagnetic coupling $J_{\parallel} = 5.8$ K as well as other spin hole configurations also contribute to the magnetization and change the picture accordingly. If the Hamiltonian of the 12-spin system is diagonalized completely and Coulomb interaction is taken into account, one finds that the magnetization depends rather strongly on J and ϵ_r. Figure 6.1 displays magnetization curves for a range of exchange parameters $J = -64, -67, -70$ K and several dielectric constants ϵ_r. For $\epsilon_r = 1$ only the dimer configuration contributes. For $\epsilon_r \gtrsim 3$ several hole configurations contribute with their respective magnetic spectra. For practical purposes only those configurations have been taken into account whose Coulomb energy differs by less than 500 K from the ground state Coulomb energy. It seems that a dielectric constant of the order of $\epsilon_r \approx 3$ is best suited to describe the magnetization data. This result is in good agreement with a dielectric constant of 3.3 found in Refs. [69, 33].

Figure 6.2 illustrates which configurations contribute for $\epsilon_r = 3$ at lower energies. These configurations, although rather high in energy, nevertheless contribute with substantial weight, since they are highly degenerate. The degeneracy for configurations where one hole is moved is of order N_{tot}, the degeneracy for configurations where two holes are moved is of order $N_{\mathrm{s}} \cdot N_{\mathrm{tot}}$.

In order to estimate the influence of the finite size of the ring system we computed the magnetization for a larger ring with $N_{\mathrm{s}} = 16$ and $N_{\mathrm{h}} = 24$ which does not differ from the respective one with $N_{\mathrm{s}} = 12$ and $N_{\mathrm{h}} = 18$, therefore it seems to be justified to assume that finite size effects do not play a role for the magnetization at this size.

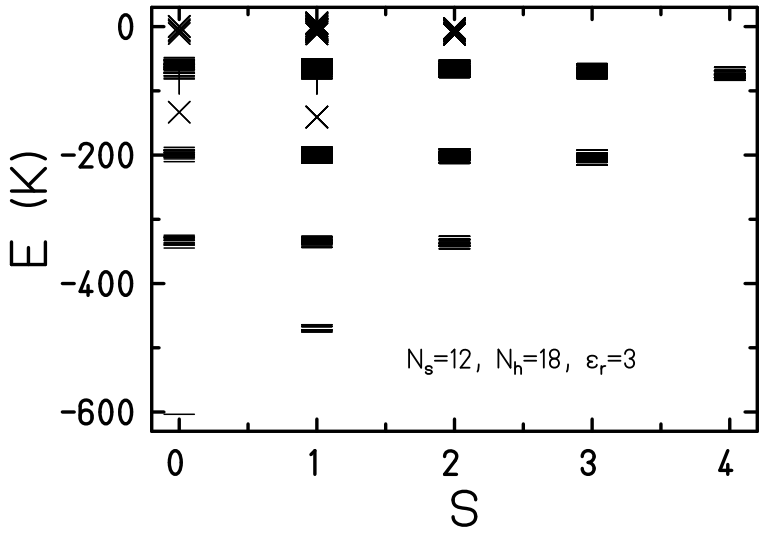

Figure 6.2.: Low-lying energy levels for $J = -67$ K and $\epsilon_r = 3$: The dashes denote magnetic levels of the dimer-configuration, x-symbols show levels for configurations where one hole is moved, the crosses mark levels for two holes moved. The first triplet excitation is split into four levels with the following excitation energies (and degeneracies): 128 K (3), 131 K (6), 136 K (6), and 139 K (3).

7. Summary and discussion

The aim of the present work was to investigate the low-density system of a chain with periodic boundary conditions using exact diagonalization (ED). We restricted ourself to a very special density, $\rho = 0.4$. Our motivation behind such restriction was to investigate an experimental discrepancy about the structure of the dimers in the chains of $Sr_{14}Cu_{24}O_{41}$ (SCO) compound which was already introduced in the former chapters. The arrangement of the dimers in the chain was discussed mainly with two possible models provided by **NMR** studies. The first model is that each dimer is separated by one ZR singlet (model I), in which a lattice distortion with 4 times the periodicity of the chain structure is required, and this was supported by lattice distortion measurements. The second is that the dimers are separated by two ZR singlets (model II), in which a lattice distortion with 5 times the periodicity of the chain structure is required, and this is consistent with studies of magnetic excitations by using INS. The common agreement between different experiments is that the chains have a dimerized ground-state with charge ordering (CO) and spin gap of about 140K, and that SCO shows an insulating behavior at low temperature.

The first part of our work was to check out whether a model appropriate for strongly correlated electrons in 1d and with the electron density $\rho = 0.4$, may show the same qualitative aspects as the experimental findings. And if so, which model parameters are responsible for dimerization and charge ordering?

For that aim, we have studied the spin and charge correlations of a chain in an extended Hubbard model (EHM), of which even a rough feature is not known so far. By proposing the model, we have considered the localization of the holes in the chains of SCO and the structure of the edge-sharing corner CuO_2. This structure allows a large next-nearest neighbour (NNN) hopping. Therefore the Coulomb repulsion between holes and NNN hopping are constituents of the EHM. Our numerical results from the ED calculations show that the model has the CO Wigner lattice (WL) type which is consistent with model II at large Coulomb repulsion between holes. This WL CO is obtained for the bare Coulomb interaction as well as for the Coulomb interaction truncated at the fourth neighbour. However, WL CO is stabilized by the truncated repulsion. The formation of dimers is a result of a competition between the hole-hole Coulomb repulsion and the NNN hopping. The later enhances largely the intra-dimer spin-spin correlations and weakens the distant interdimer correlations. When hole-hole Coulomb repulsion is not too large, a short e-e repulsion is needed to stabilize the dimer formation. However, not all NNN spins form a dimer. The ground-state has still a number of NNN charges having the same spins. We have also found that the system shows an insulating behavior for intermediate and large repulsions through the behavior of the charge gap. This result is consistent with the calculation for the Tomonaga-Luttinger liquid (TLL) critical exponent K_ρ which becomes too small, compared to its value in the bare Hubbard model, for large magnitudes of the repulsion. However, a possible finite spin gap can be obtained only for very large interaction. To refine the model, we would like as a next step, to introduce a NNN magnetic coupling to eliminate the NNN charges with the same spin, and hence increase the magnitude of the spin gap.

The second part of our work was to start with the assumption that charges are frozen in the chains of SCO, and to consider the CO proposed in model II. For that we have proposed a Heisenberg model which depends parametrically on hole positions. It includes the electrostatic repulsion between holes and allows to evaluate thermodynamic properties as function of temperature, field, and doping. As a first application the influence of the electrostatic repulsion between holes on the temperature dependence of the magnetization is investigated. We find that the dielectric constant is approximately $\epsilon_r \approx 3$ in order to reproduce the magnetization for 60 % holes on the ring. Since the proposed model depends at least on four parameters $(J, J_{\|}, J_{NN}, \epsilon_r)$ the comparison to one magnetization curve leaves some freedom for the precise values. In future projects we are attempting to refine the model in order to obtain a consistent description of the meanwhile accumulated magnetization data. A direct measurement of the energy needed to excite hole movements, compare would be very valuable since it would put additional restrictions on the range of the dielectric constant ϵ_r. It is our hope that a refined model will allow more insight into the interplay of charge order and magnetism.

List of Figures

A. Symmetries in the Hubbard model

In the process of constructing a representation for the Hamiltonian it is very useful to take advantage of the model symmetries. The 1D Hubbard Hamiltonian has a number of symmetries with a corresponding set of conserved quantities which makes it exactly integrable. These symmetries reduce the size of the matrix Hamiltonian to a block form and hence allow, using numerical methods, to compute a large sizes. Below, we discuss some of these discrete symmetries.

A.1. Discrete transformations

A characteristic feature of the Hubbard Hamiltonian on a chain consisting of an even number of sites is its invariance under the transformation

$$c_{j\uparrow} \to c_{j\uparrow} \qquad c_{j\downarrow} \to (-1)^j c_{j\downarrow} \qquad U \to -U\,. \tag{A.1}$$

The model exibit also conservation of total spin number, total spin in the z-direction and total charge, i.e.,

$$\left[\mathcal{H}, \boldsymbol{S}^2\right] = \left[\mathcal{H}, S^z\right] = \left[\mathcal{H}, \hat{N}\right] = 0\,, \tag{A.2}$$

where

$$\begin{aligned} \boldsymbol{S} &= \sum_i \boldsymbol{S}_i\,, \\ \hat{N} &= \sum_i n_i\,. \end{aligned} \tag{A.3}$$

In addition, these operators also commute with one another, i.e.,

$$\left[\boldsymbol{S}^2, S^z\right] = \left[S^z, \hat{N}\right] = \left[\hat{N}, \boldsymbol{S}^2\right] = 0\,, \tag{A.4}$$

so that the eigenvalues of $\mathcal{H}, \boldsymbol{S}, S^z$, and $\hat{N}$ are simultaneous good quantum numbers.

A.1.1. Spin-Rotational Invariance

If terms are invariant when the coordinate axes of the spin are rotated, then they are invariant when the spin is rotated. Thus, We will obtain a remarkable spin symmetry.

The two terms of the Hubbard model the kinetic energy of the electrons, and the Coulomb force which depends only on the distance between the electrons. Neither of these terms are spin dependant., thus the Hubbard Hamiltonian is invariant under the simultaneous rotation of all

the spins. As this is evident for the band term, we may be worried about the interaction term because it contains $n_\uparrow$ and $n_\downarrow$. We can rewrite $n_{l\uparrow}n_{l\downarrow}$ as follows:

$$n_{l\uparrow}n_{l\downarrow} = n_{l\uparrow} - S_l^+ S_l^- \,. \tag{A.5}$$

similarly

$$n_{l\uparrow}n_{l\downarrow} = n_{l\downarrow} - S_l^- S_l^+ \,. \tag{A.6}$$

Using the fact that $n_{l\sigma}^2 = n_{l\sigma}$, and the square of S_l^z, we obtain

$$n_{l\uparrow}n_{l\downarrow} = \frac{n_l}{2} - 2(S_l^z)^2 \,, \tag{A.7}$$

where $n_l = n_{l\uparrow} + n_{l\downarrow}$. Finally, we arrive at

$$n_{l\uparrow}n_{l\downarrow} = \frac{n_l}{2} - \frac{2}{3}\boldsymbol{S}_l^2 \,. \tag{A.8}$$

Hence the interacting term can be expressed as

$$\mathcal{H}_U = \frac{UN}{2} - \frac{2U}{3}\sum_l \boldsymbol{S}_l^2 \,. \tag{A.9}$$

This form makes the spin-rotational invariance apparent. The spin operators $\boldsymbol{S}_l$ are the SU(2) generators of rotations and given by

$$\boldsymbol{S}^+ = \sum_{j=1}^{L} c_{j\uparrow}^+ c_{j\downarrow} \qquad \boldsymbol{S}^- = \sum_{j=1}^{L} c_{j\downarrow}^+ c_{j\uparrow} \qquad S^z = \frac{1}{2}\sum_{j=1}^{L}(n_{j\uparrow} - n_{j\downarrow}) \,. \tag{A.10}$$

The decomposition of the interacting part makes it possible to search for magnetism ($\langle \boldsymbol{S}_l \rangle \neq 0$) in the Hubbard model.

A.1.2. Translational invariance

When cyclic boundary conditions are assumed, one can further reduce the size of the Hamiltonian matrix blocks specifying the eigenstates of $\mathcal{H}$ in terms of the eigenvalues of the translational operator T. The translational invariance symmetry expresses itself through the commutation of $\mathcal{H}$ with T, which can be defined as

$$T \mid n_1 n_2 \ldots n_{L-1} n_L \rangle = \mid n_2 n_3 \ldots n_L n_1 \rangle \,, \tag{A.11}$$

where

$$T \mid n_1 n_2 \dots n_{L-1} n_L\rangle = \mid n_1\rangle \otimes \mid n_2\rangle \otimes, \dots, \otimes \mid n_{L-1}\rangle \otimes \mid n_L\rangle\,, \tag{A.12}$$

and n_i is the state at site i. For each site i the four states $\mid 0\rangle_i, |\uparrow\rangle_i, |\downarrow\rangle_i$, and $|\uparrow\downarrow\rangle_i$ form a basis of the local Hilbert space. We can classify the states of the Hilbert space giving the occupation of each site, so that 2 denotes a doubly-occupied 1, a singly-occupied, and 0, an unoccupied i site. The doubly-occupied and the empty site states are eigenstates of $\boldsymbol{S}^2$ and S^z with zero eigenvalue. Let us consider The Hubbard model on a five-site ring. At $\rho = 0.4$, for two different spins, the possible configurations are

$$\text{(a)} \quad \mid 2\rangle_i \mid 0\rangle_j \mid 0\rangle_k \mid 0\rangle_l \mid 0\rangle_m\,, \quad \text{(b)} \quad \mid 1\rangle_i \mid 1\rangle_j \mid 0\rangle_k \mid 0\rangle_l \mid 0\rangle_m\,, \tag{A.13}$$

where the subscript denotes the lattice site ($i, j, k, l, m = 1, 2, 3, 4, 5$). The dimension of total Hilbert space of our small chain is 4^5. In case (a) we have $\boldsymbol{S}^2 \mid\uparrow\downarrow\rangle_i \mid 0\rangle_j \mid 0\rangle_k \mid 0\rangle_l \mid 0\rangle_m = 0$ for any i, j, k, l, m. In case (b) adding two spins $\frac{1}{2}$ we trivially obtain a triplet and a spin singlet state. Permutating the lattice indices we can write down all the eigenstates of $\boldsymbol{S}^2$ and S^z for these configurations.

The eigenvalues of T are $U = e^{i\frac{2\pi}{L}k}, k = 0, 1, 2, \dots, L-1$, which we will label by the number k. An eigenstate $\mid n, k\rangle$ of T with eigenvalue k is given by

$$\mid n, k\rangle = \frac{1}{\mathcal{N}_{n,k}}\left[1 + U + U^2 + \ldots + U^{L-1}\right] \mid n_1 n_2 \dots n_{L-1} n_L\rangle\,, \tag{A.14}$$

where $\mathcal{N}_{n,k}$ is a normalization constant. S, S^z, N, and k are simultaneous good quantum numbers. We divide the Hilbert space in sectors labeled by the quantum numbers $\left[N, S^z, k, d\right]$, where d is the dimension of the sector, and write down the states for some illustrative cases.

- $\left[2, 0, 0, 5\right]$

$$\begin{aligned}
\phi^{(1)}_{\left[2,0,0,5\right]} &= \frac{1}{\sqrt{5}}(\mid 000\uparrow\downarrow\rangle + \mid 00\uparrow\downarrow 0\rangle + \mid 0\uparrow\downarrow 00\rangle + \mid\uparrow\downarrow 000\rangle + \mid\downarrow 000\uparrow\rangle)\\
\phi^{(2)}_{\left[2,0,0,5\right]} &= \frac{1}{\sqrt{5}}(\mid 000\downarrow\uparrow\rangle + \mid 00\downarrow\uparrow 0\rangle + \mid 0\downarrow\uparrow 00\rangle + \mid\downarrow\uparrow 000\rangle + \mid\uparrow 000\downarrow\rangle)\\
\phi^{(3)}_{\left[2,0,0,5\right]} &= \frac{1}{\sqrt{5}}(\mid 00\uparrow 0\downarrow\rangle + \mid 0\uparrow 0\downarrow 0\rangle + \mid\uparrow 0\downarrow 00\rangle + \mid 0\downarrow 00\uparrow\rangle + \mid\downarrow 00\uparrow 0\rangle)\\
\phi^{(4)}_{\left[2,0,0,5\right]} &= \frac{1}{\sqrt{5}}(\mid 00\downarrow 0\uparrow\rangle + \mid 0\downarrow 0\uparrow 0\rangle + \mid\downarrow 0\uparrow 00\rangle + \mid 0\uparrow 00\downarrow\rangle + \mid\uparrow 00\downarrow 0\rangle)\\
\phi^{(5)}_{\left[2,0,0,5\right]} &= \frac{1}{\sqrt{5}}(\mid 00002\rangle + \mid 00020\rangle + \mid 00200\rangle + \mid 02000\rangle + \mid 20000\rangle)
\end{aligned}$$

- $\left[2,0,1,5\right]$

$$\begin{aligned}
\phi^{(1)}_{\left[2,0,1,5\right]} &= \frac{1}{\mathcal{N}_{\phi^{(1)}}}(\mid 000\uparrow\downarrow\rangle + e^{i2\pi/5} \mid 00\uparrow\downarrow 0\rangle + e^{i4\pi/5} \mid 0\uparrow\downarrow 00\rangle + e^{i6\pi/5} \mid\uparrow\downarrow 000\rangle \\
&\quad + e^{i8\pi/5} \mid\downarrow 000\uparrow\rangle) \\
\phi^{(2)}_{\left[2,0,1,5\right]} &= \frac{1}{\mathcal{N}_{\phi^{(2)}}}(\mid 000\downarrow\uparrow\rangle + e^{i2\pi/5} \mid 00\downarrow\uparrow 0\rangle + e^{i4\pi/5} \mid 0\downarrow\uparrow 00\rangle + e^{i6\pi/5} \mid\downarrow\uparrow 000\rangle \\
&\quad + e^{i8\pi/5} \mid\uparrow 000\downarrow\rangle) \\
\phi^{(3)}_{\left[2,0,1,5\right]} &= \frac{1}{\mathcal{N}_{\phi^{(3)}}}(\mid 00\uparrow 0\downarrow\rangle + e^{i2\pi/5} \mid 0\uparrow 0\downarrow 0\rangle + e^{i4\pi/5} \mid\uparrow 0\downarrow 00\rangle + e^{i6\pi/5} \mid 0\downarrow 00\uparrow\rangle \\
&\quad + e^{i8\pi/5} \mid\downarrow 00\uparrow 0\rangle) \\
\phi^{(4)}_{\left[2,0,1,5\right]} &= \frac{1}{\mathcal{N}_{\phi^{(4)}}}(\mid 00\downarrow 0\uparrow\rangle + e^{i2\pi/5} \mid 0\downarrow 0\uparrow 0\rangle + e^{i4\pi/5} \mid\downarrow 0\uparrow 00\rangle + e^{i6\pi/5} \mid 0\uparrow 00\downarrow\rangle \\
&\quad + e^{i8\pi/5} \mid\uparrow 00\downarrow 0\rangle) \\
\phi^{(5)}_{\left[2,0,1,5\right]} &= \frac{1}{\mathcal{N}_{\phi^{(5)}}}(\mid 00002\rangle + e^{i2\pi/5} \mid 00020\rangle + e^{i4\pi/5} \mid 00200\rangle + e^{i6\pi/5} \mid 02000\rangle \\
&\quad + e^{i8\pi/5} \mid 20000\rangle)
\end{aligned}$$

The same procedure can be applied for $k = 2, 3, 5$.

- $\left[2,1,0,2\right]$

$$\begin{aligned}
\phi^{(1)}_{\left[2,1,0,2\right]} &= \frac{1}{\sqrt{5}}(\mid 000\uparrow\uparrow\rangle + \mid 00\uparrow\uparrow 0\rangle + \mid 0\uparrow\uparrow 00\rangle + \mid\uparrow\uparrow 000\rangle + \mid\uparrow 000\uparrow\rangle) \\
\phi^{(2)}_{\left[2,1,0,2\right]} &= \frac{1}{\sqrt{5}}(\mid 00\uparrow 0\uparrow\rangle + \mid 0\uparrow 0\uparrow 0\rangle + \mid\uparrow 0\uparrow 00\rangle + \mid 0\uparrow 00\uparrow\rangle + \mid\uparrow 00\uparrow 0\rangle)
\end{aligned}$$

- $\left[2,1,1,2\right]$

$$\begin{aligned}
\phi^{(1)}_{\left[2,1,1,2\right]} &= \frac{1}{\mathcal{N}_{\phi^{(1)}}}(\mid 000\uparrow\uparrow\rangle + e^{i2\pi/5} \mid 00\uparrow\uparrow 0\rangle + e^{i4\pi/5} \mid 0\uparrow\uparrow 00\rangle + e^{i6\pi/5} \mid\uparrow\uparrow 000\rangle \\
&\quad + e^{i8\pi/5} \mid\uparrow 000\uparrow\rangle) \\
\phi^{(2)}_{\left[2,1,1,2\right]} &= \frac{1}{\mathcal{N}_{\phi^{(2)}}}(\mid 00\uparrow 0\uparrow\rangle + e^{i2\pi/5} \mid 0\uparrow 0\uparrow 0\rangle + e^{i4\pi/5} \mid\uparrow 0\uparrow 00\rangle + e^{i6\pi/5} \mid 0\uparrow 00\uparrow\rangle \\
&\quad + e^{i8\pi/5} \mid\uparrow 00\uparrow 0\rangle)
\end{aligned}$$

The above example gives an idea of how helpful symmetry implementation can be. Indeed, a further reduction in the Hilbert space can be achieved in some cases by considering a lattice symmetry, namely $[W, \mathcal{H}] = 0$, where

$$W = \mid n_1 n_2 \dots n_{L-1} n_L\rangle = \mid n_L n_{L-1} \dots n_2 n_1\rangle\,. \tag{A.15}$$

The eigenvalues of W are $+1$ and -1. For instance, the sector $\left[2,0,0,5\right]$ can be broken into

two subspaces, indexed by $W = -1(\big[2,0,0,-1,2\big])$ and $W = +1(\big[2,0,0,1,3\big])$, and given by:

- $\big[2,0,0,-1,2\big]$

$$\phi^{(1)}_{\big[2,0,0,-1,2\big]} = \frac{1}{\sqrt{2}}(\phi^{(1)}_{\big[2,0,0,5\big]} - \phi^{(2)}_{\big[2,0,0,5\big]})$$
$$\phi^{(2)}_{\big[2,0,0,-1,2\big]} = \frac{1}{\sqrt{2}}(\phi^{(2)}_{\big[2,0,0,5\big]} - \phi^{(3)}_{\big[2,0,0,5\big]})$$

- $\big[2,0,0,1,3\big]$

$$\phi^{(1)}_{\big[2,0,0,1,3\big]} = \frac{1}{\sqrt{2}}(\phi^{(1)}_{\big[2,0,0,5\big]} + \phi^{(2)}_{\big[2,0,0,5\big]})$$
$$\phi^{(2)}_{\big[2,0,0,1,3\big]} = \frac{1}{\sqrt{2}}(\phi^{(2)}_{\big[2,0,0,5\big]} + \phi^{(3)}_{\big[2,0,0,5\big]})$$
$$\phi^{(3)}_{\big[2,0,0,1,3\big]} = \phi^{(5)}_{\big[2,0,1,5\big]}\,.$$

If most symmetries discussed above are implemented, then we can significantly reduce the computational effort required for diagonalizing the Hamiltonian.

B. Implementation of ED and Lanczos algorithm

This appendix gives a brief sketch on how to implement ED for a 1d Hubbard model.

B.1. Coding the basis states

The first step is to construct a basis set. A general Fock state is given by applying creation operators to this state

$$|n_{1\uparrow},\ldots,n_{L\downarrow}\rangle = \left(C^{\dagger}_{1\uparrow}\right)^{n_{1\uparrow}}\left(C^{\dagger}_{1\downarrow}\right)^{n_{1\downarrow}}\cdots\left(C^{\dagger}_{L\uparrow}\right)^{n_{L\uparrow}}\left(C^{\dagger}_{L\downarrow}\right)^{n_{L\downarrow}}|0\rangle, \tag{B.1}$$

$|0\rangle$ is the vacuum state. $n_{i\sigma}$ is the occupation number ($= 0$ or 1) of electrons spin σ at the site $i(i = 1,\ldots,L)$.
The order in which the creation operators are applied is a matter of convention, but should be fixed for the entire calculation.
In order to minimize the computer memory, these configurations are maped onto computer words which are sets of bits also either 0 or 1. A 1 bit is "set" and a 0 bit "unset". Thus these configurations are stored in binary form. Each spin configuration is represented by a 32 bit unsigned integer word and identifies by either $I^{\uparrow}$ or $I^{\downarrow}$. These integers are written as

$$I^{\uparrow} = \sum_{1}^{L} 2^{2i-2}\sigma_i, \qquad I^{\downarrow} = \sum_{1}^{L} 2^{2i-1}\sigma_i \tag{B.2}$$

A configuration of different spins then is represented by an integer $n = I^{\uparrow} + I^{\downarrow}$.
Thus, for a linear system of 4 particles would be represented as

$$n(|\uparrow\downarrow\uparrow\downarrow\rangle \equiv 01100110) = 102 \tag{B.3}$$

There are 2^{2L} states, but not all are relevant due to the symmetries of the Hamiltonian of the Hubbard model which is a block-diagonal. The ED is to be performed in a sector of the total Hilbert space with fixed values, i.e. the dimension of the relevant sector, is

$$dim = \left(\frac{L!}{N_{\uparrow}!\,(L-N_{\uparrow})!}\right)\left(\frac{L!}{N_{\downarrow}!\,(L-N_{\downarrow})!}\right) \tag{B.4}$$

Following a set of general bit manipulations, regardless of the type of the Hamiltonian used. Here for convenience I considered a simple Hubbard form

$$\mathcal{H} = -t\sum_{<ij>,\sigma}\left(c^{\dagger}_{i\sigma}c_{j\sigma} + H.c.\right) + U\sum_{i} n_{i\uparrow}n_{i\downarrow}\,. \tag{B.5}$$

The hopping term is easily implemented by logical operations. To be more specific a subroutine representing a creation operator $c^{\dagger}_{j\sigma}$ for a fermion would set the corresponding bit in the

appropriate word,i.e. takes as arguments the specific location together with its spin σ, $2j-2$ for $\sigma =\uparrow$, and $2j-1$ for $\sigma =\downarrow$, and the Fock state labeled as above by n. It should return zero unless bit j with its corresponding σ is not set in $n\,(|n_{1\uparrow}n_{1\downarrow},\ldots,n_{L\uparrow}n_{L\downarrow}\rangle)$. A simple test for this is, for instance for $\sigma =\uparrow$, whether, the bitwise logical operation $n\&(1<<2j-1)$ is zero or not. $\wedge$ is the bitwise exclusive-or operator, which operates bit by bit. If one bit is zero and one bit is one, the result is true (1). An exclusive-or can be used to determine at which bits two bit vectors differ. The left shift operator, $<<$, shifts all bits some number of times toward the left.. The resulting Fock state is represented by $n\wedge(1<<2j-1)$
When $n\&(1<<2j-1)$ is zero, the function returns the corresponding sign obtained after the creation operator flips the bit. The hopping process can result in a negative sign due to the fermi statistics of the electrons.
Simple bit counting technique allows to track this. The sign returned is associated with bringing the operator $c^{\dagger}_{j\uparrow}$ into the ordering convention above. This can be quickly found by logical operations, beginning with a masking off of the lower bits by considering the integer $n\&(1-(1<<2j-1))$. We need to include a negative sign if the population count of this integer is odd. The population count of an integer is the number of set bits it contains. The following is a simple way to implement such a count.

- COUNTING BITS

```
inline int bitcount (int i) {
/* counts the set bits in a word */
int result = 0;
while (i) {
result++;
/* finds abd resets rightmost set bits*/
i & = (i −1);
}
return result;
}
```

For the annihilation operator which resets a bit, one does exactly the same thing except checking that the initial bit is set. To apply some combination of creation and annihilation operators to a given Fock state $|n\rangle$ involves a succession of the above subroutines. The interaction term is also easily implemented by looping over all sites and count doubly occupied sites. The later is the population count of $n_{j\uparrow}\&n_{j\downarrow}$. If $n_{\uparrow}\&n_{\downarrow}=1$, this means that both bits $2j-2$ and $2j-1$ are set to 1. Thus, we have a doubly-occupied site.

The density $\rho=\frac{N_{\uparrow}+N_{\downarrow}}{L}$ is fixed in a given calculation.
Since the number of states is less than 2^{2L}, one needs a lookup table that gives the index of a given state from its binary representation $(n_{1\uparrow}\ldots n_{L\downarrow})$. This table can be deleted as soon as the hamiltonian matrix has been built, before allocating the Lanczos vectors. If the Fock states are ordered, one can instead use a binary search. This is the method used here, where for each subspace an array of integers $(I^{\uparrow},I^{\downarrow})$. By having this array, a given state can be quickly located. Then the corresponding location gives the desired index of the state.

B.2. Reducing Hilbert space using symmetries

We wish to find eigenvalues and eigenvectors of the Hamiltonian (A.1) on large clusters. In order to achieve this, and taken into account that computational power is limited, it is necessary to use the symmetries of the problem to reduce the size of the corresponding Hilbert space. For $L = 20$ sites we use:

1. translational symmetry (L operations for an L-site cluster).

2. if the z-component S_z of the total magnetization (which commutes with the Hamiltonuan) is zero, then the spin inversion operation $|\uparrow\rangle \leftrightarrow |\downarrow\rangle$ is also a symmetry and leads to a further reduction by a factor 2.

- Momentum eigenbasis

  Using periodic boundary conditions, we can reduce the total number of basis states using the L lattice translations. Since the lattice translations commute with $\mathcal{H}$, we can break up the original Hilbert space into L subspaces, each with momentum k, where k is any reciprocal lattice in the first Brillouin zone:

$$k = \left(\frac{2\pi n}{L}\right) \text{with} \quad 0 \leq n < L \tag{B.6}$$

  We construct Bloch states using the $|n\rangle's$:

$$|n,k\rangle = \frac{1}{N_{n,k}} \sum_{l=0}^{L-1} e^{-ikl} T_l |n\rangle, \tag{B.7}$$

  where $N_{n,k}$ is a normalisation constant.
  When calculating the translated states $|n,k\rangle$, we have to take into account the Fermi signs which are introduced by the reordering of the state's particle creating operators due to translation and periodic boundary conditions which destroy the convention order above. To illustrate this consider the 1D translational operator through l lattice spacings, $T_l(k) \equiv e^{ikl} \prod_{\sigma=\pm} \prod_{iocc}^{n_\sigma} c^\dagger_{iocc+l,\sigma} c_{iocc,\sigma}$, on the state $c^\dagger_{2\uparrow} c^\dagger_{3\downarrow}|0\rangle = |0 \downarrow\uparrow 0\rangle$ in a 4-sites chain. The product runs over all n_σ occupied sites. For momentum $k = 0$ and translation by one lattice spacing $l = 1$, we have $T_1(k=0)|0 \downarrow\uparrow 0\rangle = c^\dagger_{3\uparrow} c_{2\uparrow} c^\dagger_{4\downarrow} c_{3\downarrow} c^\dagger_{2\uparrow} c^\dagger_{3\downarrow}|0\rangle = +c^\dagger_{3\uparrow} c^\dagger_{4\downarrow}|0\rangle = +|\downarrow\uparrow 00\rangle$. Thus, a translation without a jump across the boundary causes a plus sign, while $T_1(k=0)|\downarrow\uparrow 00\rangle = c^\dagger_{4\uparrow} c_{3\uparrow} c^\dagger_{1\downarrow} c_{4\downarrow} c^\dagger_{3\uparrow} c^\dagger_{4\downarrow}|0\rangle = +c^\dagger_{3\uparrow} c^\dagger_{4\downarrow}|0\rangle = -|\uparrow 00\downarrow\rangle$. The $k = 0$ state for the above example would thus be $\frac{1}{2}[+|\downarrow\uparrow 00\rangle - |\uparrow 00\downarrow\rangle + |00\downarrow\uparrow\rangle + |0\downarrow\uparrow 0\rangle]$.
  If we restrict ourself to a subspace with a particular k, the number of distinct Bloch states is about $1/L$ of the original number of basis states, but this is not the case for k-states with higher symmetries, resulting in the fact that the application of $T_l|n\rangle$ lead to less than L distinct states. In this case the appropriate normalisation factor is then given by $\frac{1}{\sqrt{\frac{L}{l}}}$, l is an integer.

The set of distinct Bloch states is used now as a new basis. In order to find the lowest energy state, we have to repeat the procedure in other subspaces with different k. Fortunately, due to the symmetry of the Brillouin zone, many of the $k^{'}$s are degenerated and we need to repeat the iterations for the nondegenerated $k^{'}$s only.

Coding the k-states is more complicated. Each basis state is not a single configuration represented by an integer word n described above. We generate L configurations by L translations but only the one with the smallest integer value should be stored as the "representative" $|r\rangle$ of the basis state $|n,k\rangle$. We throw away all other configurations which are not representatives. Additionally, the normalization factor and the signs which result from the L translations should also be stored. Now, given a representative configuration $|r\rangle$, we can generate every term in Eq. $(A.6)$. Conversely, given any spin configuration $|n\rangle$, we can find the representative $|r\rangle$ of the basis state to which it belongs by finding the smallest of $T_l|n\rangle$. This is important in calculating the matrix elements as we shall see next.

- Matrix multiplication
  We turn now to the implementation of the matrix multiplication

$$|\psi_m\rangle = \mathcal{H}|\psi_n\rangle \tag{B.8}$$

which is always specific to the model Hamiltonian $\mathcal{H}$ and form the central part of the Lanczos code. The Hamiltonian matrix has to be computed in the basis state $|n,k\rangle$. Thus it is only necessary to apply $\mathcal{H}$ on the set of representatives $|r\rangle$. Once this is done, the matrix is used in a Lanczos algorithm to obtain eigenvalues and eigenvectors of the Hamiltonian. The main difficulty is that the application of $\mathcal{H}$ on a representative $|r\rangle$ will not in general produce another representative $|\bar{r}\rangle$, but rather a state that needs to be brought into minimal form (representative) by application of a symmetry operation. An approach is to use the set of all configurations arranged in increasing order (in their integer representation) as a sorted table. One can then use a binary search to locate a given configuration in the table. For the Hubbard model, when it is applied on $|r\rangle$, the on-site Coulomb repulsion term is diagonal in the chosen basis. It does not change the spin configurations. Whereis the hopping term $c^{\dagger}_{i\sigma}c_{j\sigma}$ in $\mathcal{H}$ hops a spin σ from site j to site i, resulting in another spin configuration $|m\rangle$ from $|r\rangle$ with an additional sign s_{ij}. Then we have to identify the representative $|\bar{r}\rangle$ of the state $|m,k\rangle$ to which $|m\rangle$ belongs. The matrix element of the hopping term is given by

$$\langle m,k|\mathcal{H}_{hop}|n,k\rangle = \left(\frac{\mathcal{N}_{m,k}}{\mathcal{N}_{n,k}}\right) s_{ij}\sigma_l e^{ik.R_l}, \tag{B.9}$$

where $\sigma_l e^{ik.R_l}$ is the phase factor of $|\bar{r}\rangle$ in $|m,k\rangle$.

- Lanczos algorithm

The Lanczos algorithm is one of the algorithms to diagonalize a Hermitian matrix by first transforming it to a tridiagonal matrix. The advantage of this algorithm is that the original

matrix is not changed during the Lanczos iteration. In particular, if the original matrix is sparse, which is the case of an overdoped Hubbard Hamiltonian, it can be stored as a sparse matrix. This feature is very attractive when the size of the matrix is large. In addition, a good estimate of the lowest eigenstate can be obtained using the Lanczos algorithm well before the tridiagonalization process is completed. Therefore, the Lanczos algorithm is preferred over other algorithms for systems with large Hamiltonian matrices.
Given a Hermitian matrix $\mathcal{H}$, after M iterations, the Lanczos algorithm generates an $M \times M$ real tridiagonal matrix

$$T_M = \begin{pmatrix} a_0 & b_1 & 0 & 0 & . & . \\ b_1 & a_1 & b_2 & 0 & . & . \\ 0 & b_2 & a_2 & b_3 & . & . \\ 0 & 0 & b_3 & a_3 & . & . \\ . & . & . & . & & \\ . & . & . & . & & \end{pmatrix} \tag{B.10}$$

by the following steps:
LANCZOS ALGORITHM
$\alpha =$ normalized initial state, $\beta = \mathcal{H}\alpha$,
$a_0 = \alpha * \beta, \beta = \beta - a_0\alpha, b_1 =\parallel \beta \parallel$,
for $j = 2, \ldots, M$
$\gamma = \alpha, \alpha = \beta/b_{j-1}, \beta = -b_{j-1}\gamma$,
$\beta = \beta + \mathcal{H}\alpha$,
$a_j = \alpha * \beta, \beta = \beta - a_j\alpha, b_j =\parallel \beta \parallel$,
end
Let e_M be the algebraically smallest eigenvalue of T_M and x_M the corresponding eigenvector. For large enough M, e_M is an approximation for the smallest eigenvalue of $\mathcal{H}$. We increase M step by step until e_M converges. An approximation to the lowest eigenstate of $\mathcal{H}$ can be obtained by

$$X_M = \sum_{i=1}^{M} x_M \alpha_i, \tag{B.11}$$

where α_i are the vectors α during each iteration. The Lanczos algorithm can also be used to find the few lowest eigenstates, but here we will concentrate on the lowest eigenstate only.

C. The strong coupling limit of the Hubbard model

In this appendix we study the large U perturbation theory of the Hamiltonian following the standard method described in many textbooks [70, 71, 72]. We rewrite the Hubbard model as

$$\mathcal{H} = T + UD\,, \tag{C.1}$$

where

$$T = \sum_{j,k=1,\sigma}^{L} t_{jk} c_{j\sigma}^{\dagger} c_{k\sigma}\,, \qquad D = U \sum_{j}^{L} n_{j\uparrow} n_{j\downarrow}\,. \tag{C.2}$$

We shall assume that $t_{jj} = 0, t_{jk} = t_{kj}^{*}$ and $U > 0$.
T can be considered as perturbation if $|t_{jk}| \ll U$ for $j,k = 1,\ldots,L$. The operator D is diagonal in the Wannier basis, as we have seen in Chap. 2. It counts the number of doubly occupied states. Its eigenvalues are $n = 0, 1, \ldots, L$. Let us denote the projectors onto the corresponding eigenspaces $\mathcal{H}_n$ by P_n. Therefore the Hilbert space $\mathbf{H}$ of model $(C.1)$ decomposes into $\mathbf{H}^{(L)} = \mathbf{H}_0 \oplus \ldots \oplus \mathbf{H}_L$, and D has the spectral decomposition

$$D = \sum_{n=1}^{L} n P_n\,. \tag{C.3}$$

The Hamiltonian $(C.1)$ conserves the number of electron N as we have seen in Appendix B. In the following we will be interested in the case when $N \leq L$. In the case $N < L$ the singly occupied sites can be picked out in C_N^L ways, and each of these sites can harbour either an $\uparrow$-or a $\downarrow$-spin, so the degeneracy is $C_N^L 2^N$-fold. At half-filling $(N = L)$ we find only the spin degeneracy 2^L. The space of N-particle eigenstates has non-zero overlap with the eigenspace $\mathcal{H}_0$ of P_0, which is spanned by $C_N^L 2^N$ degenerate ground states of D. Hence, the total number of Wannier states with no site doubly occupied is

$$\mathcal{H}_0 = 3^L\,. \tag{C.4}$$

The perturbation T will partially lift this large degeneracy. The lowest energy level of UD will split into many levels which are expected to be well separated from the first excited level of UD as long as the condition $|t_{jk}| \ll U$ holds. The description of the splitting of the ground state will be by means of an effective Hamiltonian, called $t - J$ Hamiltonian. At half-filling it turns into the Hamiltonian of the isotropic spin-1/2 Heisenberg chain.

C.1. Projectors

An operator P_n which is characterized by the relations

$$P_n^2 = P_n, \qquad P_n^\dagger = P_n \tag{C.5}$$

is called a self-adjoint projection operator. One observes that $Q = 1 - P_n$ also satisfies the relations $Q^2 = Q, Q^\dagger = Q$.

A fermionic representation of the projector P_n is obtained from the following generating function

$$G(\alpha) = \prod_{j=1}^{L} (1 - \alpha\, n_{j,\uparrow} n_{j,\downarrow}) \; . \tag{C.6}$$

Let us consider the action of $G(\alpha)$ on the Wannier states $|x, a\rangle$

$$n_{j,\uparrow} n_{j,\downarrow} |x, a\rangle = \sum_{1 \le k < l \le N} \delta_{j,x_k} \delta_{j,x_l} |x, a\rangle = \begin{cases} |x, a\rangle & \text{if site } j \text{ is doubly occupied}\,, \\ 0 & \text{else}\,. \end{cases} \tag{C.7}$$

Thus

$$G(\alpha)|x, a\rangle = (1 - \alpha)^n \, |x, a\rangle \,, \tag{C.8}$$

where n is the number of doubly occupied sites in the state $|x, a\rangle$, i.e., $D|x, a\rangle = n|x, a\rangle$. From the above equation, we have

$$\frac{(-1)^k}{k!} \partial_\alpha^k G(\alpha)|_{\alpha=1} |x, a\rangle = \delta_{kn} |x, a\rangle \tag{C.9}$$

and hence,

$$P_n = \frac{(-1)^n}{n!} \partial_\alpha^n G(\alpha)|_{\alpha=1} \,. \tag{C.10}$$

The above equation extends to $n = 0$, and Eq (*C*.8) implies $P_0 = G(1)$.

C.2. Second order perturbation theory for degenerate systems

First we give a summary of the perturbation theory. Assume that the Hamiltonian, acting on a Hilbert space $\mathbf{H}$, is

$$\mathcal{H} = \mathcal{H}_0 + \lambda V \tag{C.11}$$

and $\mathcal{H}_0$ has a discrete m-fold degenerate level E

$$\mathcal{H}_0 = \sum_n E_n \, P_n \tag{C.12}$$

and a perturbation V coupled to $\mathcal{H}_0$ by a coupling constant λ.

$|\psi\rangle$ is a solution of the Schrödinger equation

$$\mathcal{H}|\psi\rangle = E|\psi\rangle \tag{C.13}$$

with eigenvalue E, if and only if

$$\begin{aligned} P_n\mathcal{H}P_n|\psi\rangle + P_n\mathcal{H}Q|\psi\rangle &= EP_n|\psi\rangle \,, \\ Q_n\mathcal{H}P_n|\psi\rangle + Q_n\mathcal{H}Q|\psi\rangle &= EQ_n|\psi\rangle \,. \end{aligned} \tag{C.14}$$

A solution of Eq. (C.14) gives

$$\mathsf{H}_n(E)|\phi\rangle = E|\phi\rangle \,, \tag{C.15}$$

where

$$\mathsf{H}_n(E) = P_n\mathcal{H}(1 + (E - Q_n\mathcal{H})^{-1}Q_n\mathcal{H})P_n \tag{C.16}$$

and $|\phi\rangle = P|\psi\rangle$. Hence, $|\phi\rangle \in P_n\mathcal{H}$, where $P_n\mathcal{H}$ is a subspace of $\mathbf{H}$, is a solution of the spectral problem Eq. (C.13), whereas the vector

$$|\psi\rangle = (1 + (E - Q_n\mathcal{H})^{-1}Q_n\mathcal{H})|\phi\rangle \tag{C.17}$$

is a solution of the full stationary Schrödinger Eq. (C.13) with eigenvalue E.

The following elementary relations

$$\begin{aligned} &P_mP_n = \delta_{mn}P_n \,, \\ &P_n\mathcal{H}_0 = \mathcal{H}_0\,P_n = E_nP_n \,, \quad Q_n\mathcal{H}_0 = \mathcal{H}_0\,Q_n = E_nQ_n \sum_{m(m\neq n)} E_mQ_m \,, \\ &P_n\mathcal{H}Q_n = \lambda P_n\mathcal{H}_1Q_n \quad Q_n\mathcal{H}P_n = \lambda Q_n\mathcal{H}_1P_n \end{aligned} \tag{C.18}$$

are useful to obtain a reformulation of the original spectral problem Eq. (C.15) to

$$P_n \mathcal{H}_1 \sum_{k=0}^{\infty} \lambda^{k+1} \left(\sum_{m(m\neq n)} \frac{P_m \mathcal{H}_1}{E - E_m} \right)^k |\phi\rangle = (E - E_n)|\phi\rangle \tag{C.19}$$

for $|\phi\rangle \in P_n\mathcal{H}$.
The Eq. (C.18) is an iterative equation in ascending orders of λ. For $\lambda = 0$, we have $E = E_n$. For small λ, Eq. (C.18) leads to corrections to E_n of the form

$$E = E_n + \lambda E_n^{(1)} + \lambda^2 E_n^{(2)} + O(\lambda^3). \tag{C.20}$$

A short calculation gives an effective Hamiltonian on the restricted Hilbert space $P_n\mathcal{H}$

$$\left[P_n \mathcal{H}_1 P_n + \sum_{m(m\neq n)} \frac{P_n \mathcal{H}_1 P_m \mathcal{H}_1 P_n}{E_n - E_m} \right] |\phi\rangle = \frac{E - E_n}{\lambda} |\phi\rangle \,. \tag{C.21}$$

This Hamiltonian describes the splitting of the energy level E_n of the Hamiltonian $\mathcal{H}_0$ under the influence of the small perturbation $\lambda\mathcal{H}_1$.

C.3. The Hubbard model in the strong coupling limit

Let us here apply the procedure described in the previous section to the hubbard model (C.1). To have a similar form of the hamiltonian as in (C.11), we need to rescale it as

$$\mathcal{H}/U = D + T/U \,. \tag{C.22}$$

Consequently, the energy has to be rescaled as well. $\lambda = 1/U, \mathcal{H}_0 = P_0\mathbf{H} = D$, and $\mathcal{H}_1 = T$. The operator D has eigenvalues $E_n = n$, for $n = 0, 1, \ldots, L$. Setting $n = 0$ in (C.20) we obtain the t-J Hamiltonian

$$\left[P_0 \mathcal{H}_1 P_0 + \frac{1}{U} \sum_{m=1}^{L} \frac{P_0 T P_0 T P_0}{m} \right] |\phi\rangle = E|\phi\rangle \,. \tag{C.23}$$

t-J Hamiltonian describes the splitting of the lowest energy level $E_0 = 0$ of the Hubbard Hamiltonian in the atomic limit, when the hopping term is much small compared to the on site interaction U. The projection operator P_0 onto the space with no doubly occupied is

$$P_0 = \prod_{j=1}^{L} (1 - n_{j,\uparrow} n_{j,\downarrow}) \,. \tag{C.24}$$

The relation

$$n_{j,\uparrow}n_{j,\downarrow}P_0 = P_0 n_{j,\uparrow}n_{j,\downarrow} = 0 \tag{C.25}$$

for $j = 0, 1, \ldots, L$, which implies that

$$G(\alpha) = \sum_{j,k=1}^{L} t_{jk}(1 - \alpha\, n_{j,\uparrow}n_{j,\downarrow})c^{\dagger}_{j,\sigma}c_{k,\sigma}P_0\,. \tag{C.26}$$

And by application of $(C.10)$, it follows that

$$\sum_{m=1}^{L}\frac{P_m T P_0}{m} = \sum_{j,k=1}^{L} t_{jk}n_{j,\uparrow}n_{j,\downarrow}c^{\dagger}_{j,\sigma}c_{k,\sigma}P_0\,, \tag{C.27}$$

and hence,

$$\mathcal{H}_{\text{t-J}} = P_0\left[\sum_{j,k=1}^{L} t_{jk}c^{\dagger}_{j,\sigma}c_{k,\sigma} - \frac{1}{U}\sum_{j,k,k',l=1}^{L} t_{jk}t_{k'l}c^{\dagger}_{j,\sigma}c_{k,\sigma}n_{k',\uparrow}n_{k',\downarrow}c^{\dagger}_{k',\sigma'}c_{l,\sigma'}\right]P_0\,. \tag{C.28}$$

The above equation can be further simplified by considering the following: for $k' \neq j$, the term $n_{k',\uparrow}n_{k',\downarrow}$ can be commuted through $c^{\dagger}_{j,\sigma}c_{k,\sigma}$, and, by $(C.24)$, the corresponding terms in the second sum in $(C.27)$ vanish. The term with $k' = j$ also vanishes. For $j \neq k$ this follows from $c^{\dagger}_{j,\sigma}n_{j,\uparrow}n_{j,\downarrow} = 0$ and for $j = k$ from $c^{\dagger}_{j,\sigma}c_{j,\sigma}n_{j,\uparrow}n_{j,\downarrow} = 2n_{j,\uparrow}n_{j,\downarrow}$ and $(C.24)$. Thus, the only non-vanishing contribution in the sum over k' comes from the term $k' = k$, and the sum in $(C.27)$ reduces to a triple sum over j, k, and l. Finally, in the remaining triple sum, we may commute the term $n_{k',\uparrow}n_{k'}$ to the left and use once more $(C.24)$. The resulting expression for the t-J Hamiltonian is, using the operators

$$S^{\alpha}_{jk} = tr(\sigma^{\alpha}S_{jk}), \quad S^{0}_{jk} = tr(S_{jk})\,, \tag{C.29}$$

where $\sigma^{\alpha}, \alpha = x, y, z$ are the Pauli matrices, and $S^{b}_{jk_a} = c^{\dagger}_{j,a}c_{k,b}$,

$$\mathcal{H}_{\text{t-J}} = P_0\big[\sum_{\substack{j,k=1\\ j\neq k}}^{L} t_{jk}c^{\dagger}_{j,\sigma}c_{k,\sigma} + \sum_{\substack{j,k=1\\ j\neq k}}^{L}\frac{2|t_{jk}|^2}{U}\left(S^{\alpha}_{j}S^{\alpha}_{k} - \frac{n_j n_k}{4}\right) \tag{C.30}$$

$$+\frac{1}{U}\sum_{\substack{j,k,l=1\\ j\neq k\neq l\neq j}}^{L} t_{jk}t_{kl}\left(c^{\dagger}_{j,\sigma}\sigma^{\alpha}_{\sigma\sigma'}c_{l,\sigma'}S^{\alpha}_{k} - \frac{1}{2}c^{\dagger}_{j,\sigma}c_{l,\sigma}n_k\right)\big]P_0\,, \tag{C.31}$$

where $S^{\alpha}_{j} = \frac{1}{2}S^{\alpha}_{jj}$ are local spin operators. Another form is obtained for t-J model when we move the operator P_0

$$\begin{aligned}\mathcal{H}_{\text{t-J}} = &\sum_{\substack{j,k=1\\ j\neq k}}^{L} t_{jk} c^{\dagger}_{j,\sigma} c_{k,\sigma} (1-n_j) + \sum_{\substack{j,k=1\\ j\neq k}}^{L} \frac{2|t_{jk}|^2}{U} \left(S^{\alpha}_j S^{\alpha}_k - \frac{n_j n_k}{4} \right) \\ &+ \frac{1}{U} \sum_{\substack{j,k,l=1\\ j\neq k\neq l\neq j}}^{L} t_{jk} t_{kl} \left(c^{\dagger}_{j,\sigma} \sigma^{\alpha}_{\sigma\sigma'} c_{l,\sigma'} S^{\alpha}_k - \frac{1}{2} c^{\dagger}_{j,\sigma} c_{l,\sigma} n_k \right) (1-n_j) \,.\end{aligned} \tag{C.32}$$

The t-J Hamiltonian conserves the number of particles and the total spin,

$$\left[\mathcal{H}_{\text{t-J}}, \hat{N}\right] = \left[\mathcal{H}_{\text{t-J}}, S^{\alpha}\right] = 0 \quad \text{for} \alpha = x, y, z \,. \tag{C.33}$$

C.4. Half-Filled Band: The Heisenberg Model

At half-filling, the $\mathcal{H}_{\text{t-J}}$ acts on pure spin states of the form $|a_1, \ldots, a_L\rangle = c^{\dagger}_{L,\sigma_L}, \ldots, c^{\dagger}_{1,\sigma_1}|0\rangle$. In these states every lattice site is occupied precisely by one electron. Hence $(1-n_j)|a_1, \ldots, a_L\rangle = 0$, and the Hamiltonian ($C$.30) reduces to an effective Hamiltonian

$$\mathcal{H}_{\text{Spin}} = \sum_{\substack{j,k=1\\ j\neq k}}^{L} \frac{2|t_{jk}|^2}{U} \left(S^{\alpha}_j S^{\alpha}_k - \frac{1}{4} \right) \,. \tag{C.34}$$

This is the isotropic spin-$\frac{1}{2}$ Heisenberg chain with exchange $J_{jk} = 2|t_{jk}|^2 U$ between spins at sites j and k. For the special case of NN hopping $t_{jk} = -t(\delta_{j,k-1} + \delta_{j,k+1})$ the Hamiltonian (C.1) turns into the Hubbard Hamiltonian (2.10). The corresponding spin chain Hamiltonian (C.32) becomes

$$\mathcal{H}_{\text{Spin}} = \frac{2t^2}{U} \sum_{j=1}^{L} \left(S^{\alpha}_j S^{\alpha}_k - \frac{1}{4} \right) \,, \tag{C.35}$$

where periodic boundary conditions $S^{\alpha}_{L+1} = S^{\alpha}_1$ are implied. The sign of the exchange coupling is the same as the sign of the Hubbard interaction U. thus, at half-filling and for strong repulsion $U \gg |t|$ the low-lying excitations of the hubbard model are effectively described by the excitations of an antiferromagnetic Heisenberg chain.

The spin Hamiltonian (C.33) is exactly solvable by Bethe ansatz [73].

Bibliography

[1] J. Hubbard. *Phys. Rev. B.*, 17:494, 1978.

[2] J. Kondo and K. Yamai. *J. Phys. Soc. Japan.*, 43:424, 1977.

[3] E. Wigner. *Trans. Faraday.*, 34:678, 1938.

[4] J. Hubbard. *Proc. R. Soc. London Ser. A.*, 240:539, 1957.

[5] J. Hubbard. *Proc. R. Soc. London Ser. A.*, 243:244, 1958.

[6] J. Hubbard. *Proc. R. Soc. London Ser. A.*, 276:238, 1963.

[7] M C Gutzwiller. *Phys. Rev. Lett.*, 10:159, 1963.

[8] J. Kanamori. *Prog. Theor. Phys.*, 30:275, 1963.

[9] E.H. Lieb and F.Y. Wu. *Phys. Rev. Lett.*, 20:1445, 1968.

[10] L. Arachea and A. A. Aligia. *Phys. Rev. Lett.*, 73:2240, 1994.

[11] S. Capponi, D. Poiblanc, and T. Giamarchi. *Phys. Rev. B.*, 61:13410, 2000.

[12] Hitoshi Seo and Masao Ogata. *Phys. Rev. B.*, 64:113103, 2001.

[13] B. Valenzuela, S. Fratini, and D. Baeriswyl. *Phys. Rev. B.*, 68:045112, 2003.

[14] S. Nishimoto and Y. Ohta. *Phys. Rev. B.*, 68:235114, 2003.

[15] P. Horsch, M. Sofin, M. Mayr, and M. Jansen. *Phys. Rev. Lett.*, 94:076403, 2005.

[16] M. Mayr and P. Horsch. *Phys. Rev. B.*, 73:195103, 2006.

[17] J. Schnack and F. Ouchni. *J. Mag. Mag. Mat.*, 290-291:341, 2005.

[18] K.A Chao, J. Spalek, and A.M. Oles. *J. Phys. C.*, 10:L271, 1977.

[19] Yu.A. Izyumov, B.M. Letfulov, and E.V. Shipitsin. *J. Phys. Condens. Matter.*, 2:8905, 1990.

[20] J. Hubbard. *Proc. R. Soc. London Ser. A.*, 277:401, 1964.

[21] S. Ejima, F. H. L. Essler, and F. Gebhard. *J. Phys. A-Math. Gen.*, 39:4845.

[22] H.J. Schulz. *Phys. Rev. Lett.*, 64:2831, 1990.

[23] P. A. Lee, T. M. Rice, and R. A. Klemm. *Eur. Phys. B.*, 15:2984, 1977.

[24] V. J. Emery. *Phys. Rev. Lett.*, 37:107, 1976.

[25] F. Ouchni, J. Schnack, and J. Schulenburg. *submited to PRB*, 2006.

[26] E. M. MeCarron, M. A. Subramanian, J. C. Calabrese, and R. L. Harlow. *Mat. Res. Bull.*, 23:1355, 1988.

[27] T. Siegrist, L. F. Schneemeyer, S. A. Sunshineand J. V. Waszezak, and R. S. Roth. *Mat. Res. Bull.*, 23:1429, 1988.

[28] M. Uehara, T. Nagata, J. Akimitsu, H. Takahashi, N. Mori, and K. Kinoshita. *J. Phys. Soc. Jpn.*, 62:2764, 1996.

[29] Elbio Dagotto. *Phys. Rev. B.*, 45:5744, 1992.

[30] Elbio Dagotto. *Science.*, 271:618, 1996.

[31] T. M. Rice, S. Gopalan, and M. Sigrist. *Eur. Phys. Lett.*, 23:445, 1993.

[32] T. Osafune, N. Motoyama, H. Eisaki, and S. Uchida. *Phys. Rev. Lett.*, 78:1980, 1997.

[33] Y. Mizuno, T. Tohyama, and S. Maekawa. *Phys. Rev. B.*, 58:R14713, 1998.

[34] M. Arai and H. Tsunetsugu. *Phys. Rev. B.*, 56:4305, 1997.

[35] T. Takahashi, T. Yokoya, A. Ashihara, O. Akaki, H. Fujisawa, A. Chainani, M. Uehara, T. Nagata, and J. Akimitsu. *Phys. Rev. B.*, 56:7870, 1997.

[36] M. Kato, K. Shiota, and Y. Koike. *Physica C.*, 258:284, 1996.

[37] M. Isobe and E. Takayama-Muromachi. *J. Phys. Soc. Jpn*, 67:3119, 1998.

[38] S. A. Carter, B. Batlogg, R. J. Cava, J. J. Krajewski, W. F. Peck, and T. M. Rice. *Phys. Rev. Lett.*, 77:1378, 1996.

[39] M. Matsuda and K. Katsumata. *Phys. Rev. B.*, 53:12201, 1996.

[40] R. G. Eccleston et al. *Phys. Rev. Lett.*, 81:1702.

[41] S. Katano et al. *Phys. Rev. Lett.*, 82:636, 1999.

[42] M. Matsuda, T. Yosihama, K. Kakurai, and G. Shirane. *Phys. Rev. B.*, 59:1060, 1999.

[43] L. P. Regnault, J. P. Boucher, H. Moudden, J. E. Lorenzo, A. Hiess, U. Ammerahl, G. Dhalenne, and A. Revcolevschi. *Phys. Rev. B.*, 59:1055, 1999.

[44] B. Ruzicka, L. Degiorgi, U. Ammerahl, G. Dhalenne, and A. Revcolevschi. *Eur. Phys. J.*, 6:301, 1998.

[45] B. Ruzicka, L. Degiorgi, G. I. Meijer, J. Karpinski, U. Ammerahl, G. Dhalenne, and A. Revcolevschi. *Physica C.*, 282:317, 1999.

[46] N. Nücker et al. *Phys. Rev. B.*, 62:14384, 2000.

[47] N. Motoyama, T. Osafune, T. Kakeshita, H. Eisaki, and S. Uchida. *Phys. Rev. B.*, 55:R3386, 1997.

[48] K. Magishi, S. Matsumoto, Y. Kitaoka, K. Ishida, K. Asayama, M. Uehara, T. Nagata, and J. Akimitsu. *Phys. Rev. B.*, 57:11533, 1998.

[49] C. Hess et al. *Physica B.*, 312:612, 2002.

[50] M. Takigawa, N. Motoyama, H. Eisaki, and S. Uchida. *Phys. Rev. B.*, 57:1124, 1998.

[51] U. Ammerahl, B. Büchner, C. Kerpen, R. Gross, and A. Revcolevschi. *Phys. Rev. B.*, 62:R3592, 2000.

[52] D. E. Cox, I. Iglesiais, K. Hirota, G. Shirane, M. Matsuda, N. Motoyama, H. Eisaki, and S. Uchida. *Phys. Rev. B.*, 57:10750, 1998.

[53] R. G. Eccleston et al. *Phys. Rev. B.*, 53:14721, 1996.

[54] M. Matsuda et al. *Phys. Rev. B.*, 54:12199, 1996.

[55] K. Kumagai, S. Tsuji, M. Kato, and Y. Koike. *Phys. Rev. Lett.*, 78:1992, 1997.

[56] Kataev et al. *Phys. Rev. B.*, 64:104422, 2001.

[57] Cornelius Lanczos. *J. Res. Nat. Bur. Stand.*, 45:255–282, 1950.

[58] C. Lanczos. *J. Res. Natl. Bur. Stand.*, 45:255, 1950.

[59] D. G. Pettifor and D. L. Weaire (eds.). *The Recursion Method and Its Applications.* Springer, Berlin, Heidelberg. Springer Ser. Solid-state Sci, 1985.

[60] W. H. Press et al. *Numerical Recipes.* Cambridge 1992. Cambridge University Press., 1992.

[61] J. E. Hirsch. *Phys. Rev. B.*, 31:4403, 1985.

[62] P. W. Leung and E.P. Oppenheimer. *Comp. in Phys.*, 6:603, 1992.

[63] H. J. Schulz. *Int. J. Mod. Phys.*, 5:57, 1991.

[64] Rüdiger Klingeler. Forschungsberichte aus den Naturwissenschaften / Physik. Mensch & Buch Verlag., Berlin, 2003.

[65] Rüdiger Klingeler. private comunication.

[66] C. Y. Chen et al. *Phys. Rev. Lett.*, 63:2307, 1989.

[67] F. Barriquand and G. A. Sawatzky. *Phys. Rev. B.*, 50:16649, 1994.

[68] V. J. Emery, S. A. Kivelson, and O. Zachar. *Phys. Rev. B.*, 56:6120, 1997.

[69] Y. Mizuno, T. Tohyama, S. Maekawa, T. Osafune, N. Motoyama, H. Eisaki, and S. Uchida. *Phys. Rev. B.*, 57:5326, 1998.

[70] M. Takahashi. *J. Phys. C.*, 10:2389, 1977.

[71] A. Auerbach. *Interacting Electrons and Quantum Magnetism.* Springer-Verlag. New York:, 1994.

[72] P. Fulde. *Electron Correlations in Molecules and Solids.* Springer-Verlag. Berlin:, 1991.

[73] H. Bethe. *Z. Phys.*, 71:205, 1931.

ACKNOWLEDGMENTS

My sincere gratitude to my advisor, Apl. Prof. Dr. J. Schnack, for his flexibility, enthusiam, effort to offer the necessary equipment for his students and also for giving me the freedom and support which were very helpful making my research enjoyable. I would like also to thank him much for offering me the possibility to use intensively his machines for my exact diagonalization calculations. It is also with warmth that I would like to express my gratitude towards Prof. K. Betzler who showed interest and took the time to read my thesis. I also express my appreciation to Dr. J. Schulenburg for letting me use his Exact Diagonalization code as a tool to do my thesis work. There are many more people to name who I had the chance to interact with during my studies. These include Prof. J. Zaanen, Prof. D. Campbell, Dr. P. Sengupta, Dr. B. Valenzuela, Dr. Ejima, Prof. F. Gebhard, Dr. O. Starykh, Prof. T. Giamarchi, Dr. T. Vuletic and Dr. M. Arikawa who support me much and who I consider as a best friend. I do not want to forget a number of people that played an important role in my studies. I could not get much data, needed for my work, without the kind support of Robin, Peter Hage, Mirko Brüger and Mohand Allalen. I also express my appreciation to Matthias Exler and Frank Hesmer for their help. Thanks to all personnel as well as professors and staff of the PhD program Synthesis and Characterisation of Surfaces and Interfaces assembled from Clusters and Molecules.